Università degli Studi di Torino
Scuola di Dottorato in Scienze della Natura

Quantum sensors based on nitrogen-vacancy centers for biological applications

Giulia Petrini

Università degli Studi di Torino
Scuola di Dottorato in Scienze della Natura

Dottorato in Fisica

Quantum sensors based on nitrogen-vacancy centers for biological applications

Giulia Petrini

Tutor: Dr. Ivo Pietro Degiovanni

Accademic Tutor: Prof. Paolo Olivero

Contents

Introduction

The principles of quantum mechanics, developed in the first half of the '900 century, formed the basis for the first "quantum revolution", which established, during the second half of the century, the new rules underlying the description of nature. In more recent times, the growing understanding of the quantum states of many physical systems and the ability to directly manipulate them, allowed the creation of technological devices that base their operation on quantum principles. Potentially, these devices offer enormously superior performances compared to the current ones, in the fields of telecommunications, metrology and sensors. In recent decades, quantum technologies aroused increasing interest from the scientific community, which is preparing for the challenges of the "second quantum revolution" offering the possibility of further improvements in various scientific fields.

In particular, in recent years there has been an interest in the development of physical systems capable of emitting single photons on request and in a stable way over time to generate new methods of secure communication, quantum computation and the definition of *cybersecurity* protocols. Numerous devices have been created with the aim of satisfying this demand. Nevertheless, these devices still have non-ideal characteristics. Among the new candidates as single photon sources, luminescent defects in the diamond play an important role, which can be created in a controlled way by means of ion implantation. Among the possible optically active defects, the most studied diamond reticular defect is the nitrogen-vacancy (NV) complex, consisting of a nitrogen substitutional defect arranged in a reticular site adjacent to a vacancial-type defect, which represents a more stable structure more with respect to the corresponding individual defects. This complex, in addition to being a single photon emitter in conjunction with an appropriate optical stimulation, possesses remarkable spin properties. The possibility of single spin optical initialization, read out at room temperature and its long spin coherence time, make the NV center promising in the field of sensors, laying the foundations for its possible use as an ultra-sensitive nano-detector of electromagnetic and temperature fields with an unprecedented combination of spatial resolution

and sensitivity.

In this thesis a recent non-classicality criterion with respect to the usually adopted second-order autocorrelation function was experimentally investigated in order to discriminate single photon sources. Its advantage lies in the resistance to Poissonian noise as well as in the possibility of assessing the non-classicality of emitters even in large ensembles.
In addition, in this thesis the statistical nature of a single photon source in a continuous laser regime is analyzed. Although the sub-Poissonian statistic ($Var[n] < E[n]$) of these sources in the pulsed laser regime is now established, in conditions of continuous optical stimulation the Poissonian statistic ($Var[n] = E[n]$) is believed to be the one actually measured. However, there is a possibility of observing the quantum nature of the source if the excitation rate is comparable with the inverse of the lifetime.
Moreover luminescent nanodiamonds were internalized in living cells consisting in a network of mouse hyppocampal neurons. Thanks to the exceptional natural biocompatibility of the diamond, temperature variations at the level of the single hippocampus cell, linked to biological processes, were analyzed in detail.
Finally, technological and experimental improvements are analyzed to achieve better sensitivities for measuring electromagnetic fields by exploiting bulk diamonds.

The thesis is structured as follows:

Chapter 1 – *The diamond and the nitrogen-vacancy center.* The basic notions relating to the properties of the diamond and of the center are presented.

Chapter 2 – *Single photon emitters: basics.* The single photon sources (SPSs) and their applications are presented. The Glauber function and recently proposed anti-correlation function (dubbed θ parameters) are analyzed for SPSs identification in continuous laser exposure regime. Finally, the well-known two-level model is presented, which allows to describe the SPS and therefore to characterize it by analyzing the behavior of the Glauber function.

Chapter 3 – *Single photon source characterization.* After having analyzed the emission statistics in the case of pulsed laser regime, the statistical distribution of a SPS in continuous laser exposure regime in described. Finally a new method to discriminate the presence of SPSs in the presence of thermal and Poissonian fields is presented.

Chapter 4 – *NV^- center as a sensor.* The basic principles of the measurement techniques used (the optically detected magnetic resonance ODMR) are presented, analyzing in detail the measurement of magnetic and electric fields and temperature variations.

Chapter 5 – *Single photon confocal microscope with microwave control equipment for sensing measurements.* The confocal microscope theory and the apparatus used is presented.

Chapter 6 – *NV^- center as bio-sensor.* The bio-sensing properties are clarified from the theoretical point of view. The possibility of applications of the sensor in the biological field for the detection of electromagnetic fields and temperature variations is outlined.

Chapter 7 – *Nanodiamonds quantum sensors application: temperature measurement inside living cells.* The experimental results in the detection of temperature variation in a cell culture of mouse cortical neurons are shown.

Chapter 8 – *Bulk diamonds based-sensors: sensitivity improvements towards biological applications.* The experimental results obtained to improve the sensitivity of the measurement technique are shown by exploiting the greater spin coherence of the bulk diamond, pulsed measurement techniques and optimized a bias magnetic fields.

Summary. The results obtained are summarized and the future prospects for the research activity continuation are highlighted.

Chapter 1

The diamond and the nitrogen-vacancy center

1.1 The diamond

The diamond is a well known material. While its brilliance is at the center of interest in the jewelry industry, its extreme physical properties make it unique and appealing in scientific and technological applications. The diamond is entirely based on carbon atoms, a chemical element of group IV, known for its abundance and versatility due to its ability to establish chemical bonds of different types both with other carbon atoms both with other elements. For this reason carbon occurs in nature in different forms with well-defined chemical structures and characterized by different inter-atomic bonds.
If in a diamond each carbon atom is bonded to four other atoms arranged at the vertices of a tetrahedron, according to a structure that guarantees the crystal's peculiar hardness, in graphite and fullerene each carbon atom is bonded to three more atoms creating planar structures. There are also cylindrical structures with a nanometric diameter made up entirely of carbon atoms and called nanotubes, which can be imagined as rolled up graphene sheets.

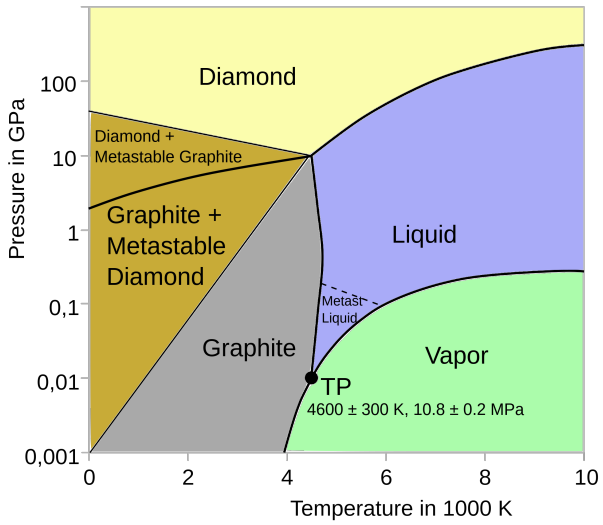

Figure 1.1: Carbon phase diagram.

By observing the carbon phase diagram (see Figure 1.1) it can be seen that under normal ambient pressure and temperature conditions, the thermally stable allotropic form is the graphite. In these conditions, the diamond appears as a metastable form but the potential barrier that needs to be overcome for a spontaneous conversion into graphite is so high ($\simeq 2\ eV$) that this never happens spontaneously under normal ambient conditions. The diamond, on the other hand, appears to be the configuration that maximizes the bond energy, and therefore the most stable, at a temperature of the order of 4000 K (melting point) and at pressures of the order of GPa.

1.1.1 Crystal structure

Among all the possible allotropic forms of carbon, in the diamond the atomic orbitals of carbon pass from the electron configuration $1s^2\,2s^2\,2p^2$ to a new hybridized configuration, creating the 4 atomic valence orbitals $sp^3 : 2s\,2p_{x,y,z}$, each with an unpaired electron. This electronic configuration determines the typical tetrahedral structure of the carbon atoms in the diamond, which generate, from the crystallographic point of view, a face-centered cubic lattice (FCC) with cell parameter $a_0 = 3.57\ \mathring{A}$, where the carbon atoms of the base occupy the lattice positions $(0, 0, 0)$ and $(\frac{1}{4}, \frac{1}{4}, \frac{1}{4})$ (see Figure 1.2). In this

configuration, each carbon atom has a distance from its first 4 neighbors equal to 1.5 $\mathring{A}$, has an atomic density of $1.77 \times 10^{23}\ cm^{-3}$ and a mass density of $3.54\ g\ cm^{-3}$.

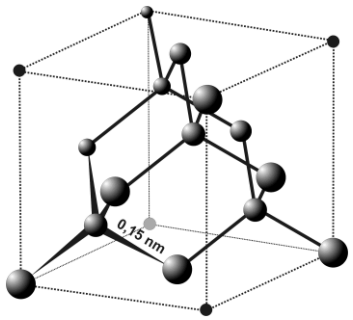

Figure 1.2: Diamond lattice primitive cell.

1.1.2 Mechanical, chemical and vibrational properties

Each carbon atom shares its 4 electron orbitals with 4 adjacent atoms. The 4 starting atomic orbitals generate 8 energy sub-bands, 4 of which are completely occupied by the valence electrons of the crystal, and constitute the valence band of the diamond, while the other 4 remain unoccupied and constitute the conduction band. The amplitude of forbidden energy that separates the valence band from the conduction band has a very high value compared to other materials, equal to $E_{gap} = 5.5\ eV$. The bond energy between the carbon atoms in the diamond is also very high ($7.73\ eV$) and determines the extreme mechanical macroscopic characteristics that determine the industrial and technological interest of this material. In particular, atomic cohesion generates a high Young's modulus ($1220\ GPa$) and a hardness value equal to 10 on the Mohs scale. From a chemical point of view, the high bonding energy means that the only chemical process capable of eroding the diamond surface is oxidation at high temperatures. Consequently, the diamond is chemically inert and, if we add to this the fact that it is made up entirely of carbon atoms, it appears that the crystal is bio-compatible and can therefore play an important role in bio-physical applications. Among the other characteristics of the diamond, there is the high Debye temperature ($2200\ K$), which reflects the fact that the crystal is characterized by a low density of phonons

at ambient temperature compared to other crystals. This determines a low number of collisions with the crystal lattice and consequently the diamond has a high thermal conductivity.

1.1.3 Electrical and optical properties

The high bond energy between the carbon atoms and the high forbidden energy amplitude have important consequences on the electrical and optical properties of the diamond. As for the binding energy, it guarantees the possibility of applying an electric field up to the value of *breakdown* $E_{bd} = 10^7\ V\ cm^{-1}$, which allows to subject the diamond to intense electric fields without generating electric discharges inside. The high band gap, on the other hand, means that, from an electrical point of view, at room temperature the diamond is included in the category of insulating materials or, alternatively, it can be considered as a semiconductor with a large gap energy. On the other hand, a forbidden energy of 5.5 eV ensures that the diamond is transparent to light in a spectral range up to $\lambda = 220\ nm$, encompassing the whole spectrum visible and infrared. Finally, the diamond has a high refractive index, described by the *Sellmeier's law*:

$$n^2 = 1 + \frac{4.3556 \cdot \lambda^2}{\lambda^2 - (0.1060)^2} + \frac{0.3306 \cdot \lambda^2}{\lambda^2 - (0.1750)^2} \tag{1.1}$$

Being its refractive index of $n_{medium} = 2.42$, the material has a high reflectance (up to 17 %) and therefore the light that is transmitted to it can undergo numerous internal reflections before emerging from the crystal: this feature becomes problematic to maximize the amount of photoemitted radiation by the luminescent centers it can contains.

1.1.4 Bulk diamond production

The high cost and poor reproducibility of different natural diamonds, characterized by uncontrolled growth conditions, made it necessary to develop methods for producing artificial samples. In particular, there are two synthetic diamond synthesis procedures: the *high pressure and high temperature* (HPHT) technique and the *chemical vapor deposition* (CVD) technique.

1.1.4.1 High pressure and high temperature (HTHP) technique

This synthesis technique originates from a diamond sample (called "seed"), around which carbon is present, generally in graphitic form. The sample is also immersed in a solvent in which there are catalysts (Fe, Co, Ti) which have the function of accelerating the growth process. Everything is pressed until pressures of the order of 10 GPa are reached and is heated up to temperatures of 1770 K, thus recreating the growth conditions of the natural diamonds that occur below the earth's crust. The graphite sample is subjected to pressure and temperature conditions in which the diamond is the thermodynamically favored allotropic form. Although this technique is very economical, it has the disadvantage of creating diamond with many impurities in the crystalline matrix. Consequently, the HTHP technique is mostly used for mechanical applications. By refining the technique it is however possible to reduce impurities, in particular the most abundant is that of nitrogen. This is achieved by inserting catalysts (such as Ti, Al, or Zr), which bind to the impurities during the synthesis process, avoiding their incorporation into the crystal lattice.

1.1.4.2 Chemical vapor deposition (CVD) technique

The technique consists in the deposition of single atomic layers on a suitable substrate, chosen in such a way as to minimize the reticular "mismatch" and therefore mechanical stress. To produce artificial diamond using this procedure, the most suitable substrate is the monocrystalline diamond in order to allow *homoepitaxial* growth. Alternatively, another material can be used as long as it has similar crystallographic characteristics, in this case the procedure is called *heteroepitaxial*. During the growth process, the substrate temperature is about 1000 K and the pressures of the order of 10^{-3} Pa. 2.46 GHz frequency microwaves are used to activate a chemically highly reactive plasma composed of carbon ions and hydrogen ions. The carbon is deposited on the substrate forming both the chemical bonds sp^2 and sp^3, generating graphite and diamond, respectively. Hydrogen plasma is capable of splitting graphite bonds, allowing only the diamond deposition. Other gases (such as nitrogen and boron) can be introduced into the chamber during the growth process to create, in a controlled way, some luminescent defects or, alterna-

tively, to dope the material from an electrical point of view. For this reason the CVD technique, even if it is more expensive and slower than HPHT technique, it allows the production of monocrystalline high purity diamonds or with more controlled doping.

1.1.5 Nanodiamonds production

The techniques for the creation of NV centers in diamond are well established also for nanodiamonds (NDs). Nanodiamonds-based sensors exploit colloidal suspensions of single diamond particles of minimum diameter of 4-5 nm, but on average the nanodiamonds typically used in experiment have a size of 50-100 nm. The nanometer size makes nanodiamonds-based sensor of extreme interest for bio-sensing application, as they are potentially usable in vivo experiments. Nonetheless, they have also important drawbacks such as e.g. the increased sensitivity of NV spins to environmental noise. Indeed, while in a bulk diamond the in coherence time T_2^* is mainly influenced by the electronic impurities and nuclear spins in the surrounding, for nanodiamonds the coherence time is further reduced due to the surface spin noise. This should be taken into account in the estimation of the sensitivity limit (see Equation (6.2)). Despite this limitation, nanodiamonds have attracted interest also as a non-toxic alternative to quantum dots for biomedical imaging, as magnetic sensors and finally as drug transporters (thanks to the discovery of the possibility to functionalize the diamonds surface in various ways, exploiting the covalents carbon bonds). The great interest and the exceptional range of applications of NDs is boosting the development of novel fabrication techniques, even if the actual technologies are already able to provide very pure nanodiamonds with controlled surface chemistry at a relative low cost [1, 2]. Nanodiamonds are usually fabricated by milling of CVD or HPHT crystals, in this way the nanocrystals sizes are ranging from 20 to 200 nm. To reach smaller sizes, in order to increase the internalization rate in living organisms for sensing or drug delivery purposes, detonation nanodiamonds can be produced starting from solid carbonous precursors, with this method sizes down to a couple of nanometers can be achieved.

1.1.6 Classification

Artificial diamonds are classified according to their degree of purity [3]. Given that the most common and naturally present impurities are nitrogen and boron (being elements with an atomic radius very similar to that of carbon and therefore easily incorporated into the diamond lattice), their respective concentrations are used to proceed with the categorization, as described below.
The types of diamonds are as follows:

- *Ia* when the nitrogen impurity concentration is between 100 ppm and 1000 ppm, which is high enough to be measurable with IR spectroscopy. Being so abundant, nitrogen is in aggregate form. This category of artificial diamond is referred to as "*mechanical grade*" diamond, since the only technologically relevant characteristic is mechanical hardness;

- *Ib* when the nitrogen concentration is around 500 ppm, still measurable with IR spectroscopy. The distribution of the substituted nitrogen atoms is no longer in aggregate form, but isolated. Most of the diamonds created with the HPHT technique belong to this category. The nitrogen impurities introduce a continuous absorption band in the green and blue region of the visible spectrum, giving the diamond sample a typical yellowish color;

- *IIa* when the nitrogen concentration is less than 10 ppm and therefore becomes difficult to measure with conventional techniques. The diamond is transparent and is referred to as"*optical grade*" type. Most of the diamonds created with the CVD technique belong to this category;

- *IIb* when the nitrogen concentration is still lower than in the previous category. The properties of the diamond are significantly influenced by the presence of isolated boron impurities, which acts as an acceptor and determines a conductive behavior of the p-type diamond. Diamonds belonging to this category are referred to as "*electronic grade*" diamonds, alluding to their good charge carrying properties.

- Finally, the crystalline matrix of the purest diamonds may still have an intrinsic magnetic field due to the non-zero spin of the naturally

occurring C^{13} isotope atoms. By using isotopically purified gases during the growth process, it is possible to significantly reduce the concentration of C^{13}, and such a sample is called "*quantum grade*".

1.2 Color center in diamond: the nitrogen-vacancy (NV) center

The diamond optical properties described in the previous sections can be adequately modified by introducing defects in the crystalline matrix in a controlled way. These defects can be of various types:

- **interstitial**, when the impurity is constituted by an atom that is inserted between the positions of the diamond lattice;
- **substitutional**, when the impurity atom is inserted in the place of a carbon atom, thus occupying the correct lattice position;
- **vacancial**, when the carbon atom is missing from the crystalline site;
- **a combination of them**, when the impurity consists of an atomic structure in which several types of defects appear (such as the *nitrogen-vacancy* complex which will be discussed in the next sections).

These defects can be naturally present in the crystalline matrix of the diamond, or artificially inserted during the diamond CVD growth, or subsequently by means of ion implantation.The presence of such impurities introduces electronic levels within the diamond forbidden band. Depending on the type of defect, the energy levels can be very close to the valence/conduction band, or deeper, creating localized electronic states. Typically these levels consist of a ground state and one or more excited states. During an appropriate stimulation, for example an optical stimulation (by means of a laser source with a wavelength small enough to provide the required energy) or an electrical stimulation(by an external current), the electronic state can change from its own fundamental state to its excited state. Depending on the energy absorbed by the electronic state, the system can transit in one of the vibrational levels of the excited state. After a few *ns* the system evolves to the

vibrational state zero of its excited level and it can go through the following relaxation processes, see Figure 1.3:

- relax directly to the ground state, emitting its own characteristic radiation, which in this case is called *zero phonon line "ZPL"*;
- relax in one of the vibrational levels of the ground state, thus emitting photons of longer wavelength. In this case the emission spectrum presents additional peaks which are called *phononic repetitions*;
- alternatively the physical system can relax without photon emission, through lattice interactions and/or resonant energy transfer to proximate defects. In this case the system relax through a non-radiative channel.

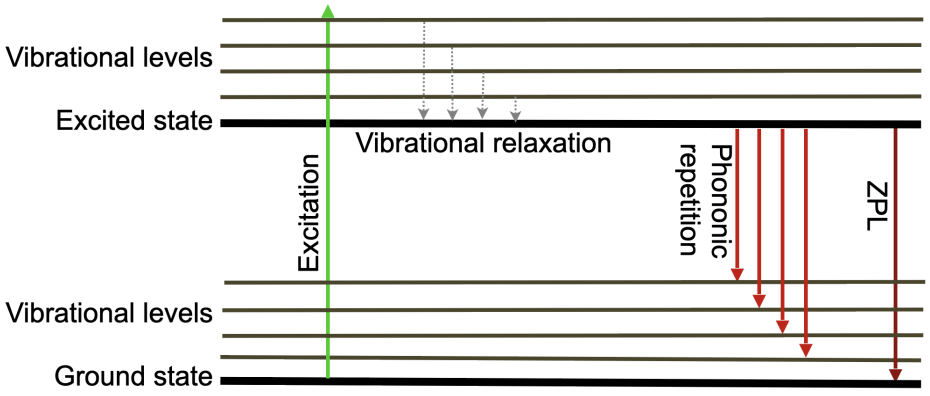

Figure 1.3: Diagram of the transitions between the energy levels in the diamond band gap. The black bold lines represent the ground state and the excited state. The black lines represent the vibrational levels of the respective states. The green arrow represents the stimulation (optical or electrical). Finally, the red arrows refer to the possible relaxation channels.

The defects for which it is possible to observe photon emission are also called *luminescent defects* and, in particular, if the emission occurs in the visible, they are called *color centers*.
There is a parameter, called *quantum efficiency*, defined as the ratio between the probability of radiative and non-radiative relaxation. In general, for the use of these defects, the quantum efficiency should be as high as possible.

By subjecting the diamond sample to optical stimulation, it is also possible that the exciting photon stimulate the valence band electronic state. In this case, the electronic state can be promoted to a virtual excited state and relaxed by interacting with the diamond crystal lattice. This effect is called *Raman scattering* and results in the emission of light at different wavelengths than that of the exciting radiation. This energetic variation is linked to the energy of the vibrational state involved (*Raman shift* for first order Raman scattering in the diamond: RS = 1332 cm^{-1}). This spectral shift appears both for higher energies if the phonon is absorbed (*Anti-Stokes transitions*), and lower if the phonon is generated following the transition (*Stokes transitions*).

Of all the luminescent defects in artificial diamonds, the most studied is the nitrogen-vacancy (NV) center, which is the main topic of this thesis. The nitrogen-vacancy defect is a complex of impurities composed of a substitutional nitrogen atom, arranged in a reticular site adjacent to a vacancy-type defect, see Figure 1.4. The system has a pyramidal symmetry (C_{3v}) and has as its symmetry axis the direction that joins the nitrogen atom with the vacancy. With respect to the tetrahedral structure of the diamond, there are in total 4 possible orientations of the defect, among them equally probable under conventional synthesis conditions. There are two configurations in which the complex can be found and they are distinguished by the number of electrons involved: the neutral state, called "NV^0" and the negative one, called "NV^-". The 3 carbon atoms surrounding the vacancy contribute by sharing 1 electron each to the complex, while nitrogen with 2. If in total there are only these 5 electrons in the system, the center it is electrically neutral (NV^0) with total electron spin $S = \frac{1}{2}$. Alternatively, the defect can trap 1 additional electron from the surrounding lattice. In this case, the center NV^- is formed, which is negatively charged and has total electron spin S = 1.

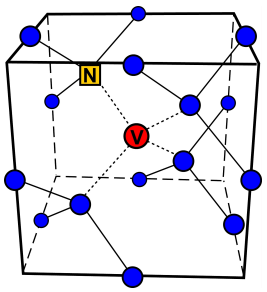

Figure 1.4: Diamond crystalline structure with nitrogen-vacancy defect.

1.2.1 Optical properties

Both charge states of the complex are optically active (i.e. capable of emitting luminescence if stimulated optically), but are characterized by a different spectral emission (see Figure 1.5).

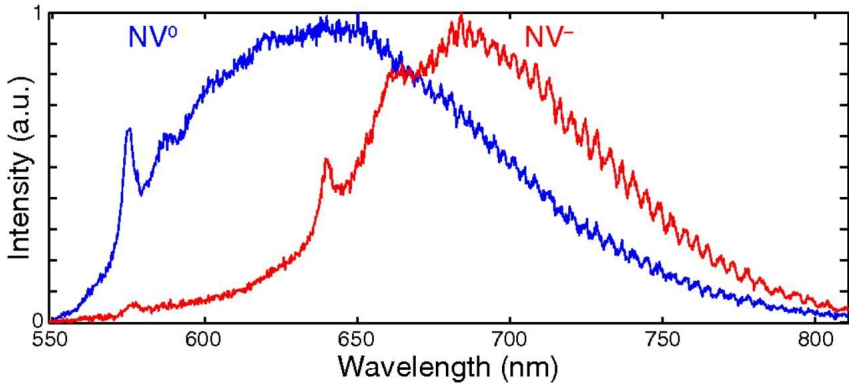

Figure 1.5: Spectral emission of the nitrogen-vacancy centers.

The most defined emission peak, present at wavelengths $\lambda = 575\ nm$ for the neutral state of charge and $\lambda = 638\ nm$ for the negative state, is associated with the respective *zero phonon line* (ZPL). It is due to the purely radiative relaxation of the complex. The emission at longer wavelengths is associated with the relaxation process mediated by the production of phonons.
It is important to underline that the center, once formed, is not bound to remain in a fixed state of charge but can pass from one to the other simply by electronic entrapment/de-entrapment. The state of charge is determined

by the position of the Fermi level in the diamond, which depends on the concentration of nitrogen atoms and other impurities in the crystal, as well as on the chemical termination of the surface, which may be primarily hydrogen atoms or oxygen. In the case of hydrogen termination, due to electric dipole interactions, the neutral configuration NV^0 is more likely because the Fermi level of the diamond is at lower energy than the NV^- level. If, on the other hand, the surface is oxidized, the effect due to the electric dipole interactions leads to the opposite situation. The intensity of the interaction with the surface terminations is inversely proportional to the square of the distance, therefore this effect is observed across the first 20 nm of depth from the surface, while at greater depths it becomes negligible.
As can be seen from the Figure 1.5, the emission associated with this type of defect in artificial diamonds is not monochromatic. Furthermore, the life time of the electronic state in excited states is about 12 ns, which is too high for applications in quantum communication. Therefore, although the nitrogen-vacancy complex appears as a single photon source, it cannot satisfy all the characteristics of ideality presented in the previous section. On the other hand, the NV^- center exhibits particular properties relevant to spintronics, which make it a system of interest for a number of applications in quantum computing and magnetometry.
It will be precisely the negative state of charge, the cornerstone of this thesis work.

1.2.2 NV^- energy levels structure

The NV^- complex is characterized by 2 additional electrons with respect to the electron configuration of the diamond, which determine the effective spin of the system: S = 1. Consequently, analyzing in more detail the scheme of energy levels (Figure 1.6), it presents a ground state of *spin triplet* ($^3A_2$) and an excited state of *triplet* (^3E), separated by an energy of 1.945 eV.

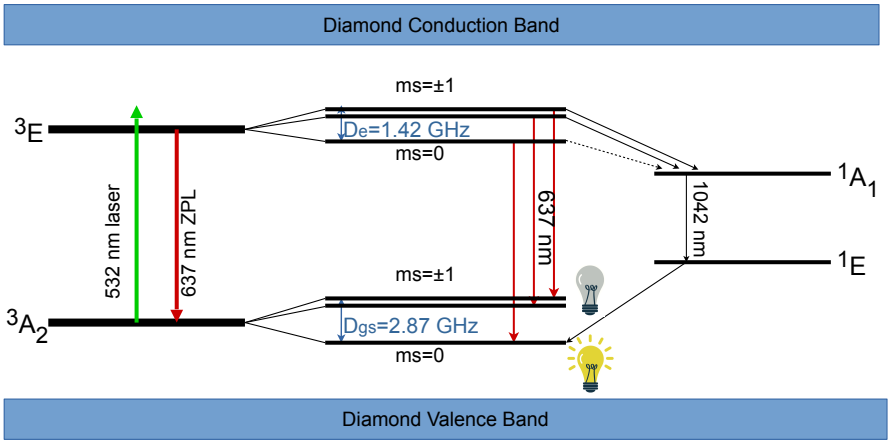

Figure 1.6: NV^- energy levels structure

The letters indicate the type of symmetry of the orbitals involved in the transitions optics.
The states with third spin component $|m_s = \pm 1\rangle$ are degenerate in the absence of electromagnetic fields. Instead, due to the *spin-orbit interaction*, there is an energy difference between the state $|m_s = 0\rangle$ and the states $|m_s = \pm 1\rangle$, which as indicated in the Figure amounts to $D_{gs} \sim 2.87$ GHz. This type of *splitting* is also present for the excited state and is worth $D_{ex} \sim 1.42$ GHz.
With a green emission laser it is possible to excite the system in a *non-resonant* way, from the ground state to the excited state (green lines in Figure 1.6). The relaxation mode can follows two alternative paths depending on the initial spin state of the system:

- If the initial state is $|m_s = 0\rangle$, a radiative transition occurs with the emission of a photon at around wavelength 637 nm (ZPL). In this process, the quantum number m_s is conserved. It is also possible a relaxation with production of phonons, in which case it is possible to observe the phononic replicas at wavelengths range between 650 nm and 800 nm. The lifetime of the excited state depends on the temperature and on the type of crystal: for a monocrystalline diamond it is worth $\tau = 12\ ns$.

- If the initial state is $|m_s = \pm 1\rangle$, two relaxation channels are possible. The first, in which the spin is preserving, is completely analogous to that

previously described. In the second relax channel the quantum number m_s is not conserved and the system relaxes in the configuration $|m_s = 0\rangle$ of the ground state. In the latter case the system passes through two metastable states of *singlet*, namely ^1A and ^1E, between which there is a radiative transition at a wavelength of 1042 nm. The spin variation process is known in literature as *inter-system crossing*. The metastable states have a lifetime of 200 ns. (More in detail, this relaxation channel through the metastable levels is also possible from the $|m_s = 0\rangle$ level, however the probability is much lower).

From the excited state $|m_s = \pm 1\rangle$, the transition through the metastable state happens with a probability of $\sim 30\%$. This involves the configuration $|m_s = \pm 1\rangle$ is characterized by a radiative efficiency lower than that $|m_s = 0\rangle$. In fact, these two states are referred to as *dark-state* and *bright-state* respectively. Regardless of the initial spin, if the external laser irradiation it lasts over time, as a consequence of multiple cycles of excitation and relaxation the electronic spin of the system is initialized in the state $|m_s = 0\rangle$, due to the above process. The application of a microwave pulse of frequency equal to D_{gs} can modify the spin, bringing the electronic state in $|m_s = \pm 1\rangle$, as will be explained in detail in Chapter 4.

1.2.3 NV color center creation processes

One of the reasons why the nitrogen-vacancy defect has been extensively studied is that nitrogen is an impurity naturally present in diamonds, typically it is the most common one (this is the reason why it is used to classify artificial diamonds according to its concentration). To control the creation of the NV center, one can regulate the density of nitrogen defects during the growth of the diamond itself and/or adjust the vacancy density in the lattice after the diamond sample creation. For this purpose, the sample is irradiated with ions or other energetic particles, such as electrons and neutrons. This process damages the crystal by creating vacancies. By controlling the incident particles fluence it is possible to regulate the concentration of the induced vacancies in the crystal. Furthermore, the type and energy of the particles used determines the depth at which the defects are formed. For ions, for example, this process takes place decisively at their *Bragg peak*. To

create vacancy in a controlled way, codes are used that simulate the effect of particles radiation.
At the end of irradiation process the sample is subjected to heat treatment at a temperature above 600 °C (*annealing process*). At these temperatures the thermal energy is sufficient to allow the vacancies to become mobile and therefore able to migrate from one reticular site to another, unlike the substitutional nitrogen which remains immobile within the reticulum. This migration process continues as soon as a NV center is formed, which represents a significantly more energy-stable complex.
A diamond synthesized with the CVD technique is characterized by a small percentage of native defects, because during growth only a fraction of substitutional nitrogen (typically $< 0.5\%$) forms NV complexes by trapping the vacancies also created naturally during growth. So sometimes it can be convenient to implant nitrogen ions in order to simultaneously increase the nitrogen concentration as well as the vacancy-type defects.

Chapter 2

Single photon emitters: basics

A single photon source (SPS) is referred to as a physical system capable of emitting a single photon at a time. For the applications that will be described in the next sections, an emitter of this type must have some ideal characteristics, including:

- reliably guarantee an on-demand emission;
- have a high emission rate (of the order of GHz);
- guarantee a stable emission over time;
- exhibit monochromaticity of the emitted photon, preferably at a wavelength in which the transmission along the optical fibers is maximized;
- indistinguishability.

Since the 1970s physical systems, which attempt to implement a single photon emitter, have been studied. They can be divided into two types, that is sources with *probabilistic emission* and sources with *deterministic emission*.
A first example of a probabilistic emitter is represented by the *attenuated pulsed laser*. In this approach, a laser beam is attenuated so that it *statistically* emitted only one photon in a single pulse. These pulses inevitably have a multi-photonic component and it is therefore not possible to guarantee that a single photon is present in each emission.
An alternative probabilistic technique exploits the phenomenon of the *parametric down conversion* (PDC), which can occur in particular materials, such as non-linear crystals. In the PDC, the absorption of a photon can create

a pair of photons. In the process, the conservation of the energy and the momentum of incident and outgoing photons occurs. One of the 2 photons emitted is used as a *trigger* signal, which is detected by a single photon detector. This triggers the second photon arrival. The probabilistic aspect of PDC technique concerns the instant in time in which the emission occurs: the pair of photons is not created in a predefined instant, as the creation process is governed by statistical laws. Another disadvantage concerns the impossibility of guaranteeing a high emission rate, as the pair creation efficiency is very low: a pair of correlated photons is emitted every approximately 10^{12} photons of excitation.
An example of a deterministic emitter, closer to the ideal concept of a single emitter, is given by *quantum dots*. These consist of hetero-structures fabricated using epitaxial growth methods such as the *molecular beam epitaxy* (MBE): on a semiconductor with a certain band gap another semiconductor with a less wide band gap is grown. The size of these structures are nanometric, i.e. comparable with the characteristic wavelength of the charge carriers that are confined to them. In a regime of weak electrical or optical excitation, an exciton can be produced and the subsequent radiative recombination of the same electron-hole exciton pair results in the emission of a single photon. Although deterministic, the process typically occurs at cryogenic temperatures and this typically represents a significant technological disadvantage.
An alternative solution, which carries the promise of overcoming the limitations of the aforementioned systems, is represented precisely by the *luminescent defects in solids*. Taking up the characteristics of the ideal source required for the use of these devices, the radiation collected by the luminescent defects has the following advantages:

- can be considered *on demand*, because it occurs when the user decides to stimulate the defect (for example optically);
- is characterized by a high temporal stability, given that the photochemical degradation (*photobleaching*) typical of molecular systems is not present and, in particular, the use of diamond as host material ensures resistance to deterioration and chemical agents;
- some of these defects are characterized by a high quantum efficiency,

made possible by the low phonon density which reduces the probability of having non-radiative transitions or in any case assisted by interactions with reticular vibrations.

It is important to underline that not all defects have the same emission characteristics. Each impurity generates a specific discrete energy levels structure in the forbidden band, and therefore must be studied individually to understand if it can present suitable characteristics. The diamond is an excellent material to host defects: its high band gap can allow numerous radiative transitions inside it (in the diamond there are more of 500 optically active defects). Furthermore, being a transparent material over the entire visible spectrum, it does not absorb photons emitted by defects, even if the effect of internal reflections is not negligible due to its high refractive index.
Of all the luminescent defects in artificial diamonds, the most studied is the *nitrogen-vacancy complex*.

2.1 SPSs applications

As described, the nitrogen-vacancy center in the diamond is a single photon emitter, therefore it can be used for various applications in this sense. Although its emission is not ideal, single photon states are valid candidates such as *quantum bit*: the NV center therefore has potential applications in *quantum computing* and in *quantum cryptography*. Its use can also make a decisive contribution in *quantum metrology*, where the single photon can be used to link the candela unit to fundamental constants.

2.1.1 Quantum computation

The concept of *quantum computer* is based on unique properties characterizing physical systems governed entirely by quantum mechanics, such as *state superposition* and the *entanglement*. A quantum computer would be able to solve certain problems in a significantly more efficient way than a classic computer, making it even obsolete. The quantum computer is based on the implementation of *quantum bits*, instead of the *bits* on which the current information technology is based. At present, there are two possible logical

states, typically referred to as "0" and "1". Information technology of quantum computers, called QIP (Quantum Information Processing) is based on *qubits*.
The ideal physical system in which to implement the *qubits* is still the subject of fundamental research. Several candidates have been proposed: cold atoms, photons, nuclear spins in molecular systems, superconducting devices, quantum dots and defects in solids.
To build a quantum computer, specific criteria must be satisfy, called *Di-Vincenzo criteria* [4]. 7 have been listed, of which the first 5 are related to quantum computation and the last 2, here not considered, necessary for quantum communication.
The first 5 criteria are shown below.
1. Scalability and *qubits* well defined;
2. Ability to initialize the *qubits* status;
3. Coherence time much greater than the time of a logic gate operation;
4. Availability of a universal set of quantum gates;
5. Possibility to selectively query the *qubits* states.
Nitrogen-vacancy centers can be considered good candidates that satisfy these criteria. In fact they have a high coherence time ($\tau > 2\ ms$) and since the spin states have different luminosity, it is also possible to implement an optical spin state *readout* of the single defect.
Furthermore, a NV^- center inside a magnetic field has 3 states of distinguishable triplet. If we consider only the state $|m_s = 0\rangle$ and $|m_s = \pm 1\rangle$, the system is on 2 levels. Thanks to the possibility of coupling the NV^- centers to the nuclear spin of the surrounding crystal defects, quantum prototypes registers can be constructed.

2.1.2 Quantum cryptography

Cryptography deals with making a message indecipherable to actors who are not authorized to intercept it. Since the advent of computers, the public-key cryptographic techniques developed were based on complex mathematical problems, such as the prime number factorization: a problem that (it is believed) cannot be solved efficiently by a computer working according to the "classical" information theory. Despite today's advanced computational ca-

pabilities, computation times are so long that the code is relatively secure. The security of this approach will fail with the advent of *quantum computers*. Fortunately, quantum mechanics creates the problem with the quantum computer, but provides also the solution thanks to the quantum cryptography, or more correctly on quantum key distribution (QKD) solution. Indeed QKD allows the secure distribution of cryptographic keys that will be used in symmetric (and quantum-safe) cryptographic protocols such as the Vernam cipher of the AES (advanced encryption standard). Specifically QKD solution exploits single photons and the single photon sources can themselves represent a good way to encrypt the information.
Most known QKD protocol is called *BB84*. The abbreviation is composed by the inventors initials (Bennett and Brassard) and by the date of the first pubblication of the protocol (1984). The first protocol implementation using attenuated laser as single photon sources only happened in 1992. The crypto-key to be transferred safely is encoded through the polarization of single photon states that are sent from a sender A (Alice) to the receiver B (Bob). According to this protocol, Alice arbitrarily prepares single photons in polarization states on two different bases, each chosen at random. For example, Alice causally configures the photons in four different polarization states corresponding to the eigenstates of a horizontal-vertical base and a 45° base:

$$| \uparrow \rangle = 1 \qquad | \rightarrow \rangle = 0 \tag{2.1}$$

$$| \nwarrow \rangle = 1 \qquad | \nearrow \rangle = 0 \tag{2.2}$$

Bob performs polarization measurements on the photons that are sent to him, choosing also randomly between the two possible measurement bases. After the broadcast of the key, Alice, through a classic channel, publicly communicates the basis in which she has sent the photons, but not their polarization state, so that Bob can eliminate the measurements made using the wrong polarization bases. In this way, the remaining measures (*sifted key*) correspond exactly to the state of incoming photons. The probability that Bob randomly adopts the correct basis with which Alice prepared the photons is 50%, therefore about half of the photons sent will determine the *sifted key*.
It should be noted that when Bob and Alice use different bases the *bit* has however a 50% chance of being correct (with the wrong polarizer, the photon

polarization state is projected onto the other base), hence then total probability that Bob has a wrong *bit* is equal to $\frac{1}{4}$. Let's assume that an eventual spy (Eve) has the intention and the ability to intercept all the bits of the key and, in order not to reveal the interception itself, to retransmit each photon to Bob. According to the rules of quantum mechanics, by performing a measurement on a physical state on an arbitrary basis, the system is perturbed causing its wave function collapse on the measured value. As a result, the message relayed to Bob is affected by Eve's measure. Eve, like Bob, has to choose randomly between the 2 polarization bases with a 50% probability of guessing the base chosen by Alice. This intermediate measure perturbs the polarization state and produces an increase in the total probability that Bob receives wrong bits even within the *sifted key*. If only the bits belonging to the *sifted key* are considered, the probability that Bob receives the wrong *bit* in the presence of Eve is about 25%. At this point, Alice and Bob can decide to sacrifice a part of the key and broadcast its content on a classic channel. By analyzing later the probability of receiving Bob's wrong *bits*, it is possible to assess with certainty whether the key has been intercepted or if it has reached its destination without interception attempts. In the latter case, the remainder of the *sifted key* not shared on the classic channel is used as a key and the message encoded by it can be sent via the classic channel.
The protocol security level is significantly worsens if a classical source (such as the attenuated laser) characterized by non-negligible multi-photonic components is used, instead a single photon source (SPS). In this case Eve can carry out a *photon number splitting* (PNS) attack, that is, deterministically intercepting photons from each multiphotonic pulse, so as to have information about the signal sent. In this way Eve would have the possibility of determining the polarization of only one of these photons without altering the quantum observables of the others. In this way Eve is able to obtain the information without disturbing the state of the *qubits* transmitted. Furthermore, the recipient would have no way of detecting this intrusion because the missing photons can be attributed to losses during transmission and reception and therefore the safety requirement would be missing.
In conclusion, the system presented so far is totally safe from external attacks only if we consider the case in which there are pulses containing *always and*

only a single photon. This condition can be adequately satisfied by using nitrogen-vacancy centers as single photon sources. This type of system was built in 2004 [5], using this sources in nanodiamonds with an average diameter of 90 nm. The above experiment gave results in complete agreement with the theoretical models.

2.1.3 Metrology

According to the International System of units, the luminous intensity is quantified as equal to 1 candela (1 cd) if: in a given direction, a source emits monochromatic radiation with a frequency equal to 540×10^{12} Hz with an intensity in the direction of propagation of a value equal to 1 W in a steradian. The *Candela project* takes care of redefining this unit of measurement, based on the photons number rather than the power carried by the light. This would involve the possibility of tracing this measurement unit to Planck's constant, thus having a direct reference to a fundamental constant.

2.2 SPSs identification theory

One of the most debated issues in quantum mechanics is related to understanding the boundary separating the counterintuitive behavior of the systems governed by the quantum laws from the classical, familiar properties of the macroscopical systems. This transition also manifests itself in the realm of optics where, even if undoubtedly the radiation emitted by any possible source of light is indeed composed by an ensemble of individual photons, the properties of classical sources differ consistently from those of nonclassical ones.
Since nonclassical optical states have now become a fundamental resource for quantum technology [6], the determination of nonclassicality for a state is not only important for studies concerning boundaries from quantum to classical world, but also represents an important tool for quantifying such resources. Vast literature exists on the characterization of SPSs. Most of the techniques rely on the sampling of the second-order autocorrelation function (or Glauber function $g^{(2)}$), whose value is never smaller than 1 for classical light, while it is lower than 1 for sub-Poissonian light, and in particular vanishes for single-

photon states, where $g^{(2)} = 0$ is expected in the ideal case of a single photon source.

2.2.1 Glauber function $g^{(2)}$

To clarify whether the collected luminescence consists of a sequence of *single* photons emitted by individual defects, mathematically the *second order autocorrelation function* $g^{(2)}$ is used. This function is defined as follows:

$$g^{(2)}(t) = \frac{\langle I(t_0) \cdot I(t_0 + t) \rangle}{\langle I(t_0) \rangle^2} \tag{2.3}$$

where $I(t_0)$ and $I(t_0 + t)$ are the electromagnetic fields intensity evaluated at two different times and the average is carried out over time.
The light intensity is equal to the square of the electric field amplitude:

$$I \propto E^{(+)}(t) \cdot E^{(-)}(t) \tag{2.4}$$

where $E^{(+)}$ and $E^{(-)}$ are the positive and negative frequency components of the field. In quantum mechanics this expression can be redefined using the *creation* and *annihilation operators*, respectively $\widehat{a}^\dagger$ and $\widehat{a}$:

$$E^{(+)}(t) \propto \widehat{a} \qquad E^{(-)}(t) \propto \widehat{a}^\dagger \tag{2.5}$$

So the equation (2.3) becomes:

$$g^{(2)}(t) \propto \frac{\langle E^{(-)}(t) \cdot E^{(-)}(t+\tau) \cdot E^{(+)}(t) \cdot E^{(+)}(t+\tau) \rangle}{\langle E^{(-)}(t) \cdot E^{(+)}(t) \rangle \cdot \langle E^{(-)}(t+\tau) \cdot E^{(+)}(t+\tau) \rangle} \tag{2.6}$$

Considering small values of t ($t \to 0$) and using the above operators, the following expression is obtained:

$$g^{(2)}(0) \propto \frac{\langle \widehat{a}^\dagger \cdot \widehat{a}^\dagger \cdot \widehat{a} \cdot \widehat{a} \rangle}{\langle \widehat{a}^\dagger \cdot \widehat{a} \rangle \cdot \langle \widehat{a}^\dagger \cdot \widehat{a} \rangle} \tag{2.7}$$

Taking into account the bosonic commutator:

$$[\widehat{a}^\dagger, \widehat{a}] = \widehat{a}^\dagger \cdot \widehat{a} - \widehat{a} \cdot \widehat{a}^\dagger = 1 \tag{2.8}$$

and introducing *the number operator*:

$$n = \widehat{a}^\dagger \cdot \widehat{a} \tag{2.9}$$

Is possible to obtain:

$$g^{(2)}(0) \sim \frac{\langle \widehat{a}^\dagger \cdot (\widehat{a} \cdot \widehat{a}^\dagger - 1) \cdot \widehat{a} \rangle}{\langle \widehat{a}^\dagger \cdot \widehat{a} \rangle \cdot \langle \widehat{a}^\dagger \cdot \widehat{a} \rangle} = \frac{\langle n^2 \rangle - \langle n \rangle}{\langle n \rangle^2} \tag{2.10}$$

where $\langle n \rangle$ is the mean value of the photon.
If the light source consists of a single photon emitter, then n = 1 and therefore the function vanishes: $g^{(2)} = 0$. If it were possible to produce 2 photons simultaneously (as for example in the case of an agglomeration of 2 single photon emitters), then $g^{(2)} = 0.5$ and so on.
It is important to underline that these results represent an ideal cases, while the experimental procedure presents non-idealities such as background noise and dark counts from the detectors, which can invalidate the result if not properly taken into account. Typically it is sufficient that the value of $g^{(2)}$ turns out to be < 0.5 to conclude that it is a single photon source. In the low-photon-flux regime, this parameter is equivalent to Grangier's parameter α [7], defined as the ratio between the photon coincidence probability and the product of the single photon detection probabilities at the output of a Hanbury-Brown & Twiss interferometer, which is the typical approach used to estimate $g^{(2)}$ experimentally. This parameter $g^{(2)}$, can be extended to any order K by defining $g^{(K)}$:

$$g^{(K)}(0) = \frac{\langle n(n-1)...(n-K+1) \rangle}{\langle n \rangle^K} \tag{2.11}$$

2.2.2 Parameter $\theta^{(K)}$ to quantifying SPSs in presence of strong classical light

Recent years have seen an impressive advancement of quantum technology in the optical domain [8, 9, 10, 11, 12] and single-photon metrology [13] up to a point where the associated techniques are not anymore restricted to scientific labs, but are starting to effectively penetrate in the industry [14, 15], in the world-wide market [16], ultimately approaching everyday's life. As a consequence, it is of the utmost importance to develop simple methods [17, 18, 19, 20, 21, 22, 23, 24] to characterize optical states that are significantly more complex than that of the proof-of-principle single isolated quantum systems (with possible addition of a small amount of background).

Composite and application-driven quantum systems require an appropriate characterization. Such systems are significantly affected by inevitable noise and decoherence effects occurring when the system is moved from a controlled lab-like environment to the real-world. From a theoretical point of view, devising reliable and robust non-classicality criteria for such quantum systems is a topic of high interest [25, 26, 27, 28]. For instance, the characterization of ensembles of single-photon sources (SPSs) [18, 29, 30] in the presence of strong backgorund noise is considered. The most widespread techniques for the characterization of quantum optical states are based on the measurement of second order Glauber's autocorrelation function $g^{(2)}$, defined in the section 2.2.1. and typically used to intuitively assess the nonclassicality of optical sources.

This parameter $g^{(2)}$ (or Grangier's parameter α), can immediately be extended to any order K by defining $g^{(K)}$ (see Eq.(2.11)) as the ratio of the probability of a K-fold coincidence divided by the product of K single click probabilities of K non-photon-number-resolving (non-PNR) detectors attached to the output ports of a generalized multiport Hanbury-Brown & Twiss interferometer (HBTI). Operationally, such an HBTI can be comprised of cascaded two-ports beam splitters [31, 32, 33, 34, 35, 36, 37]. One of the main advantages of the $g^{(K)}$ parameter is that its value does not depend on the splitting ratio among the HBTI arms, on the overall losses and on the detection efficiency of the detectors comprising the HBTI.

The experimental measurement of $g^{(K)}$ has proven to be a useful resource in quantum optics. It has been demonstrated how to identify, by simultaneously sampling multiple-order $g^{(K)}$'s (in the specific case, $K = 2, 3, 4$), the underlying mode structure of complex multimode fields such as the superposition of a SPS emission with thermal fields, or a multi-thermal field with a Poissonian field, a task that cannot be achieved by only measuring $g^{(2)}$ [38]. This useful technique presents some limitations, emerging for instance when the fields to be reconstructed are composed by one or more distinct SPSs in presence of Poissonian or both thermal and Poissonian background noise. A situation of interest, e.g., when trying to identify single-photon emission due to color centers in diamond. Furthermore, some "a priori" knowledge on the state to be reconstructed (e.g., the number and types of modes composing

it) is needed to achieve reliable results.
Lately, a new criterion for assessing optical sources nonclassicality, mainly focused on clusters of single-photon emitters, has been proposed [39] and successfully implemented to test SPSs based on emitters such as color centers [40], trapped ions [41] and colloidal CdSe/CdS dot-in-rods[42]. This criterion is based on the measurement of a parameter, $\theta^{(K)}$, defined as:

$$\theta^{(K)}(0) = \frac{Q(0^{\otimes K})}{(Q(0))^K}, \tag{2.12}$$

where $Q(0)$ and $Q(0^{\otimes K})$ are, respectively, the probability of no-photon detection at the end of one arm and in K HBTI arms simultaneously. The parameter $\theta^{(K)}$ has an interesting properties: the $\theta^{(K)}$ value is not affected by the presence of Poissonian light, so that it can be extremely valuable in the characterization of photoluminescent emitters [43, 44, 45, 46, 47, 48, 49, 50, 51], since such a parameter would be insensitive to residual back-reflected excitation laser light. As a drawback, $\theta^{(K)}$, contrarily to $g^{(K)}$, strongly depends on the experimental apparatus, i.e. the BSs splitting ratio, the optical transmission of the HBTI and detection efficiencies of the detectors involved.

2.3 SPSs charactherization theory

Once a SPS has been identified using the autocorrelation function criterion or using the $\theta^{(K)}$ parameter, it is advisable to characterize its emission in order to have a complete description of the source. In particular, the emission of a SPS can mainly be described using the following parameters: lifetime, saturation power and asymptotic emission intensity. The lifetime (τ) is defined as the average time between the excitation of the source and the subsequent relaxation through the emission of a photon. As defined, the lifetime determines an important characteristic of a SPS, namely the emission rate ($1/\tau$). As regards the saturation power (P_{sat}), this quantity indicates the excitation power beyond which the emission of the source tends to a constant value. The maximum intensity obtained in this condition is defined as the asymptotic emission intensity (I_∞). In order to obtain these quantities, mathematical models are used which describe a SPS in a simplified way. The simplest is the 2-level model.

2.3.1 SPS two-levels model

Normally a SPS can be well described by two energy levels model: a fundamental level (here called 1) and an excited one (2). These levels are separated by a $\Delta E = E_2 - E_1 = h\nu_0$ and their occupation probabilities, also called populations, are indicated respectively as n_1 and n_2.
Initially it is assumed that the system is prepared in its ground state. Therefore, the following relations hold for populations at $t = 0$:

$$\begin{cases} n_1(t) + n_2(t) = 1 \quad \forall t \\ n_1(0) = 1 \\ n_2(0) = 0 \end{cases} \tag{2.13}$$

By exciting the system non-resonantly with a laser of frequency $\nu_1 > \nu_0$, the system transitions to a vibrational level and subsequently relaxes non-radiatively to the excited level (2). From this level the source can then transition to the ground state (1) by emitting a photon, see Figure 2.1.

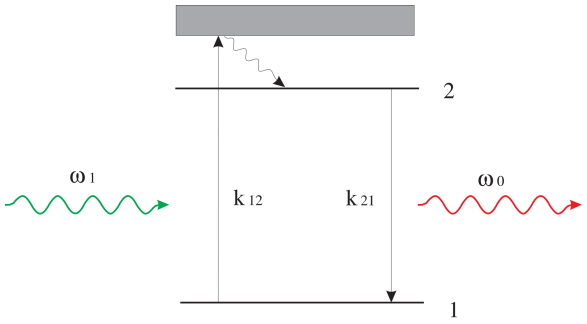

Figure 2.1: Representation of a SPS according to the two-level model

The dynamics of the populations of the two levels, neglecting the vibrational one, is described by the following equations:

$$\begin{cases} \dot{n}_1(t) = -k_{12}n_1(t) + k_{21}n_2(t) \\ \dot{n}_2(t) = +k_{12}n_1(t) - k_{21}n_2(t) \end{cases} \tag{2.14}$$

where k_{12} indicates the probability per unit of time that a photon is promoted from the 1 level to 2 and, conversely, k_{21}, the probability per unit time that a photon spontaneously relaxes from the level 2 to 1. The first of these two

quantities is directly proportional to the excitation power P, so $k_{12} = \alpha P$. The second can be written according to the *lifetime* τ of the source. In fact, if we imagine turning off the exciter pump at a time $t = 0$, the system of equations reduces to $\dot{n}_2(t) = -k_{21} n_2(t)$, the whose solution is a decreasing exponential with $\tau = \frac{1}{k_{21}}$.
In the general case, solving the previous system of equations for n_2, we obtain that the level 2 population can be expressed as follows:

$$n_2(t) = n_2(\infty)(1 - e^{-\lambda t}) = \frac{k_{12}}{\lambda}(1 - e^{-\lambda t}) \tag{2.15}$$

where $\lambda = k_{12} + k_{21}$ and $n_2(\infty)$ indicates the population of the excited level in the stationary case, i.e. when the excitation pump has been on for a long time.
We can relate the expression just found with the second order autocorrelation function, described in section 2.2.1. The autocorrelation function described in Eq.(2.3), can be rewritten by making explicit $I(t_0)$, intensity of the source in stationary conditions, and $I(t_0 + t)$, intensity after a time t from the photon emission, as the number of photons emitted per time unit, the following relations are obtained:

$$\begin{cases} I(t_0) \equiv I & = \eta_r \cdot k_{21} \cdot n_2(\infty) \\ I(t_0 + t) & = \eta_r \cdot k_{21} \cdot n_2(t) \end{cases} \tag{2.16}$$

with η_r detector efficiency of the instrumental apparatus. Inserting these last expressions in Eq.(2.3), we obtain:

$$g^{(2)}(t) = \frac{n_2(t)}{n_2(\infty)} = 1 - e^{-\lambda t} \tag{2.17}$$

Below, in Figure 2.2, the graph of the autocorrelation function obtained is shown.

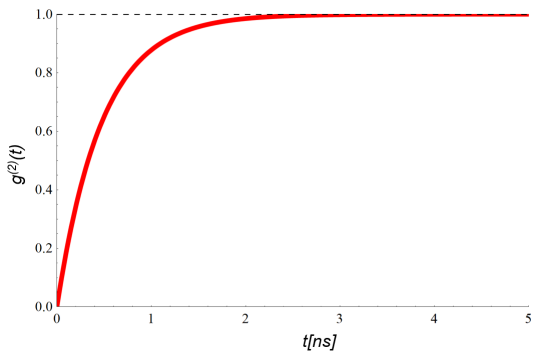

Figure 2.2: Trend of the autocorrelation function predicted by the two-level model for a SPS.

By studying the number of correlations as the time varies between the emission of the first photon and the detection of the second, it is possible to obtain parameters necessary for the characterization of the sources, such as the *lifetime*. By interpolating the graph it is possible to obtain the argument of the exponential λ of Eq.(2.17) at different pump laser power values. Once the $\lambda(P)$ values are known, a linear interpolation can be performed and the parameter of interest can be obtained. For convenience, the report is reproduced:

$$\lambda = k_{12} + k_{21} = \alpha P + \frac{1}{\tau} \tag{2.18}$$

To complete the characterization, it is interesting to obtain the saturation power P_{sat} and the asymptotic emission intensity I_∞ of a SPS, which are related to the intensity by the following relationship:

$$I = I_\infty \cdot \frac{P}{P + P_{sat}} \tag{2.19}$$

Comparing this definition with the terms in Eq.(2.16), in which the expression of $n_2(\infty)$ (see Eq.(2.15), of reported below:

$$I = \eta_r \cdot k_{21} \cdot \frac{\alpha P}{\alpha P + k_{21}} = \eta_r \cdot k_{21} \cdot \frac{P}{P + \frac{k_{21}}{\alpha}} \tag{2.20}$$

From this expression it can be easily seen that the saturation power is none other than the term $\frac{k_{21}}{\alpha}$ and that, in the same way, the asymptotic emission intensity is given by $\eta_r \cdot k_{21}$.
By measuring the emission intensity as a function of the power and performing a suitable interpolation, it is also possible to obtain the saturation power

and the asymptotic emission intensity of a SPS [52].
The model just illustrated describes the SPS as two-level structures in which the only transitions involved are radiative. Even if this condition is hardly satisfied in practice, since the inevitable interactions between the SPS and the surrounding environment lead to the presence of non-radiative transitions, it is often sufficient to understand the characteristics of the source. Alternatively, one can imagine describing the SPS as a three-level structure: a fundamental level, an excited level, and a metastable intermediate level. However, the procedure is the same.

Chapter 3

Single photon source characterization

In this chapter the results obtained on the characterization of single photon sources (SPSs) are described.
The first result concerns the theoretical study on the SPSs statistical distribution of the photon emission. While in pulsed laser regime the well-known sub-Poissonian statistic is obtained, it is shown here how the same statistic can be obtained by subjecting the source to a continuous laser. This statistic, index of the quantum nature of the source, can potentially occur when the emission and relaxation rates are comparable and the experimental conditions are such as to guarantee an almost ideal collection of photons.
The second result concerns a practical application of the theoretical model described in the previous chapter. From the experimental results it can be deduced that the glauber function $g^{(K)}$ and the theta parameters $\theta^{(K)}$ simultaneously can be an excellent method to resolve the optical states and trace the presence of single photon sources, even when immersed in a bath of thermal and Poissonian light.

3.1 Statistical emission in pulsed laser regime

As reported in the previous chapter, the presence of a SPS (and therefore the sub-Poissonianity of the emitted photon statistics) can be observed from the second order autocorrelation function by analyzing its emission for measurement times of the order of the lifetime of the source itself, or ps/ns. For longer measurement times, this function does not provide any indication on the distribution of the photons emitted. The method that is adopted involves

directly deriving the mathematical expression of the average value and the variance of the number of photons emitted and, from their comparison, the type of emission statistics is then established. This method is well developed in the scientific literature to describe the emission of a SPS excited with a pulsed laser [53, 54, 55]. The procedure with which the SPS emission statistics is derived in the pulsed laser regime is reported here.
Let us consider the excitation of a SPS with a laser that emits pulses at a frequency f. In a measurement time T, the system receives N pulses, where $N = f \cdot T$. By defining q the pumping efficiency, that is the probability for the SPS transition from its fundamental level to the excited one, given an incident pulse. Assuming that the system has a unitary quantum efficiency, which implies that the source always transits radiatively to the ground level once prepared in its excited level. In this case, the emission process is binomial and the probability of extracting from the system n photons given N incident pulses is given by the following distribution:

$$\mathcal{B}(n\,|N,\,q) = \frac{N\,!}{n\,!\,(N-n)\,!} q^n (1-q)^{N-n} \tag{3.1}$$

In this case, exploiting the normalization relation $\sum_{n=0}^{N} \mathcal{B}(n\,|N,\,q) = 1$, it can be shown that for the binomial distribution in 3.1 the following expressions are satisfied:

$$\big\langle n \big\rangle = Nq \qquad Var[n] = (1-q)\big\langle n \big\rangle \tag{3.2}$$

Since the pumping efficiency q is typically lower than 1, it follows that for a SPS excited with a pulsed laser the emission statistic is of the sub-Poissonian type since $Var[n] < \big\langle n \big\rangle$ [53].

This same behavior is obtained even if the non-ideal nature of the instruments used to detect the photons is taken into account. In fact, this is demonstrated below by taking into consideration the effects of both the efficiency and the dead time of the detectors.
First, imagine detecting the photons emitted by the source with a detector with an efficiency η_r lower than 100%. In this case, the probability of counting a photon is given by the convolution of the pumping efficiency with the instrumental one. This quantity, in fact, must take into account both the

probability of the system of emitting a photon, given a pump pulse, and the probability of the instrument detecting it. Consequently, the probability of extracting from the system n photons given N incident pulses becomes:

$$\mathcal{B}(n\,|N,\,q\,\eta_r) = \frac{N\,!}{n\,!\,(N-n)\,!}(q\,\eta_r)^n(1-\,q\eta_r)^{N-n} \tag{3.3}$$

Also the expressions given in Eq.(3.2) become:

$$\big\langle n\big\rangle = Nq\,\eta_r \qquad Var[n] = (1-q\,\eta_r)\big\langle n\big\rangle \tag{3.4}$$

Since η_r is assumed to be less than unity, then again we find that $Var[n] < \big\langle n\big\rangle$. Also in this case, therefore, the emission statistics are of the sub-Poissonian type [54].
Considering now the case of a further non-ideal element: a detector which has a dead time D different from 0. (This quantity will be described in more detail in the section 3.2.4.2). In this case, the probability of detecting a photon becomes $q' = \frac{q\,\eta_r}{1+Int(fD)\,q\,\eta_r}$, where Int indicates the mathematical operation selection of the integer part of the number between brackets [55]. Consequently, the binomial distribution takes the form $\mathcal{B}(n\,|N,\,q')$ and the expressions reported in Eq.(3.4) become:

$$\big\langle n\big\rangle = \frac{Nq\,\eta_r}{1+Int(fD)\,q\,\eta_r} \qquad Var[n] = (1-q\,\eta_r)\big\langle n\big\rangle$$

Also in this case we obtain the result $Var[n] < \big\langle n\big\rangle$.
From these examples, therefore, it emerges that the non-ideal elements accentuate the sub-Poissonian behavior of the emission statistic of a SPS excited with a pulsed laser with respect to the ideal case.

3.2 Statistical distribution of a SPS in continous laser regime

Depending on the properties of the light source, three statistical distribution regimes can be obtained in photon counting measurements: Poissonian, super-Poissonian and sub-Poissonian. These regimes are defined by the relationship between the variance Var[n] and the average number $\langle n\rangle$ of photon

counts for the corresponding distribution. For super-Poisson statistics typical of less coherent sources such as LEDs: $Var[n] > \langle n \rangle$; for Poissonian statistics characteristic of coherent light sources such as lasers: $Var[n] = \langle n \rangle$ and for sub-Poisson statistics characteristic of quantum lights: $Var[n] < \langle n \rangle$. Experimentally, by measuring the source light intensity for a time T, from the count of emitted photons, and repeating the measurement n times, it is possible to clarify the nature of the analyzed source.
The autocorrelation function evaluated at $t = 0$ can be easily rewritten in order to make explicit the variance and the average number dependence, starting from Eq.(2.10):

$$g^{(2)}(0) = \frac{\langle n^2 \rangle - \langle n \rangle^2 + \langle n \rangle^2 - \langle n \rangle}{\langle n \rangle^2} = \frac{Var[n] + \langle n \rangle^2 - \langle n \rangle}{\langle n \rangle^2} = \frac{Var[n] - \langle n \rangle}{\langle n \rangle^2} + 1 \tag{3.5}$$

The request for a $g^{(2)}(0) = 0$ to identify an SPS is in accordance with the sub-Poissonianity request $Var[n] < \langle n \rangle$. Provided that the measurement is performed for a time T of the order of its $lifetime\, \tau$ the emission statistic is sub-Poissonian.
On the other hand, when a measurement is carried out experimentally on macroscopic times $T >> \tau$, there is currently no mathematical description capable of determining the relationship that links the variance and the average value of the number of photons emitted. In this section, a new method is set out for directly deriving the mathematical expression of variance and mean value. This procedure is already developed in the literature for the description of the emission of an SPS excited with a pulsed laser [53, 54, 55], while it is absent in the continuous excitation regime.

3.2.1 Emission probability

To obtain the variance Var[n] and the average number $\langle n \rangle$ of photon counts, it is necessary to derive the probability that the source has to emit a photon following laser excitation.
Let us assume that a SPS, initially prepared in its fundamental level ($|m_s = 0\rangle$ in the case of the NV center), is subjected to continuous excitation. The electronic state spends a characteristic time (lifetime τ) in the excited level and then relaxes by returning to the ground-state (see section 1.2.2). It can be

assumed that the photon emission is a random event and that successive emissions are independent of each other. This process has a Poissonian nature. Setting $\mu_2 = 1/\tau$ the emission rate, the probability density functions of the photon emission process in the time window between t and $t + dt$ is:

$$f_{em}(t)\,dt = \mu_2\, e^{-\mu_2 t}\,\theta(t)\,dt \tag{3.6}$$

where $\theta(t)$ is the Heaviside symbol.
The same can be considered for the case of the absorption of pump photons. In fact, also this process has a Poissonian nature. Setting μ_1 the absorption rate of the pump photons, the probability density functions that the photon is absorbed between t and $t + dt$ is given by:

$$f_{ex}(t)\,dt = \mu_1\, e^{-\mu_1 t}\,\theta(t)\,dt \tag{3.7}$$

In order to model the overall behavior of an SPS, however, it is not sufficient to treat the absorption and emission process separately. Instead, it is necessary to consider that photons are emitted only if a pump photon is first absorbed. Consequently, in this case the probability that the first photon emitted falls between t and $t + dt$, given the previous emission at $t = 0$, is obtained from the convolution of $f_{em}(t)$ e $f_{ex}(t)$ as follows:

$$f(t)\,dt = \iint f_{em}(t')\, f_{ex}(t'')\,\delta(t - t' - t'')\,dt'\,dt'' = \frac{\mu_1\,\mu_2}{\mu_1 - \mu_2}(e^{-\mu_2 t} - e^{-\mu_1 t})\,\theta(t)\,dt \tag{3.8}$$

The goal becomes to establish the emission statistics of the process described by Eq(3.8). We can immediately identify two regimes in which the statistic is of the Poissonian type, that is $Var[n] = \langle n \rangle$. In fact, if absorption prevails ($\mu_1 \gg \mu_2$), $f(t)$ tends to be equal to $f_{ex}(t)$. In this condition the process is of the Poissonian type as well as its emission statistic. The same situation also occurs if the emission ($\mu_2 \gg \mu_1$) prevails since $f(t)$ tends to be equal to $f_{em}(t)$. As far as the intermediate regime is concerned, there is no indication to determine the type of statistic. It is therefore necessary to explicitly derive the mean value and variance of the number of photons emitted.

3.2.2 Probability generating function

In order to derive the moments of the number of photons emitted distribution, is necessary know the probability $P_T(n)$ of having n photons emitted in a time

interval T. Once this expression is determined, it will be possible to derive the average number of photons emitted in a time T as $\langle n \rangle = \sum_n n\, P_T(n)$. With the same procedure it is also possible to derive the higher order moments. The procedure by which these quantity can be derived is shown below.
First of all, taking advantage of the knowledge of the $f(t)$ function reported in Eq.(3.8), the probability of having the $n-th$ photon emitted in a time interval between t and $t+dt$ is derived. This quantity is obtained from the convolution of a number n of $f(t_i)$ and is denoted by $f_n(t)$, where $t = \sum_{i=1}^{N} t_i$. Subsequently, from this expression we derive the probability that the $n-th$ photon is emitted in the time interval $[0, T]$. This quantity can be expressed as follows:

$$K_N(T) = \int_0^T f_n(y)dy \tag{3.9}$$

The expression just presented for $K_n(T)$ can be obviously rewritten as the sum of the probabilities of issuing *at least* n photons in T:

$$K_N(T) = \sum_{n=N}^{\infty} P_T(n) \tag{3.10}$$

This implies that $P_T(n)$ can be simply obtained as:

$$P_T(N) = K_N(T) - K_{N+1}(T) \tag{3.11}$$

As can be easily observed, this last equation links $P_T(n)$ to the convolution of n probability density functions $f(t)$, that are known quantities. Consequently, the expression in (3.11) can be used to derive, in principle, all moments of the number of emitted photons distribution. However, due to the computational difficulty due to the convolutions involved, it is convenient in this case to adopt a different approach. The probability generating function is used to derive the desired moments. Before getting to the heart of this alternative approach, however, it is considered appropriate to report the definition and some properties of this function.

In general, given a discrete variable n, the probability generating function is defined as a power series in which the coefficient associated with the $n-th$ term is the probability $P(n)$. In the case under analysis, it takes the following

form:

$$G(t,\xi) = \sum_{n=0}^{\infty} P_t(n)\,\xi^n \tag{3.12}$$

This last equation can then be rewritten differently by making explicit the $P_t(n)$ coefficients. The final result of this replacement is shown below.

$$G(t,\xi) = 1 + \sum_{n=1}^{\infty} K_n(t)(\xi - 1)\,\xi^{n-1} \tag{3.13}$$

This alternative expression contains in $K_n(t)$ the only quantity known so far, that is the function $f(t)$.
Once the probability generating function has been defined, it should be noted that this function has some very interesting properties. In particular, starting from its analytical expression it is possible to derive directly the probabilities $P_t(n)$ and the moments of the associated distribution. In fact, the following relations hold:

$$P_t(n) = \frac{1}{n\,!}\frac{\partial^n}{\partial \xi^n} G(t,\xi)\,\Big|_{\xi=0} \tag{3.14}$$

$$\big\langle n \big\rangle = \frac{\partial}{\partial \xi} G(t,\xi)\,\Big|_{\xi=1} \tag{3.15}$$

$$\big\langle n(n-1) \big\rangle = \frac{\partial^2}{\partial \xi^2} G(t,\xi)\,\Big|_{\xi=1} \tag{3.16}$$

$$Var[n]_t = \big\langle n(n-1) \big\rangle + \big\langle n \big\rangle - \big\langle n \big\rangle^2 \tag{3.17}$$

From what has just been described it may seem that the use of the probability generating function to derive the distribution moments leads to the same problems as the initial approach. In fact, in Eq.(3.13) there are however n convolutions of $f(t)$. However, unlike the previous case, it is possible to overcome this limit by using the Laplace transforms. In fact, the Laplace transform of the probability generating function presents a very simple mathematical expression since it contains only the transform of $f(t)$, which is denoted by $\widetilde{f}(s)$. This result is reported below:

$$\widetilde{G}(s,\xi) = \int_0^{\infty} G(t,\xi) e^{-st}\,dt = \frac{1}{s}\,\frac{1 - \widetilde{f}(s)}{1 - \xi\,\widetilde{f}(s)} \tag{3.18}$$

The probabilities $P_t(n)$ and the moments of the associated distribution can also be easily calculated starting from this new expression and analytically calculating the Laplace anti-transform. The new relationships of interest are as follows:

$$P_t(n) = \mathcal{L}^{-1}\left[\frac{1}{n\,!} \frac{\partial^n}{\partial \xi^n} \widetilde{G}(s,\xi) \,\Big|_{\xi=0} \right] \tag{3.19}$$

$$\big\langle n \big\rangle = \mathcal{L}^{-1}\left[\frac{\partial}{\partial \xi} \widetilde{G}(s,\xi) \,\Big|_{\xi=1} \right] \tag{3.20}$$

$$\big\langle n(n-1) \big\rangle = \mathcal{L}^{-1}\left[\frac{\partial^2}{\partial \xi^2} \widetilde{G}(s,\xi) \,\Big|_{\xi=1} \right] \tag{3.21}$$

Precisely these properties make it advantageous to use this alternative approach to the one presented initially.

To summarize, this alternative approach involves deriving the probabilities $P_t(n)$ and the moments of the associated distribution by following these steps:

- the Laplace transform of $f(t)$ is first computed;
- the found expression is subsequently replaced in Eq.(3.18) so as to derive the Laplace transform of $G(t,\xi)$;
- finally, the desired quantities are derived using the Eq.(3.17) and Eqs.(3.19) - (3.21).

3.2.3 Mean value and the variance derivation of the distribution of the number of photons emitted by an SPS

Using the general approach described in the previous section to determine the statistical moments of a probability distribution, the procedure is applied to the case in which the probability density function $f(t)$ is the one presented in Eq.(3.8). Consequently, the Laplace transform of $f(t)$ is initially computed, obtaining:

$$\widetilde{f}(s) = \frac{\mu_1 \mu_2}{(\mu_1 + s)(\mu_2 + s)} \tag{3.22}$$

This expression is used to derive the Laplace transform of the probability generating function by applying the equation (3.18). The following expression

is obtained:

$$\widetilde{G}(s,\xi) = \frac{s+\mu_1+\mu_2}{s^2+(\mu_1+\mu_2)s-\mu_1\mu_2(\xi-1)} \tag{3.23}$$

At this point, it is possible to proceed by calculating the average value and the variance of the distribution of the number of photons emitted by an SPS, in order to obtain the type of emission statistic for macroscopic measurement times. Eq.(3.19) is used to derive the average value, obtaining:

$$\langle n \rangle = \frac{\mu_1\mu_2}{(\mu_1+\mu_2)^2}\left(e^{-(\mu_1+\mu_2)\,t} + (\mu_1+\mu_2)\,t - 1\right) \tag{3.24}$$

Of the latter expression, however, only the behavior for $t \to \infty$ is concerned. In fact, studying the system for macroscopic times, i.e. at the laboratory scale, means working on time scales of ms/s. These scales for an SPS are comparable to an infinite time since the characteristic times of these emitters are of the order of *lifetime* ($\mu s/ns$). Here is the expression of $\langle n \rangle_t$ for $t \to \infty$.

$$\langle n \rangle = \frac{\mu_1\mu_2}{(\mu_1+\mu_2)}\,t \tag{3.25}$$

Subsequently, the variance of the distribution of the number of photons emitted is also obtained and for the sake of brevity only the result for $t \to \infty$ is reported.

$$Var[n] = \frac{\mu_1^2+\mu_2^2}{(\mu_1+\mu_2)^2}\,\langle n \rangle \tag{3.26}$$

At this point, having known all the quantities required, it is possible to derive the type of emission statistic for $t \to \infty$. For convenience, the ratio is calculated:

$$\frac{Var[n]}{\langle n \rangle} = \frac{\mu_1^2+\mu_2^2}{(\mu_1+\mu_2)^2} = \frac{1+\left(\frac{\mu_1}{\mu_2}\right)^2}{\left(1+\frac{\mu_1}{\mu_2}\right)^2} \tag{3.27}$$

If its value is equal to 1, the relation $Var[n] = \langle n \rangle$ holds, which implies that there is a Poissonian emission. If this ratio is less than or greater than 1, it is evident that the statistic is of the sub-Poissonian or super-Poissonian type, respectively. The graph in Figure 3.1 plots Eq.(3.27) as a function of the ratio $\frac{\mu_1}{\mu_2}$.

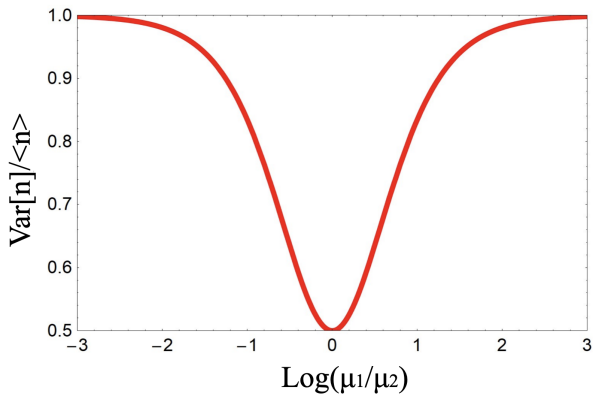

Figure 3.1: $\frac{Var[n]}{<n>}$ as a function of the logarithm of $\frac{\mu_1}{\mu_2}$.

To confirm the validity of this approach, it clearly emerges from the graph that the emission statistic is Poissonian both in the case in which the absorption prevails ($\mu_1 \gg \mu_2$) and in the opposite one in which the emission is predominant ($\mu_2 \gg \mu_1$). This result is in line with what has already been mentioned. The really interesting result that can be deduced from the discussion and therefore from the 3.1 graph is that, when the emission and relaxation rates are comparable ($\mu_1 \sim \mu_2$), the emission statistic of an SPS excited with a continuous laser for macroscopic times is sub-Poissonian.

3.2.4 Effect of optical losses and detector dead time on the non-classical properties

This section explores how the results just obtained are modified by the non-ideality of the tools used to detect photons. In particular, the SPS emission statistic under continuous laser excitation in the presence of optical losses is derived below. Subsequently, this calculation is repeated taking into account the effect of the detectors dead time.

3.2.4.1 Statistical distribution of a SPS in presence of optical losses

In the presence of optical losses, it must be taken into account that, given n photons emitted, only a part of these is actually detected by the measuring apparatus. In order to model this effect, a detection efficiency η_r is introduced into the discussion. This quantity describes overall the non-ideal

elements that contribute to the losses. Among these contributions we can, for example, mention those non-radiative transitions that reduce the quantum efficiency η_Q of an SPS (the metastable level for example in the case of the NV center). Other contributions may be related to excitation efficiencies, photon extraction efficiencies, uncorrelated background photons, mode superpositions, beam-splitter losses, and also detectors efficiencies and dark counts.

Due to the presence of optical losses, the function $f(t)$ previously obtained no longer correctly describes the probability that the first photon detected falls in the interval $[0, t]$ given the previous emission at $t = 0$. Consequently, it is necessary to obtain this quantity in the new conditions in such a way as to be able to derive the emission statistics following the same approach adopted previously. To obtain the desired expression, it is appropriate to introduce a new probability of detecting k photons in a time interval t in the presence of optical losses. This quantity is indicated with the notation $P_{\eta_r}(k)$ and its mathematical expression can be linked to the known probability $P_t(n)$ to emit n photons at the same time, as follows:

$$P_{\eta_r}(k) = \sum_{n=k}^{\infty} P_t(n)\, \mathcal{B}(k\,|n, \eta_r) \tag{3.28}$$

As can be seen, the new probability $P_{\eta_r}(k)$ consists of a sum whose terms are the probabilities $P_t(n)$ weighted by the respective probabilities $\mathcal{B}(k\,|n, \eta_r)$ to reveal k photons, when n photons are emitted, and an overall optical efficiency equal to η_r. Furthermore, it should be noted that the sum runs on all integers greater than k in such a way as to take into account all the configurations that can give rise to k photons detected.

By setting $k = 1$, we can derive the probability that the first photon detected, in the presence of optical losses, falls in the interval $[0, t]$. In this way, the desired quantity is obtained, the expression of which takes the following form:

$$f_{\eta_r}(t) = \sum_{n=1}^{\infty} (1 - \eta_r)^{n-1}\, \eta_r\, f_n(t) \tag{3.29}$$

Once this quantity is known, the previously illustrated method can be applied to derive the emission statistic associated with it. In particular, the Laplace

transform of $f_{\eta_r}(t)$ is initially calculated and the final result is reported below.

$$\widetilde{f}_{\eta_r}(s) = \sum_{n=1}^{\infty}(1-\eta_r)^{n-1}\,\eta_r\,\widetilde{f}_n(s) = \frac{\eta_r \widetilde{f}(s)}{1-(1-\eta_r)\widetilde{f}(s)} = \frac{\eta_r \mu_1 \mu_2}{s^2+(\mu_1+\mu_2)s+\eta_r\mu_1\mu_2} \tag{3.30}$$

The latter expression is then used to derive the Laplace transform of the probability generating function. In fact, applying the Eq.(3.18) with $f_{\eta_r}(s)$ instead of $f(s)$, we obtain:

$$\widetilde{G}_{\eta_r}(s,\xi) = \frac{s+\mu_1+\mu_2}{s^2+(\mu_1+\mu_2)s+\eta_r\mu_1\mu_2(1-\xi)} \tag{3.31}$$

At this point, the moments can be calculated. In particular, using Eq.(3.19), the following expression is obtained for the average value, which is equal to the average value of the ideal case weighted for the η_r efficiency:

$$\big\langle n \big\rangle_{\eta_r} = \eta_r \,\frac{\mu_1\mu_2}{(\mu_1+\mu_2)^2}\big(e^{-(\mu_1+\mu_2)\,t} + (\mu_1+\mu_2)\,t - 1\big) = \eta_r \,\big\langle n \big\rangle \tag{3.32}$$

For macroscopic measurement times, that is for $t \to \infty$, the average value is equal to the previous case less the multiplication factor η_r.

$$\big\langle n \big\rangle_{\eta_r} = \eta_r \,\frac{\mu_1\mu_2}{(\mu_1+\mu_2)}\,t \tag{3.33}$$

Finally, the variance of the distribution of the number of photons emitted is obtained and, for the sake of brevity, only the result for $t \to \infty$ is reported.

$$Var[n]_{\eta_r} = \frac{\mu_1^2 + 2\,(1-\eta_r)\,\mu_1\mu_2 + \mu_2^2}{(\mu_1+\mu_2)^2}\,\big\langle n \big\rangle_{\eta_r} \tag{3.34}$$

At this point it is possible to derive the type of emission statistic, evaluating for convenience also in this case the ratio $\frac{Var[n]_{\eta_r}}{<n_{\eta_r}>}$, which for $t \to \infty$ takes the following expression:

$$\frac{Var[n]_{\eta_r}}{<\,n\,>_{\eta_r}} = \frac{\mu_1^2 + 2\,(1-\eta)\,\mu_1\mu_2 + \mu_2^2}{(\mu_1+\mu_2)^2} \tag{3.35}$$

As before, the latter equation is represented graphically as a function of the relationship $\frac{\mu_1}{\mu_2}$, see Figure 3.2. The graph was evaluated for three different

efficiency values η_r in such a way as to be able to visually evaluate the effect of optical losses on the type of emission statistic in the various regimes.

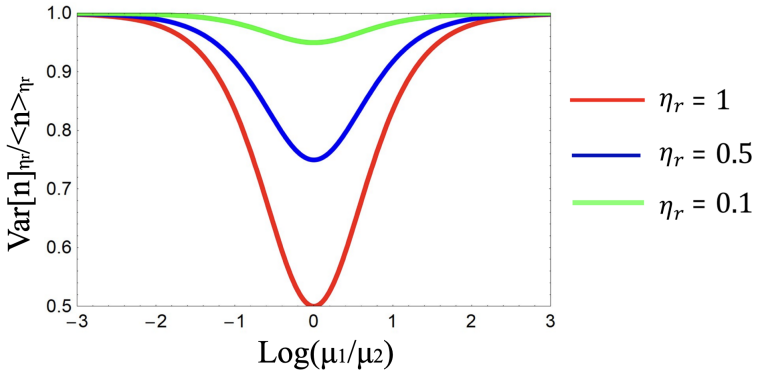

Figure 3.2: $\frac{Var[n]_{D,\eta_r}}{<n>_{D,\eta_r}}$ as a function of the logarithm of $\frac{\mu_1}{\mu_2}$.

As can be seen, the optical losses do not modify the shape of the curve, but progressively reduce the amplitude of the minimum with respect to the ideal case. Consequently, in the intermediate regime ($\mu_1 \sim \mu_2$), as η_r decreases, the statistic becomes less and less sub-Poissonian, tending towards the Poissonian case. In the other configurations, however, we always have $\frac{Var[n]_{\eta_r}}{<n>_{\eta_r}} = 1$ as expected.

3.2.4.2 Statistical distribution of a SPS in presence of optical losses and detector dead time

In addition to the optical losses, a further element of non-ideality is considered, that is the dead time of the detectors. They, after measuring a photon, take some time to restore the initial conditions and be ready for a new measurement. As a direct consequence, the photons hitting the instrument in this time interval are not detected and are therefore lost. For this very reason, this time is called *dead time*. Specifically we consider the effect of $dead-time$ in no-paralizable detectors such as SPAD detector operated in Geinger mode with active quenching circuit, that is the kind of detectors more used in this kind of application, and specifically, the one I used in my experiment.
Therefore, having known the effect of this non-ideal element on photon detection, it is evident that the previously obtained function $f_{\eta_r}(t)$ no longer correctly describes the probability that the first photon detected falls within

the interval $[0, t]$ given the previous revelation at $t = 0$. It is necessary to obtain this quantity in the current conditions in such a way as to be able to derive the emission statistics following the same approach adopted previously. In particular, said D the *dead time* of the detector, the probability must have the following form:

$$f_{D,\eta_r}(t) = A\, f_{\eta_r}(t)\, \theta(t - D) \tag{3.36}$$

To obtain $f_{D,\eta_r}(t)$, we need to specify the normalization constant A. To derive it, it is necessary to compute the Laplace antitransform of the function $\widetilde{f}_{\eta_r}(s)$, see appendix A.4, so as to obtain the expression of $f_{\eta_r}(t)$. The result obtained from this operation is the following:

$$f_{\eta_r}(t) = \frac{\eta_r \mu_1 \mu_2}{\sqrt{(\mu_1 + \mu_2)^2 - 4\eta_r \mu_1 \mu_2}(e^{-\frac{\mu_- t}{2}} - e^{-\frac{\mu_+ t}{2}})} \tag{3.37}$$

where $\mu_\pm = \mu_1 + \mu_2 \pm \sqrt{(\mu_1 + \mu_2)^2 - 4\eta_r \mu_1 \mu_2}$.
At this point, the constant A can be derived by imposing the normalization condition $\int_0^\infty A\, f_{\eta_r}(t)\, \theta(t - D)\, dt = 1$ and the resulting expression has the following form:

$$A = \frac{\sqrt{(\mu_1 + \mu_2)^2 - 4\eta_r \mu_1 \mu_2}}{2\eta_r \mu_1 \mu_2 \big(\frac{e^{-\frac{\mu_- D}{2}}}{\mu_-} - \frac{e^{-\frac{\mu_+ D}{2}}}{\mu_+}\big)} \tag{3.38}$$

Replaced in Eq.(3.36) the constant A, we get:

$$f_{D,\eta_r}(t) = \frac{e^{-\frac{\mu_- t}{2}} - e^{-\frac{\mu_+ t}{2}}}{2\left(\frac{e^{-\frac{\mu_- D}{2}}}{\mu_-} - \frac{e^{-\frac{\mu_+ D}{2}}}{\mu_+}\right)} \tag{3.39}$$

Once the expression of $f_{D,\eta_r}(t)$ s known, we can apply the method previously illustrated to derive the emission statistic associated with it. In particular, $\widetilde{f}_{D,\eta_r}(s)$ is initially calculated and the Laplace transform of the probability generating function is derived by applying Eq.(3.18) with $f_{D,\eta_r}(s)$ instead of $f(s)$ (not shown here).

At this point, we can calculate those moments of the distribution of the number of photons emitted. However, the Laplace antitransform present in

the formula for calculating the average value cannot be calculated analytically. This aspect, however, does not represent a limit for the discussion since the quantity we are interested in is the average value for $t \to \infty$. However, this expression can be derived by exploiting the following property of Laplace transforms:

$$\langle n \rangle_{D,\eta_r} = \lim_{t\to\infty} \frac{\partial}{\partial \xi} G(t,\xi)\big|_{\xi=1} = \lim_{s\to 0} \frac{\partial^2}{\partial \xi^2} \widetilde{G}(s,\xi)\big|_{\xi=1} t \tag{3.40}$$

The result obtained is the following:

$$\langle n \rangle_{D,\eta_r} = \frac{\mu_-\mu_+\left(\mu_- e^{-\frac{\mu_+ D}{2}} - \mu_+ e^{-\frac{\mu_- D}{2}}\right)}{\mu_-^2\,(2+\mu_+ D)\,e^{-\frac{\mu_+ D}{2}} - \mu_+^2 (2+\mu_- D)\,e^{-\frac{\mu_- D}{2}}} \tag{3.41}$$

The same to derive the variance of the distribution of the number of photons emitted (not shown here).
At this point it is possible to derive the ratio $\frac{Var[n]_{D,\eta_r}}{<n>_{D,\eta_r}}$. In particular, this quantity for $t \to \infty$ takes the following form:

$$\frac{Var[n]_{D,\eta_r}}{< n >_{D,\eta_r}} \sim \frac{1}{(1+< n >_{\eta_r} \frac{D}{t})^2} = \frac{1}{[1+\eta_r \frac{\mu_1}{\mu_2}(1+\frac{\mu_1}{\mu_2})D]^2} \tag{3.42}$$

This last equation is graphically represented as a function of the ratio $\frac{\mu_1}{\mu_2}$, with fixed efficiency and for different values of D, in such a way as to visually evaluate the effect of the detectors *dead time* on the type of emission statistic in the various regimes. The graph is represented in Figure 3.3.

The *dead time* of the detectors changes the shape of the curve with respect to the ideal case. In particular, when this quantity is different from 0, the trend is no longer symmetrical with respect to $\frac{\mu_1}{\mu_2}$. To confirm this aspect, the asymptotic trends of Eq.(3.42) for $\mu_1 \gg \mu_2$ and $\mu_2 \gg \mu_1$. Below are the results obtained by setting $D = k\tau$, with τ *lifetime* of the SPS.

$$\begin{cases} \frac{Var[n]_{D,\eta_r}}{<n>_{D,\eta_r}} \to \frac{1}{(1+\eta_r \frac{\mu_1}{\mu_2}(1-\frac{\mu_1}{\mu_2})\,k]^2} \to 1 \quad \text{per } \mu_2 \gg \mu_1 \\ \frac{Var[n]_{D,\eta_r}}{<n>_{D,\eta_r}} \to \frac{1}{(1+\eta_r k)^2} = cost < 1 \quad \text{per } \mu_1 \gg \mu_2 \end{cases} \tag{3.43}$$

Consequently, when the *dead time* is different from 0, the system exhibits a sub-Poissonian behavior extrinsic to the emission source and this trend tends

to affect more and more emission regimes as the value of D increases. In particular, for $D \ll \tau$ this effect is confined to the $\mu_1 \gg \mu_2$ regime only. On the contrary, for $D \geq \tau$ the non-ideality of the detectors also affects the region in which $\mu_2 \gg \mu_1$.

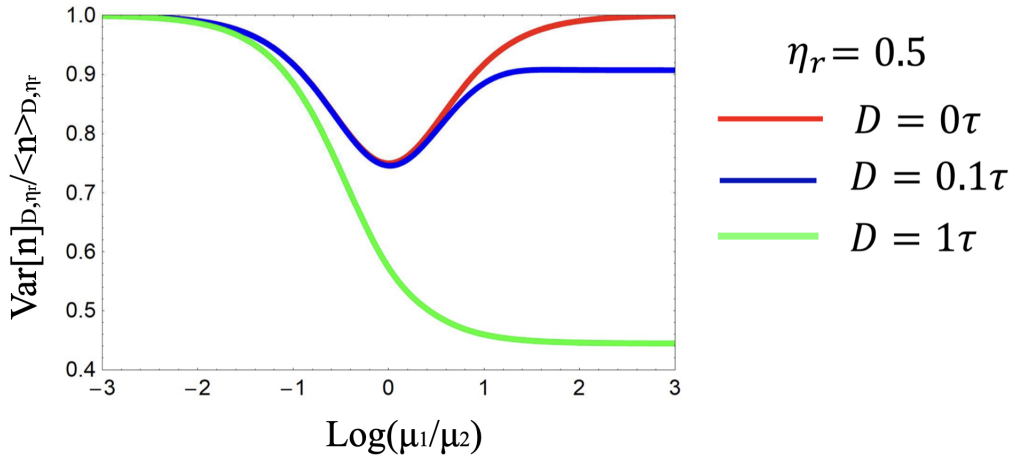

Figure 3.3: $\frac{Var[n]_{D,\eta_r}}{<n>_{D,\eta_r}}$ as a function of the logarithm of $\frac{\mu_1}{\mu_2}$.

3.2.5 Results discussion

For macroscopic measurement times $t \gg \tau$, the emission statistic of a SPS excited by a laser of continuous power is of type:

- Poissonian if the absorption rate or the emission rate prevails respectively;
- sub-Poissonian if the two processes are concurrent.

To experimentally measure the emission statistics of such a system, it is necessary to take into account the effect of those non-ideality elements treated in the previous section. In fact, the optical losses reduce the intrinsic sub-Poissonianity of the source, while the *dead time* of the detectors introduces an apparent sub-Poissonian behavior extrinsic to the system under analysis, an artifact. From a practical point of view, it is therefore necessary to work at high optical efficiencies and at *dead time* $D \ll \tau$. However, this last requirement severely limits the experimental verification of the model. In fact,

current detectors have *dead times* higher than the *lifetime* of an SPS. Typically their value is of the order of tens/hundreds of ns.

This model can offer a new measurement protocol for deriving the properties of such sources. In fact, it can be noted that in correspondence with the minimum of the curve shown in Figure 3.1, $\mu_1 = \mu_2$, that is $\alpha P = \tau^{-1}$ (see the parameters k_{12} and k_{21} in section 2.3.1). Consequently, a scan of the emission statistic as a function of the optical excitation power would allow to determine the SPS *lifetime* from the value of P corresponding to the minimum of $\frac{Var[n]}{<n>}$. This measurement protocol would be particularly competitive with respect to the methods currently used, requiring the use of a single detector and a reduction in measurement times since to obtain the SPS emission statistic would be sufficient times of ms order.

3.3 Reconstruction of optical states exploiting both the $g^{(K)}$ and $\theta^{(K)}$ parameters simultaneously

In the next sections an excellent method to resolve the optical states and trace the presence of single photon sources, even when immersed in a bath of thermal and Poissonian light, is illustated. Such a technique consists in applying the glauber function $g^{(K)}$ and the theta parameters $\theta^{(K)}$ simultaneously.

3.3.1 Theoretical model for $g^{(K)}(0)$ and $\theta^{(K)}(0)$ derivation

The physical phenomenon considered here (see Fig. 3.5) is the emission of multimode light from one or many different optical sources observed by $N = 4$ non-PNR detectors in a tree configuration. There we develop a general model for N arms HBTI assuming, for simplicity, that the photons are split in the N arms of the HBTI with equal probability $1/N$, and that each subsequent detector has identical system efficiency (including transmission losses and detection efficiency) η. This assumption does not qualitatively change the results. Let us define the characteristic function for a discrete probability

function p_n of having n photons in our system (with $\sum_{n=0}^{+\infty} p_n = 1$)

$$\Gamma(z) = \sum_{n=0}^{+\infty} p_n z^n \tag{3.44}$$

Accounting for the efficiency η, the characteristic function in Eq.(3.44) becomes:

$$\Gamma(z) = \sum_{n=0}^{+\infty} [1 - \eta(1-z)]^n p_n \tag{3.45}$$

See appendix B.1 for the derivation. From the characteristic function $\Gamma(z)$ one can estimate the moments of the distribution P_n:

$$\begin{aligned} \tfrac{d}{dz}\Gamma(z)\Big|_{z=1} &= \mathcal{E}\{n\}, \\ \tfrac{d^2}{dz^2}\Gamma(z)\Big|_{z=1} &= \mathcal{E}\{n(n-1)\}, \\ &\vdots \\ \tfrac{d^K}{dz^K}\Gamma(z)\Big|_{z=1} &= \mathcal{E}\big\{\tfrac{n!}{(n-K)!}\big\}, \end{aligned} \tag{3.46}$$

where $\mathcal{E}\{x\}$ represents the expectation value of the variable x. It is straightforward to show from Eqs. (3.46) that the generic $g^{(K)}(0)$ function can be expressed as:

$$g^{(K)}(0) = \left.\frac{\frac{d^K}{dz^K}\Gamma(z)}{\big(\frac{d}{dz}\Gamma(z)\big)^K}\right|_{z=1}. \tag{3.47}$$

Let us now suppose that we have a combination of several optical sources at once, with different statistical distributions. For instance, for M single-photon emitters with photon emission probability p, one thermal source and one Poissonian source (but the result can be generalized to any number and type), the total photon-number probability distribution reads:

$$p_n^{TOT} = \sum_{k,l,m} \delta_{n,(k+l+m)} P_k^{bin}(p, M) P_l^{th}(\nu) P_m^{poi}(\mu), \tag{3.48}$$

where the three sources have, respectively, binomial $\big(P_k^{bin}(p,M) = \binom{M}{k} p^k (1-p)^{M-k}\big)$, thermal $\big(P_l^{th}(\nu) = \frac{\nu^l}{(1+\nu)^{l+1}}\big)$ and Poissonian $\big(P_m^{poi}(\mu) = \frac{\mu^m e^{-\mu}}{m!}\big)$ photon

number distributions. For a multimode field, where each mode's statistical distribution is given by a characteristic function, the composite characteristic function $\Gamma^{TOT}(z)$ can be simply written as the product pf the characteristic functions

$$\Gamma^{TOT}(z) = \Gamma^{th}(z)\Gamma^{poi}(z)\Gamma^{bin}(z), \tag{3.49}$$

where $\Gamma^{th}(z)$, $\Gamma^{poi}(z)$ and $\Gamma^{bin}(z)$ are, respectively, the characteristic functions related to the thermal source, the coherent one and the SPS ensemble (see Eq.(3.45)). Thus, also the $g^{(K)}(0)$ values can be calculated from the characteristic function $\Gamma^{TOT}(z)$ from Eq.(3.47) and Eq.(3.49). To generalize the previous examples, here we consider multimode optical fields comprised of a total of S modes. Instead of requiring a priori knowledge on the photon number statistics of each of the S modes, we identify all possible S-mode combinations (with arbitrary statistics):

$$\Gamma^{TOT}(z) = \delta_{S,(j_{poi}+j_{bin}+j_{th})} \prod_{j=0}^{j_{poi}} \Gamma_j^{poi}(z) \prod_{j=0}^{j_{th}} \Gamma_j^{th}(z) \prod_{j=0}^{j_{bin}} \Gamma_j^{bin}(z) \tag{3.50}$$

(since the sum of multiple Poisson distributions is also a Poisson distribution, it is enough to consider only one Poissonian mode, i.e. $j_{poi} \leq 1$).
Let us now investigate the expression of the $\theta^{(K)}(0)$ function, defined in Eq.(2.12), for this multimode field. The no-click probability of the detector at the end of the i^{th} branch of a K-branch detector tree with n impinging photons can be calculated as the convolution of the probability of having k_i out of n photons in the i^{th} branch (governed by binomial distribution) and the probability of observing zero out of k_i incoming photons in the same branch ($\pi_i = (1-\eta)^{k_i}$, being η the detection efficiency of the detector):

$$Q_i(0|n) = \sum_{k_i=0}^{n} \frac{n!}{n!(n-k_i)!} \left(\frac{1-\eta}{K}\right)^{k_i} \left(1-\frac{1}{K}\right)^{n-k_i} = \left(1-\frac{\eta}{K}\right)^{n}. \tag{3.51}$$

Analogously, the probability of detecting zero out of n photons simultaneously in $K \leq N$ branches is the probability of a particular permutation of n photons over K branches of the detector-tree (governed by the multinomial distribution) multiplied by the joint probability of detecting zero photons in each branch ($\prod_i^K \pi_i$) considering all the possible photon distributions in the

K branches, i.e. all possible $\{k_i\}$ sets fulfilling the condition $\sum_{i=0}^{K} k_i = n$:

$$Q(0^{\otimes K}|n) = \sum_{\substack{k_1,\ldots,k_K \\ \left[\sum_{i=1}^{K} k_i = n\right]}} \frac{n!}{k_1!\ldots k_K!} \prod_{i=1}^{K} \left(\frac{1-\eta}{K}\right)^{k_i} = \left(\sum_{i=1}^{K} \frac{1-\eta}{K}\right)^{n} = (1-\eta)^n \ . \tag{3.52}$$

In order to calculate the terms in Eq.(2.12), the conditioned probabilities in Eqs.(3.51) and (3.52) must be averaged on the statistical distribution. In this case it can be shown, with a procedure analogous to the one leading to Eq.(3.49), that $Q^{TOT}(0)$ and $Q^{TOT}(0^{\otimes K})$ can be factorized as:

$$Q^{TOT}(0) = \sum_{n=0}^{\infty} (1 - \frac{\eta}{K})^n p_n^{TOT} = Q^{th}(0) Q^{poi}(0) Q^{bin}(0) \tag{3.53}$$

and

$$Q^{TOT}(0^{\otimes K}) = \sum_{n=0}^{\infty} (1-\eta)^n p_n^{TOT} = Q^{th}(0^{\otimes K}) Q^{poi}(0^{\otimes K}) Q^{bin}(0^{\otimes K}). \tag{3.54}$$

Thus, the $\theta^{(K)}(0)$ function can be calculated as:

$$\theta^{(K)}(0) = \frac{Q^{th}(0^{\otimes K}) Q^{poi}(0^{\otimes K}) Q^{bin}(0^{\otimes K})}{(Q^{th}(0) Q^{poi}(0) Q^{bin}(0))^K} = \frac{Q^{th}(0^{\otimes K}) Q^{bin}(0^{\otimes K})}{(Q^{th}(0) Q^{bin}(0))^K}, \tag{3.55}$$

where we used the property $Q^{poi}(0^{\otimes K}) = [Q^{poi}(0)]^K$, demonstrating that $\theta^{(K)}$'s insensitive to Poissonian light and, as a consequence, resilient to a Poissonian noise. Again, this result can be extended to an arbitrary number of sources of each type by simply including appropriate multipliers to the above factorized expression, in a similar manner to Eq.(3.50).

3.3.2 Experimental reconstruction

The technique described in the section 3.3.1 has been tested by applying it to several different multi-mode optical fields detected by our detector tree—SP, see section 3.3.3. The detector tree is composed of three 50:50 fiber beam splitters (FBSs) connected to $N = 4$ InGaAs/InP single-photon avalanche diodes (SPADs) in a tree configuration, allowing us to discriminate up to

four incoming photons.
We generate a multimode optical field combining, in our experimental setup (Figure 3.5), up to four optical modes (because of the $N = 4$ constraint on the detection side). The multimode field is produced by three different source types: a Poissonian (coherent) source, thermal source and single-photon source (see section 3.3.2 for details).
The reconstruction of the S-mode field is achieved by a minimization algorithm based on a least square difference between the theoretical $g^{(K)}$'s and $\theta^{(K)}$'s (labeled "rec") and the ones obtained in the experiment (labeled "exp"). Specifically, the function to be minimized is:

$$LS = \sum_{K=2}^{4} \lambda_g(K) \left(g_{\text{rec}}^{(K)}(0) - g_{\text{exp}}^{(K)}(0) \right)^2 + \lambda_\theta \sum_{K=2}^{4} \left(\theta_{\text{rec}}^{(K)}(0) - \theta_{\text{exp}}^{(K)}(0) \right)^2 \quad (3.56)$$

where λ_θ and $\lambda_g(K)$ are Lagrange multipliers, $g_{\text{rec}}^{(K)}(0)$ is given by Eq.(3.47) and $\theta_{\text{rec}}^{(K)}(0)$ by Eq.(3.55). The photon number resolution of our detection system is limited to $N = 4$, therefore we can only reconstruct a maximum of $S = 4$ arbitrary modes. In our reconstruction algorithm we assume that these four modes are completely unknown. So, with each experimental data set we perform mode reconstructions for all possible four-mode combinations of one Poissonian, four thermal and four single-photon modes. We then compare the minimized LS values and choose the mode combination and the set of reconstructed average energies per mode that result in the lowest LS value (details in appendix B.2). This way, our algorithm truly identifies the multimode light field with unknown modes, and not merely matches the previously-known modes with appropriate mean photon numbers. To test the robustness and reliability of our method, in our experiment we perform a series of acquisitions in several regimes, combining different modes and comparing the results of our mode-reconstruction technique (exploiting both $\theta^{(K)}$ and $g^{(K)}$ parameters) with the ones obtained using only the $g^{(K)}$'s (adding in both cases a further constraint on the overall no-click probability $Q(0^{\otimes N})$, to have a definite average number of photons of the light field) as in [38]. In particular, we especially focus on cases in which the multi-mode optical field under test features one or more single-photon modes, although heavily polluted by classical (thermal and/or Poissonian) light, giving an overall

$g^{(2)}(0) \geq 1$. The obtained results are summarized in Table 3.1, comparing the fidelity achieved by both reconstruction methods, defined as the distance $F_x = (2|\vec{m}_\mathrm{e} \cdot \vec{m}_x|)/(|\vec{m}_\mathrm{e}|^2 + |\vec{m}_x|^2)$, where $\vec{m}_\mathrm{e}$ is the set of expected mean photon numbers and $\vec{m}_x$ is the one reconstructed with the "x" method ($x = g+\theta$ labels the one exploiting both $g^{(K)}$ and $\theta^{(K)}$ functions, whilst $x = g$ indicates the one based solely on the $g^{(K)}$'s as in [38]). The expected mean photon number set $\vec{m}_\mathrm{e}$ is obtained by separately measuring the mean photon number per pulse of each mode composing the optical field to be reconstructed. Table 3.1 shows the number of modes present in the multimode light field under examination (S^e), as well as the number of modes identified by both reconstruction methods, respectively labeled $S^{\mathrm{rec}}_{g+\theta}$ and S^{rec}_{g} (for both of them, the number of correctly recognized modes is indicated in parentheses). For each case studied, the value of $g^{(2)}_{\mathrm{exp}}(0)$, the observable that is typically used for discriminating between classical and non-classical states, is also reported in the last column of Table 3.1.

These results demonstrate how the $g^{(K)}, \theta^{(K)}$ method manages to faithfully reconstruct the modal structure of the multimode light field characterized by our detector tree, always obtaining large fidelities (above 0.95) and identifying the correct number and type of optical modes for all the cases investigated. This gives the experimental proof of both the reliability and robustness of our method, that clearly outperforms the one relying solely on the $g^{(K)}$ parameters [38] in all the cases (except for case V where fidelities are comparable). The latter, in fact, not only achieves comparatively lower fidelities (occasionally going below 0.9, indicating poor reconstruction), but in half of the cases it does not correctly identify the number and types of optical modes comprising the multimode field under test, as it is evident from column (f) of Table 3.1.
The expected and reconstructed modal structures for the multi-mode fields marked with a star in Table 3.1, column (b), are shown in Figure 3.4. We show selected cases in which different single photon emitters are combined together (Figure 3.4a)) or mixed with strong Poissonian and/or thermal sources (Figure 3.4b)-f)). Each plot compares the mean-photon number of every mode present in the light field (yellow bars) with the reconstructed one obtained

Case	(a)S^{e}	(b)Mode configuration	Method $g+\theta$ (c)$F_{g+\theta}$	(d)$S^{\mathrm{rec}}_{g+\theta}$	Method g (e)F_g	(f)S^{rec}_g	(g)$g^{(2)}_{\mathrm{exp}}(0)$
I	4	1 SPS, 2 Th, 1 Poi	0.9597	4 (4)	0.9337	4 (4)	1.137 ± 0.002
II	4	1 SPS, 3 Th	0.9518	4 (4)	0.9480	4 (4)	1.332 ± 0.002
III	4	2 SPS, 1 Th, 1 Poi $\star$	0.9745	4 (4)	0.9469	4 (4)	1.044 ± 0.003
IV	4	2 SPS, 2 Th $\star$	0.9979	4 (4)	0.9949	4 (3)	1.411 ± 0.005
V	4	3 SPS, 1 Poi $\star$	0.9941	4 (4)	0.9963	4 (4)	0.998 ± 0.003
VI	4	3 SPS, 1 Th $\star$	0.9996	4 (4)	0.9729	3 (3)	1.532 ± 0.012
VII	4	3 Th, 1 Poi	0.9819	4 (4)	0.7325	4 (3)	1.103 ± 0.001
VIII	4	4 Th	0.9547	4 (4)	0.8481	4 (3)	1.245 ± 0.001
IX	3	1 SPS, 1 Th, 1 Poi	0.9885	3 (3)	0.9755	4 (3)	1.072 ± 0.002
X	3	1 SPS, 2 Th	0.9934	3 (3)	0.9390	3 (3)	1.478 ± 0.003
XI	3	2 SPS, 1 Poi $\star$	0.9931	3 (3)	0.8463	4 (3)	0.996 ± 0.004
XII	3	2 SPS, 1 Th	0.9972	3 (3)	0.8325	3 (2)	1.732 ± 0.011
XIII	3	2 Th, 1 Poi	0.9749	3 (3)	0.9749	4 (3)	1.135 ± 0.001
XIV	3	3 SPS $\star$	0.9947	3 (3)	0.9660	4 (3)	0.64 ± 0.03
XV	3	3 Th	0.9509	3 (3)	0.9490	3 (3)	1.349 ± 0.001

Table 3.1: Performance comparison between the $g+\theta$ and the g methods. Columns (a) and (b) show, respectively, the number S^{e} of modes and the mode types of the multimode light field to be reconstructed. Column (c) shows the fidelity $F_{g+\theta}$ between the expected multimode optical field and the one reconstructed exploiting both $g^{(K)}$'s and $\theta^{(K)}$'s, while column (d) indicates the number of optical modes $S^{\mathrm{rec}}_{g+\theta}$ identified (correctly identified) by this technique. Columns (e) and (f) are equivalent of columns (c) and (d), respectively, but for the reconstruction method that uses $g^{(K)}$'s only. Finally, column (g) shows the $g^{(2)}_{\mathrm{exp}}(0)$ value experimentally measured for each mode configuration. The reconstructed mean photon number per mode for starred configurations are shown in Fig. 3.4, together with their theoretically-expected counterparts. SPS: single photon state; Th: thermal mode; Poi: Poissonian mode.

with our novel technique (dark blue bars) and with the reconstruction method exploiting only the $g^{(K)}$'s (light blue bars).

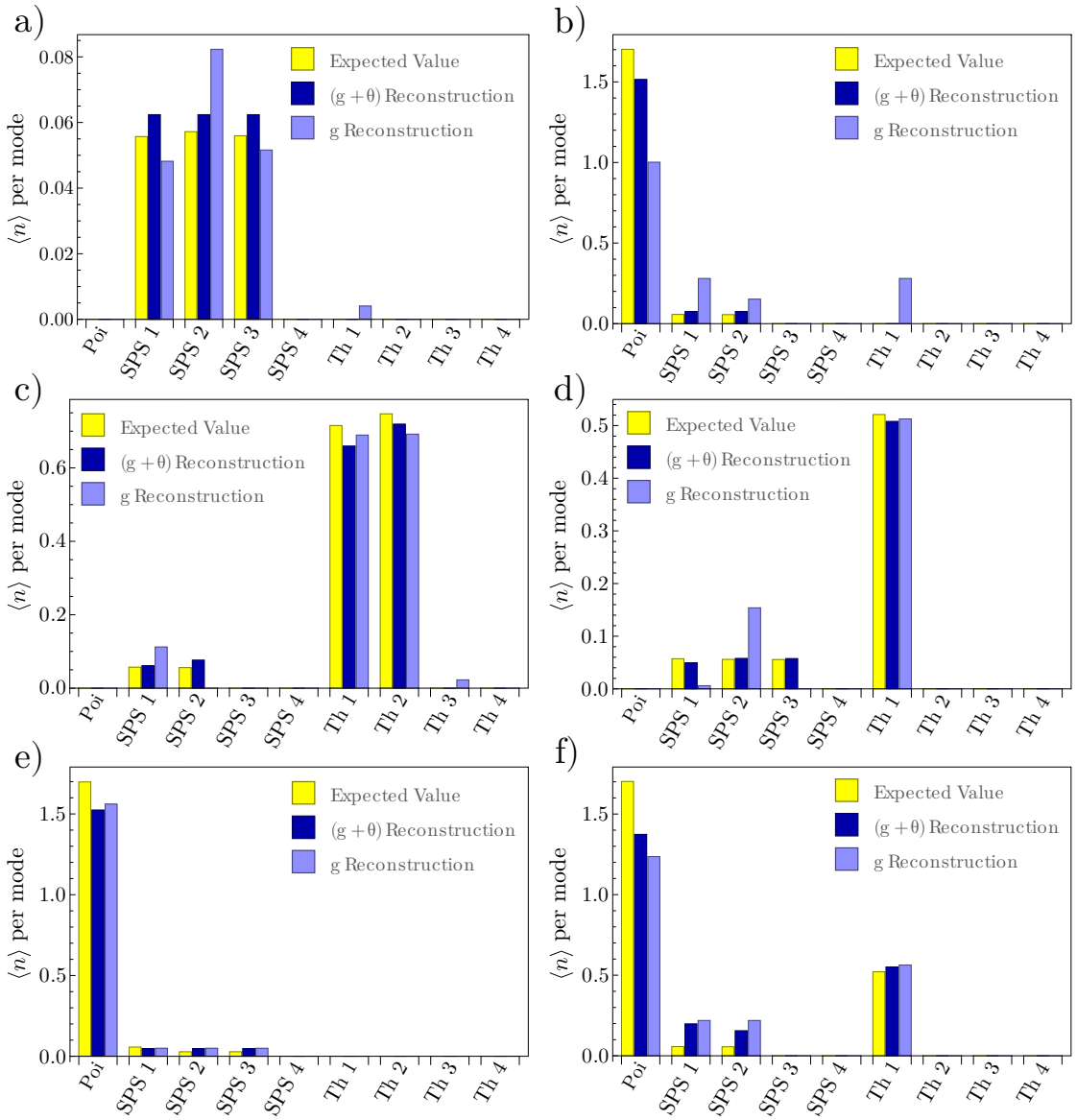

Figure 3.4: Mode structure reconstruction results. Expected and reconstructed mean photon number per mode for the light fields generated by: a) three single-photon emitters; b) two single-photon emitters in the presence of Poissonian light; c) two single-photon emitters together with two thermal fields; d) three single-photon emitters in the presence of a thermal field; e) three single-photon emitters in the presence of a Poissonian field; f) two single-photon emitters with both a Poissonian and a thermal mode. Yellow bars correspond to the mean photon numbers per mode present in our light field, whilst dark and light blue bars represent, respectively, the ones obtained with the $g^{(K)} + \theta^{(K)}$ and $g^{(K)}$-only reconstruction techniques. Poi: Poissonian mode. SPS: single photon state. Th: thermal mode.

In particular, Figure 3.4 shows the following cases: a) three single-photon emitters; b) two single-photon emitters in presence of heavy Poissonian noise; c) two single-photon emitters in presence of two thermal sources; d) three single-photon emitters in presence of thermal noise; e) three single-photon emitters in presence of heavy Poissonian noise; f) two single-photon emitters mixed with both a Poissonian and a thermal mode. Even though the Poissonian and thermal mode intensities are, respectively, about 30 and 10 times higher than that of each single-photon emitter, our technique correctly recognizes and reconstructs the type and number of light modes composing our optical field, identifying non-classical single-photon emission even in supposedly classical optical fields, i.e. with $g^{(2)}_{\mathrm{exp}}(0) \geq 1$, and not finding single-photon emission in multimode fields with no single-photon mode.

3.3.3 Experimental setup

In our experimental setup, shown in Figure 3.5, a pulsed telecom laser (1.55 μm) attenuated to the single-photon level generates a Poissonian mode. Each pseudo-thermal mode is produced by making the same laser pass through a rotating ground glass disk. Finally, heralded single-photon states at 1.55 μm are obtained from a heralded single-photon source based on spontaneous parametric down-conversion (SPDC). A continuous wave (CW) laser (at 532 nm) pumps a periodically-poled lithium niobate (PPLN) crystal, generating photon pairs at 810 nm (idler) and 1.55 μm (signal) [56, 57]. The idler photon is spectrally filtered and coupled to a single-mode fiber (SMF) connected to a Si-SPAD, heralding the presence of the corresponding signal photon. The generated state is close to a single-photon Fock state, with $g^{(2)}(0) < 0.05$. Once these modes are incoherently combined, the resulting multi-mode field is sent to our detector tree, allowing for a photon-number resolution up to $N = 4$ photons. With our scheme, we can generate S-mode optical fields (with $S = 1, ..., N$) whose underlying mode structure can comprise up to S thermal and/or single-photon modes, and up to one Poissonian mode, giving rise to $(2S + 1)$ possible different modal configurations. As stated above, in our particular case we consider a maximum of $N = 4$ modes combined

together.

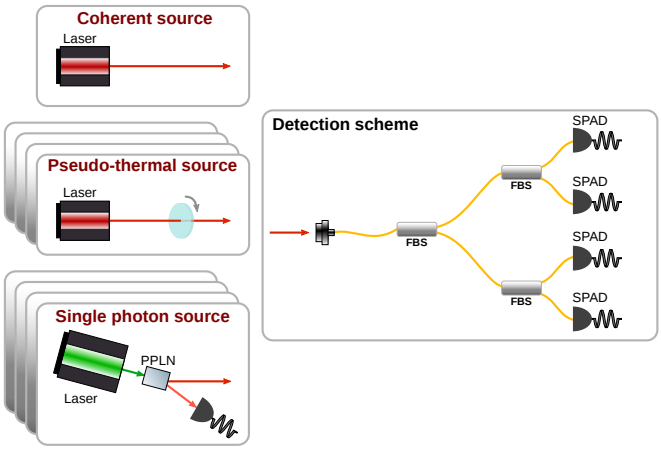

Figure 3.5: Experimental setup.The physical systems under study are a classical or non-classical multimode fields. The non-classical ones correspond to the emission of $M \leq N$ single-photon sources, heavily affected by thermal and/or Poissonian noise, optically coupled to a detector tree able to discriminate up to $N = 4$ incoming photons. The classical fields, instead, are arbitrary compositions of multi-thermal and Poissonian modes. On the left, three types of sources generate photons at 1.55 μm: a coherent (Poissonian) mode, produced by attenuating a pulsed laser; pseudo-thermal mode(s), generated by the pulsed laser sent to a rotating ground glass disk; single-photon mode(s) are emitted by a heralded single-photon source based on SPDC in a PPLN crystal. On the right, a pictorial scheme of our detector tree, which consists of a cascade of three 50:50 fiber beam splitters (FBSs) in a tree configuration connected to four InGaAs/InP SPADs.

3.3.4 Results discussion

Overall, our technique exploiting both $g^{(K)}$ and $\theta^{(K)}$ enables a reliable reconstruction of the mode structure of very complex multimode fields, with simultaneous presence of Poissonian, thermal and/or single-photon emission, even in cases that are not successfully reconstructed with the method exploiting $g^{(K)}$ parameters only. This is particularly interesting, since it is a well known issue that, when sampling g-function only, it is practically impossible to distinguish the emission of a SPS in the presence of noise from the simultaneous emission of two distinct and differently coupled SPSs. The studied cases demonstrate that the proposed technique is extremely efficient for characterizing SPSs in noisy environments, with practical applications to nonclassical emission from fluorescent targets. The applications range from

characterization of color centers in diamond [43, 44, 45, 46, 47, 48, 49, 50], which can be affected (or even overtaken) by both Poissonian (residual excitation laser light) and thermal (stray light, unwanted fluorescence) noise contributions, to nonclassical imaging with fluorophores. According to our results, the proposed technique for the mode reconstruction of optical fields, based on the combination of $g^{(K)}$ and $\theta^{(K)}$, not only outperforms the one illustrated in [38], but it is also capable to reconstruct more complex mode structures that could not be processed with the legacy method, ultimately proving that adding $\theta^{(K)}$ parameters estimation in the mode reconstruction algorithm leads to superior performance. Finally, the fact that this new technique does not rely on any "a priori" assumption on the number and type of modes constituting the optical field (except for the obvious constraint on the maximum number of modes allowed, due to the finite photon number resolution of the PNR detector used) not only is a clear evidence of its robustness, but also allows for its widespread application to several practical scenarios in quantum metrology and other quantum technologies.

Chapter 4

NV^- center as a sensor

4.1 Optically detected magnetic resonance (ODMR) technique: theory

In this section the spin properties of the negative charge state of the nitrogen-vacancy (NV^-) center are analyzed in detail. As mentioned in section 1.2.2, its ground state is in a spin triplet configuration (S=1). Due to that state configuration, the energy levels assume different energies values depending on the electromagnetic fields, the temperature and the reticular mechanical stresses. By measuring the energy difference between the ground state levels characterized by the different third spin component (m_s), it is possible to estimate the electromagnetic fields and/or thermal variations. The method that allows to evaluate the levels resonance frequency (i.e. their energetic difference) is the optically detected magnetic resonance (ODMR) technique.

In the next sections the standard ODMR technique and a new ODMR variant for a faster measurement are described.
Afterwards, we will put this in the contest of the ground state Hamiltonian and we will discuss the dependence of the energy levels on the magnetic and electric fields and finally on the temperature and consequently we will show their effects on the ODMR spectrum.

4.1.1 Continuous ODMR technique

One of the characteristics that makes NV^- centers so attractive and convenient as key element in various type of sensors is the possibility to discriminate the spin components of the electronic state. This is allowed by the different coupling of the $|m_s = 0\rangle$ state with a metastable level, compared to the $|m_s = \pm 1\rangle$ states and results in a variation of the photoluminescence (PL) of the defect under laser non resonant excitation, (see section 1.2.1). The ODMR technique consists in the application of a microwave field (MW) on the sample, simultaneously with its exposure to a non resonant laser at a frequency higher than the resonant one, corresponding to the energy gap between the ground state and the excited ^{3}E level (e.g., 532 nm) (see Figure 4.1a). When the MW frequency reaches the ground state resonance, with a certain probability (depending on the MW power), those NV centers will be initialized in the states $|m_s = \pm 1\rangle$ rather than $|m_s = 0\rangle$. As mentioned, this corresponds to a reduction in photoluminescence of the NV centers, as it can be observed, e.g., in Figure 4.1b, where a typical ODMR spectrum is reported.

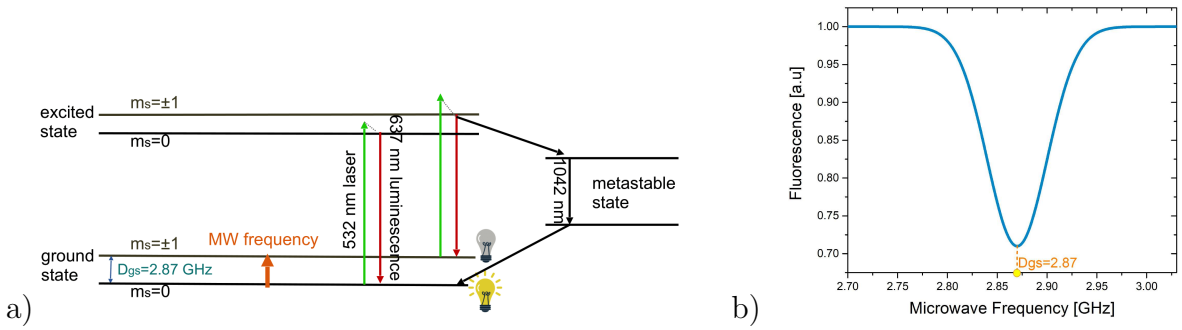

Figure 4.1: a) NV− state transition that occurs after laser excitation and MW excitation. The coupling of the states $|m_s = \pm 1\rangle$; with the metastable level generates a statistically lower PL emission than the $|m_s = 0\rangle$. b) The profile of the ODMR spectrum as a function of the frequency f can be expressed with the following function: $F(f) = R \cdot [1 - C \cdot func(\frac{f - f_0}{FWHM})]$. Where F is the fluorescence collected by the sample, R is the emission rate of the incident photons, C is the contrast (i.e. the difference in the emission rate between the state $|m_s = 0\rangle$ and the states $|m_s = \pm 1\rangle$, i.e. at the resonant frequency), *func* is the function that fits better to the profile of the *minimum* (*Lorentzian curve*), $FWHM$ is the width of the peak, and f_0 is the resonant frequency (D_{gs} in absent of external fields).

Consequently, as will be described in the following sections, a variation of the measurement of the MW resonance frequency ΔD_{gs}, allows to obtain an estimate, for example, of the temperature variation:

$$\Delta T = \frac{\Delta D_{gs}}{\partial D_{gs}/\partial T} \tag{4.1}$$

In the same way it is possible to obtain magnetic and electric fields variations, substituting the appropriate coupling coefficients as will be described in the following sections.

It is important to underline that a standard method to derive the frequency at the minimum of the dip of the ODMR graph consists, for example, by interpolating the data with a Lorentzian function. By integrating the ODMR measurement for an increasingly longer time, the estimation of the resonant frequency is improved. However, this method may require too long measurement times for certain applications. In the next sections some ODMR methods are described to improve the sensitivity of the measurement.

4.1.2 Differential ODMR technique

By repeatedly acquiring the ODMR spectrum, it is possible to evaluate the temperature variation ΔT that may have occurred in two distinct instants of time, see Equation 4.1. This is typically realized by a frequency shift measurement of the ODMR fluorescence dip.
When a fast measurement is needed, such as when the target is a biological sample, in order to preserve the cells health and its biological processes, it is necessary to expose the target to lasers and microwaves as quickly as possible. To estimate the resonant frequency shift ΔD_{gs} more conveniently than the traditional method, the following experimental procedure could be adopted. The full ODMR spectrum is acquired only once. The data is post-processed creating the differential spectrum (see Figure 4.2).

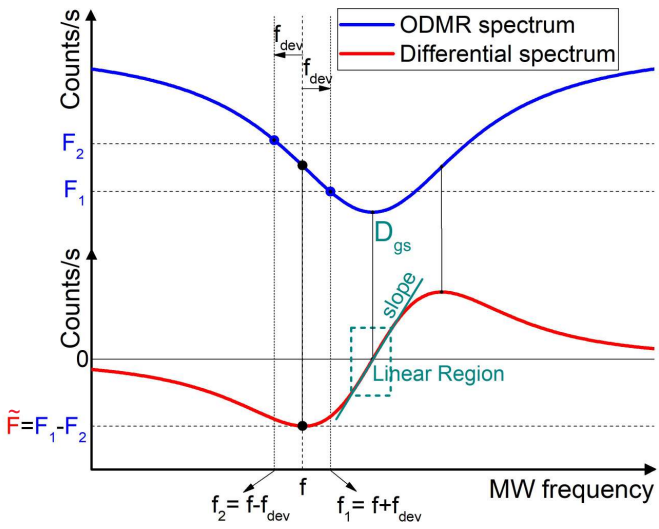

Figure 4.2: Sketch of differential measurement. From the ODMR spectrum (upper part of the figure) the differential spectrum (lower part of the figure) is derived taking, for every value of the microwave (MW) frequency, the difference in fluorescence $\tilde{F}$ between two point separated by $2f_{dev}$. $\tilde{F}$ is zero at the two extreme of the spectrum and at the resonant frequency D_{gs}. Around D_{gs} there is a region where $\Delta\tilde{F}$ depends linearly on ΔD_{gs} trough the differential spectrum *slope*.

Where in correspondence to each microwave scanning frequency f, a differential fluorescence value $\tilde{F}$ is associated, evaluated as follows: $\tilde{F} = F(f + f_{dev}) - F(f - f_{dev})$. F represents the fluorescence collected by the sensor and f_{dev} represents a frequency deviation chosen in order to optimize the differential graph. (For the measurements carried out in the biological field with our diamond samples and in our experimental conditions $f_{dev} = 2$ MHz).
This method is advantageous since temperature variations are estimated by the differential signal $\tilde{F}$ that is now linear with respect to frequency shift, around the resonant frequency D_{gs}:

$$\Delta\tilde{F} = slope \cdot \Delta D_{gs} \tag{4.2}$$

rather than finding a minimum that is more difficul to estimate (see Figure 4.2).
The *slope* is obtained through a linear regression from the differential spectrum.
The differential signal $\tilde{F}$ is acquired at a single frequency chosen in the linear region of the differential spectrum. Any variation $\Delta\tilde{F}$ recorded will be

attributable to a shift in the resonance frequency ΔD_{gs} (see Eq.(4.2)) and therefore, for example, an eventual temperature variation ΔT (see Eq. 4.1) will be stimated, according to:

$$\Delta T = \frac{\Delta D_{gs}}{\partial D_{gs}/\partial T} = \frac{\Delta \tilde{F}/slope}{\partial D_{gs}/\partial T} \tag{4.3}$$

4.1.3 Lock-in technique

Another experimental strategy to obtain an estimate of the resonant frequency shift ΔD_{gs} in a short measurement time is to use the lock-in detection technique. The principle is similar to the one adopted for the differential ODMR technique: measure the fluorescence F emitted by the NV center at a single microwave frequency, instead of recreating the entire ODMR spectrum by performing a frequency scan. As in the previous section, in this way a reading of a fluorescence variation ($\tilde{F}$) can be directly associated with the variation of external fields, provided that the dependence (the one that was the *slope* in the previous method) has been obtained from the complete differential graph.
In addition, a further advantage of the lock-in technique is to "move" the measured signal to a frequency region affected by less noise providing the possibility to detect small signal amplitudes even in the presence of strong noise.
The working principle of a lock-in amplifier (LIA) can be explained by considering a single ODMR dip with Lorentzian lineshape of linewidth $FWHM$, contrast C and frequency f_0 (Fig. 4.1b). The detected fluorescence can be written as:

$$F(f) = R \cdot [1 - C \cdot \frac{1}{1 + (\frac{f - f_0}{FWHM/2})^2}] \tag{4.4}$$

where R is the fluorescence in the absence of MW. Consider a sinusoidal MW input signal, $f_{MW}(t) = f_c + f_{dev} \cdot sin(2\pi f_{mod} t)$, where f_{mod} is the modulation frequency, f_c is the central frequency and f_{dev} is the frequency deviation. Suppose that we also have available a reference signal $V^{ref}(t) = V_0^{ref} \cdot sin(2\pi f_{mod} t)$ at the same modulation frequency (Figure 4.3). After integration over the period T all oscillating components vanished and only DC

output in form of dispersion-type signal with a zero-crossing at f_0 remains:

$$V_{LIA}(f, f_{dev}) \propto \frac{F(f+f_{dev}) - F(f-f_{dev})}{2} = \frac{V_0 C}{2} \cdot [\frac{1}{1+(\frac{(f+f_{dev})-f_0}{FWHC/2})^2} + \frac{1}{1+(\frac{(f-f_{dev})-f_0}{FWHC/2})^2}] \tag{4.5}$$

V_0 is a voltage determined by R and the output settings of the LIA (Figure 4.3a)). Setting $f_{dev} = \frac{FWHM}{2\sqrt{3}}$ maximizes the amplitude of the LIA signal and consequently the signal-to-noise ratio of the measured signal. A time-varying field, for example an eventual temperature variation ΔT (see Eq. 4.1), is sensed by setting $f_c = f_0$ and detecting resonance frequency shifts $f_0(t) = f_0 + \delta f(t)$, where $\delta f(t) = \partial D_{gs}/\partial T \cdot \Delta T(t)$ as:

$$V_{LIA}(t) \simeq \frac{-3\sqrt{3}}{4} \cdot \frac{V_0 C}{FWHM} \cdot \partial D_{gs}/\partial T \cdot \Delta T(t) \tag{4.6}$$

The demodulated signal is linear in the temperature variation and therefore provides a good measure for $\Delta T(t)$. Lock-in detection is ideal for very noisy signals and allows one to achieve optimally driving a low-density ensemble, maintaining a linewidth that closely resembles those obtained from single NV defects. The reason why it is sometimes preferable to use the differential ODMR is related to its simpler application. In fact, creating the lock-in signal requires a more advanced instrumentation (see Figure 4.3b)).

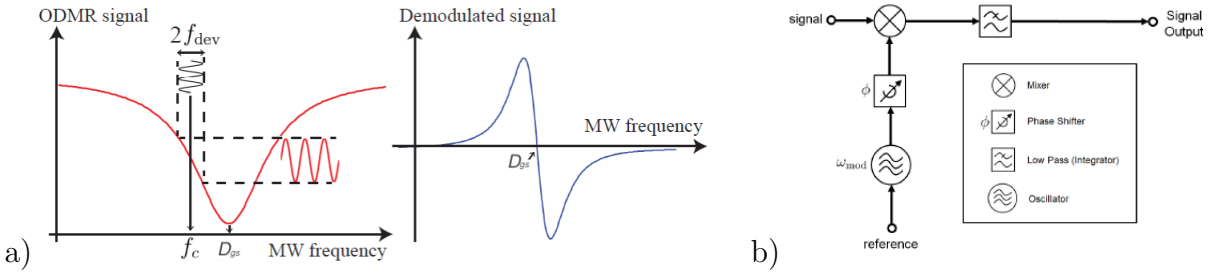

Figure 4.3: a) Optically detected magnetic resonance signal. The MW frequency is modulated at the frequency f_{mod} around the central value f_c with a certain frequency deviation f_{dev}. Right: The demodulated signal has a dispersive lineshape when sweeping the central frequency. b) Block diagram of a lock-in amplifier.

4.2 NV^- sensor property

In this section the electronic state spin property of the NV^- is described highlighting its dependence with respect to external fields and temperature variation.

4.2.1 NV^- ground electronic state

The Hamiltonian of $^3A_2$, the ground spin state of the NV system, can be written in the following form [58, 59]:

$$\frac{\hat{H}_{gs}}{h} = \hat{S}\mathbf{D}\hat{S} + \hat{S}\mathbf{A}\hat{I} + \hat{I}\mathbf{Q}\hat{I} \tag{4.7}$$

where $\hat{S} = (\hat{S}_x, \hat{S}_y, \hat{S}_z)$ and $\hat{I} = (\hat{I}_x, \hat{I}_y, \hat{I}_z)$ are the dimensionless electron and nitrogen nuclear spin operators, respectively. The first term represents the fine structure splitting due to the electronic spin-spin interaction, coupled by the fine structure tensor $\mathbf{D}$. The second term is generated by the hyperfine interaction between NV electrons and the nitrogen nucleus ($I = 1$ for a ^{14}N nucleus, while $I = 1/2$ for a ^{15}N nucleus), with the hyperfine tensor $\mathbf{A}$. Finally, the third term represents the nuclear electric quadrupole interaction, with the electric quadrupole tensor $\mathbf{Q}$. It should be noted that, in this notation, the component z coincides with the NV axis of symmetry. Due to the symmetry of the NV center, $\mathbf{D}$, $\mathbf{A}$, and $\mathbf{Q}$ are diagonal in the NV coordinate system [60, 61] and, in terms of the natural spin-triplet basis $\{|m_s = 0>, |m_s = +1>, |m_s = -1>\}$, the Hamiltonian can be written as:

$$\frac{\hat{H}_{gs}}{h} = \underbrace{D_{gs}[\hat{S}_z^2 - \hat{S}^2/3]}_{electronic\ spin-spin\ interaction} + \underbrace{A_{gs}^{//}\hat{S}_z\hat{I}_z + A_{gs}^{\perp}[\hat{S}_x\hat{I}_x + \hat{S}_y\hat{I}_y]}_{electron-nucleus\ spin\ interaction} + \underbrace{Q_{gs}[\hat{I}_z^2 - \hat{I}^2/3]}_{nuclear\ spin-spin\ interaction} \tag{4.8}$$

where $D_{gs} \simeq 2.87$ GHz is the zero field splitting, Q_{gs} is the nuclear electric quadrupole parameter, $A_{gs}^{//}$ and $A_{gs}^{\perp}$ are the axial and non-axial magnetic hyperfine parameters [62, 63]. The parameters values are reported in Table 4.1.

Hyperfine parameters	Value
Zero field splitting	$D_{gs} \simeq 2.87$ GHz
Axial hyperfine term	$A^{//}_{gs,^{14}N} \simeq$ -2.14 MHz
	$A^{//}_{gs,^{15}N} \simeq 3.03$ MHz
Transverse hyperfine term	$A^{\perp}_{gs,^{14}N} \simeq$ -2.70 MHz
	$A^{\perp}_{gs,^{15}N} \simeq 3.65$ MHz
Nuclear electric quadrupole term	$Q_{gs} \simeq$ -5 MHz

Table 4.1: Hyperfine parameters for the NV defect determined at room temperature.

4.2.2 Magnetic field sensing

A static magnetic field produces the well-known Zeeman effect [64], that it is described by:

$$\frac{\hat{V}_{gs}}{h} = \underbrace{\frac{\mu_B g^{//}_{gs}}{h}\hat{S}_z B_z + \frac{\mu_B g^{\perp}_{gs}}{h}(\hat{S}_x B_x + \hat{S}_y B_y)}_{Zeeman\ interaction} + \underbrace{\frac{\mu_N g_N}{h}\hat{I}\vec{\boldsymbol{B}}}_{nuclear\ Zeeman\ interaction} \tag{4.9}$$

where μ_B is the Bohr magneton, μ_N is the nuclear magneton, $g^{//}_{gs}$ and $g^{\perp}_{gs}$ are the components of the ground state electronic g-factor tensor and g_N is the isotropic nuclear g-factor. In the presence of relatively weak magnetic fields, it is possible to approximate the almost diagonal g-factor tensor in a diagonal form, with constant $g_e = 2.003$ [65]. As reported in Table 4.2, the interaction of the magnetic field with the nucleus is 2000 times smaller and, consequently, it is typically neglected [66]. The presence of external fields eliminates the energy degeneracy of the levels $|m_s = \pm 1>$, whose splitting become $\gamma_e B_z$, where $\gamma_e = \frac{\mu_B g_e}{h}$ (see Figure 4.4). If, instead of a single NV center, an ensemble of NV centers is considered, up to eight magnetic resonance dips can be observed, due to the four possible orientation of the NV axis in the diamond's crystalline matrix (see Figure 4.5). For certain directions of the magnetic field, some resonances can be degenerate.
A NV-based magnetometer can be realized, for example, by applying a bias field along the NV axis, removing the degeneracy, so that changes in the magnetic field projection along this axis affect the resonance frequencies almost linearly. Another option is to use all four NV alignments; although the eight ODMR frequencies have more complicated dependence on $\vec{B}$, this

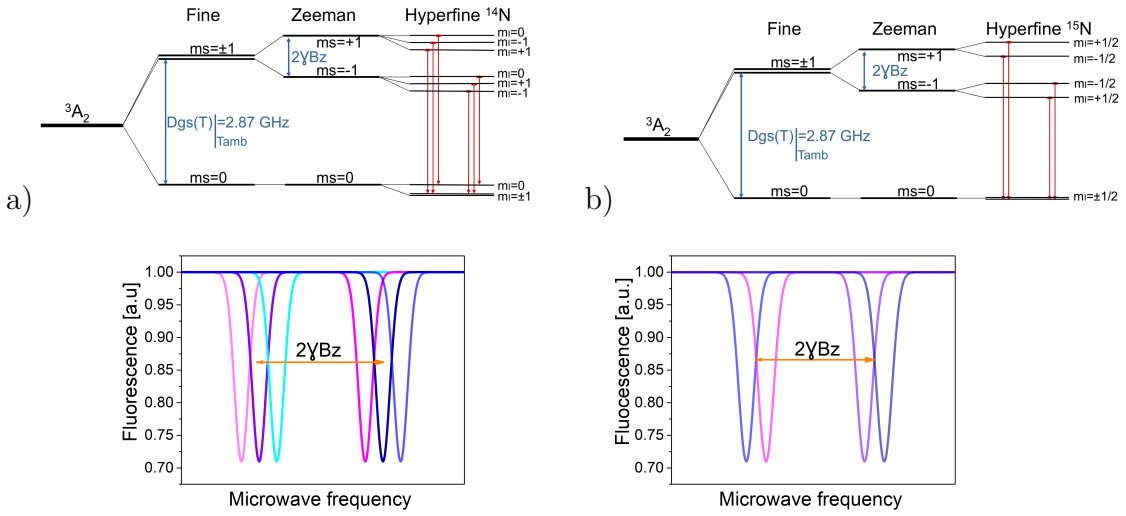

Figure 4.4: NV ground-state $^3A_2$ scheme. Above: a) ^{14}N hyperfine states and b)^{15}N hyperfine states. Below: schematic ODMR spectra. The spectra are shown considering Zeeman splitting and hyperfine splitting.

option yields information about the direction of magnetic field [67].
Because of this interesting properties connected to the presence of a magnetic field, the use of NV center as a magnetic field sensor firstly was proposed in [68, 69] and demonstrated with single NV [64, 70] and NV ensembles [71] in 2008.

4.2.3 Electric field sensing

The Hamiltonian describing the interaction with the electric field was derived from molecular orbit theory by Doherty et al.[59] and it can be written in the following form:

$$\frac{\hat{V}_{gs}}{h} = d_{gs}^{//}(E_z+F_z)[\hat{S}_z^2-\frac{\hat{S}^2}{3}]+d_{gs}^{\perp}(E_x+F_x)(\hat{S}_y^2-\hat{S}_x^2)+d_{gs}^{\perp}(E_y+F_y)(\hat{S}_x\hat{S}_y+\hat{S}_y\hat{S}_x) \tag{4.10}$$

where $d_{gs}^{//}$ and $d_{gs}^{\perp}$ are respectively the axial and non-axial Stark shift components of the permanent electric dipole moment $d_{gs}^{\perp}$ in the ground triplet state [73], $\vec{\boldsymbol{E}}$ is the electric field and $\vec{\boldsymbol{F}}$ is the mechanical strain.
According to Eq.(4.10) the effect of the electric field $\vec{\boldsymbol{E}}$ plays the same role as mechanical strain $\vec{\boldsymbol{F}}$ [74, 75]. The strain depends on the diamond material:

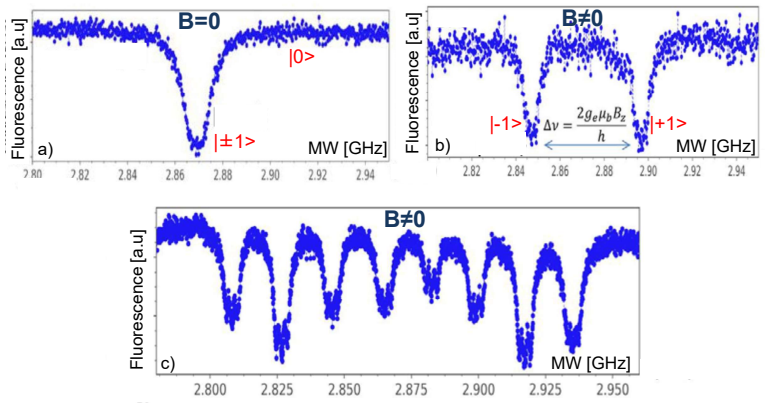

Figure 4.5: ODMR spectra in the absence a) and in the presence b) of an external bias magnetic field. The magnetic field lifts the degeneracy of the $|m_s = \pm 1>$ states and results in two separate dips in the ODMR spectrum. c) An example ODMR spectrum (excited at 532 nm) with a magnetic field in an arbitrary direction for an ensemble NV centers in diamond. Each of the four NV alignments has a different magnetic field projection along its quantization axis, leading to eight ODMR peaks (two for each NV alignment). For each dip a coupling with the nuclear spin of the ^{14}N atom generates additional three hyperfine levels [72].

in single-crystal samples, the mechanical strain field is substantially negligible; while, in polycrystalline ones, a relatively high strain field is induced by the growth conditions, leading to a splitting of the spin state $|m_s = \pm 1>$ even in absence of external fields.
The frequency shift caused by the electric field is much smaller than the shift produced by the presence of a magnetic field (see Table 4.2). For this reason, in order to reliably measure this second-order effect caused by the Stark shift, it is necessary to decouple it from the Zeeman shift.

Briefly, the fine structure Hamiltonian of the NV ground state, describing the energy levels of the electronic spin states due to the spin ($\hat{S}$) interaction with the static magnetic ($\vec{\mathbf{B}}$), electric ($\vec{\mathbf{E}}$), and strain ($\vec{\mathbf{F}}$) fields, can be written in terms of the natural spin-triplet basis $\{|m_s = 0>, |m_s = +1>, |m_s =$

$-1>\}$ in the following matrix form:

$$\hat{H}_{gs} = \begin{pmatrix} 0 & -\mu_B g_e \frac{B_x - iB_y}{\sqrt{2}} & -\mu_B g_e \frac{B_x + iB_y}{\sqrt{2}} \\ -\mu_B g_e \frac{B_x + iB_y}{\sqrt{2}} & hD + \mu_B g_e B_z & -hd_{gs}^{\perp}(P_x - iP_y) \\ -\mu_B g_e \frac{B_x - iB_y}{\sqrt{2}} & -hd_{gs}^{\perp}(P_x + iP_y) & hD - \mu_B g_e B_z \end{pmatrix}$$

where it is possible to observe that the natural-spin basis vectors are eigenstates of the Hamiltonian only in the presence of both the magnetic and electric field aligned with the NV axis. In this condition, $D = D_{gs} + d_{gs}^{//} P_z$ describes the frequency shift of the resonance lines resulting from the zero-field splitting and from the Stark effect associated with the component of the vector $\vec{\boldsymbol{P}} = \vec{\boldsymbol{E}} + \vec{\boldsymbol{F}}$. Otherwise, external fields not aligned to NV symmetry axis produce a non-diagonal matrix, and therefore energy levels of undefined spin. In particular, the presence of additional transverse strain and electric-field components $P^{\perp}$ modifies the ground-state structure.

The Hamiltonian assumes a quasidiagonal form considering a new spin basis $\{|0>, |+>, |->\}$, obtained by a field-dependent mixing of the $|m_s = +1>$ and $|m_s = -1>$ spin states according to the following unitary operator:

$$\hat{U} = \begin{pmatrix} 1 & 0 & 0 \\ 0 & e^{i\frac{\phi}{2}} sin(\frac{\theta}{2}) & e^{-i\frac{\phi}{2}} sin(\frac{\theta}{2}) \\ 0 & e^{i\frac{\phi}{2}} cos(\frac{\theta}{2}) & -e^{-i\frac{\phi}{2}} sin(\frac{\theta}{2}) \end{pmatrix}$$

where $\tan(\phi) = P_x/P_y$ and $\tan(\theta) = (d_{gs}^{\perp} P^{\perp})/(\mu_B g_e B_z)$ are the field-dependent phases defining the spin state mixing. The Hamiltonian takes the following form in the $\{|0>,|+>,|->\}$ basis:

$$\hat{H'}_{gs} = \hat{U}\hat{H}_{gs}\hat{U}^{\dagger} = \begin{pmatrix} 0 & c_1 \mu_B g_e B^{\perp} & c_2 \mu_B g_e B^{\perp} \\ c_1^* \mu_B g_e B^{\perp} & hD + W & 0 \\ c_2^* \mu_B g_e B^{\perp} & 0 & hD - W \end{pmatrix}$$

with

$$W = \sqrt{(hd_{gs}^{\perp} P^{\perp})^2 + (\mu_B g_e B_z)^2} \tag{4.11}$$

The complex constants c_1 and c_2 represent the phase of the matrix elements and $B^{\perp}$ is the transverse component of the magnetic field with respect to the NV axis. If $B^{\perp} \approx 0$, the non-diagonal terms can be neglected and the

Hamiltonian can be regarded as diagonal in the basis $\{|0>, |+>, |->\}$. The energy difference between the $|0>$ and the $|\pm>$ states is $hD \pm W$, corresponding to ODMR resonances separated by 2W/h depending on the strengths of the magnetic, electric, and strain fields, as well as their orientations with respect to the axes of the NV center. Since the states $|\pm>$ are a coherent superposition of the states $|m_s = \pm 1>$, we underline that the ODMR resonance is observed also in this case as a reduction in the fluorescence emission at the new MW resonance frequencies.

4.2.4 Temperature variation sensing

Another interesting feature of the NV complex is the temperature dependence of its spin levels [76]. Indeed, the microscopic origin of D_{gs}, also called the zero field splitting (ZFS) parameter, is due to spin-spin interactions in the NV's orbital structures, and the value depends on the lattice length, which is strongly correlated to the local temperature. When the local temperature increases the diamond lattice spacing of the NV center increases as well, lowering the spin-spin interaction and reducing the ZFS parameter D_{gs}. The resonant frequency between the two levels is:

$$D_{gs,T} = D_{gs,T_0} + \partial D_{gs}/\partial T \cdot \Delta T \tag{4.12}$$

The term D_{gs,T_0} represents the *spin-spin interaction* at room temperature T_0. The second term represents the effect of a temperature increase on the system. Under ambient conditions $D_{gs,T_0} \simeq 2.87\,GHz$ and the temperature dependence is $dD/dT \simeq -74kHz/K$ [76]. In general, the ZFS parameter shows a non-linear dependence, and its value increases when temperature decreases [77].

Property	Coupling coefficient
Magnetic field	$\gamma_e = \frac{\mu_B g_e}{h} \simeq 28$ GHz T^{-1}
	$\gamma_N = \frac{\mu_N g_N}{h} \simeq 15$ MHz T^{-1}
Electric field	$d_{//,gs} \simeq 3.5$ mHz V^{-1}m
	$d_{\perp,gs} \simeq 0.17$ Hz V^{-1}m
Temperature	$\partial D_{gs}/\partial T \simeq$ -74 kHz K^{-1}

Table 4.2: Coupling coefficient of the NV center with the external fields and temperature.

To realize a NV-based temperature sensor, the most obvious solution is exploiting the D_{gs} temperature dependence. This requires that no external field is present ($\vec{\boldsymbol{B}}, \vec{\boldsymbol{E}}, \vec{\boldsymbol{F}} = 0$), i.e. $|m_s = \pm 1>$ is degenerate. In this case, an increase in temperature leads to a decrease in the resonance frequency, associated with a shift of the degenerate levels $|m_s = \pm 1>$ towards the level $|m_s = 0>$.
Nevertheless, this is the simplest but not the optimal solution, since, even in the absence of applied fields, the sample may have an internal strain (especially when nanodiamonds are used instead of bulk diamond) and may be affected by the Earth's magnetic field. Unless it is possible to find a bulk diamond sample with negligible $\vec{\boldsymbol{F}}$ and to design an experimental set up able to reasonably compensate for the external magnetic field (e.g. Helmholtz coils), the dips would not be perfectly overlapped because of the non perfect degeneracy of $|m_s = \pm 1>$, thus showing a larger full-width-at-half-maximum (FWHM) and therefore a lower resolution.
A better solution is to apply an external magnetic field in order to significantly separate the spin levels, or in case of nanodiamonds, have samples with high internal mechanical stress. However in this configuration, a single dip can shift for a temperature variation, but also for a variation of magnetic field. To decouple the two contributions it is sufficient to monitor both $|m_s = +1>$ and $|m_s = -1>$ spin states at the same time, using simultaneous driving of the microwaves in ODMR technique [78]. As it can be seen in the Figure 4.6, by simultaneously monitoring the initial dips (red curves), it is in principle possible to understand if there are variations in the magnetic field (the dips move in opposite directions) or in temperature (the dips move in the same direction).

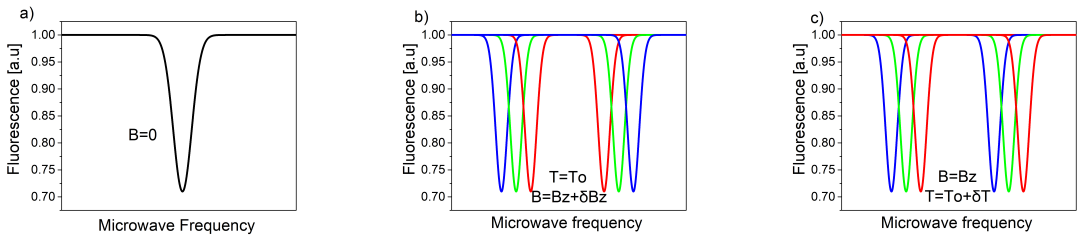

Figure 4.6: Example of magnetic and thermal shifts of the spin resonance, in ODMR spectra. Dips with equal colors correspond to paired resonances. The colors represent the timeline of the dips. The initial dips is red, then green and finally blue.

Chapter 5

Single photon confocal microscope with microwave control equipment for sensing measurements

5.1 Confocal microscope theory

This section analyzes the theoretical functioning of the confocal microscope, which is the essential tool for optically stimulating the diamond sample and collecting its photoluminescence.

5.1.1 Operating principles

Confocal microscopy in single photon luminescence is used to characterize the NV centers. With this technique it is possible to map luminescent physical systems, with a spatial resolution that is substantially limited by the excitation laser wavelength. The feature that best qualifies this technique is represented by the possibility of viewing the different optical planes of the sample, thanks to the presence of a collection iris, which has the function of eliminating the diffused light from the planes out of focus, (see Figure 5.1). The term "confocal" derives from the fact that there are 3 optically conjugated points of the system, that is: the laser source, the displayed object and the collection point of the emitted radiation. Hence, unlike conventional microscopy, where the image is formed directly on the detector, in confocal microscopy the probe radiation coming from the source illuminates the object only one point and therefore a scan of the laser beam or sample is required

to form the final image.

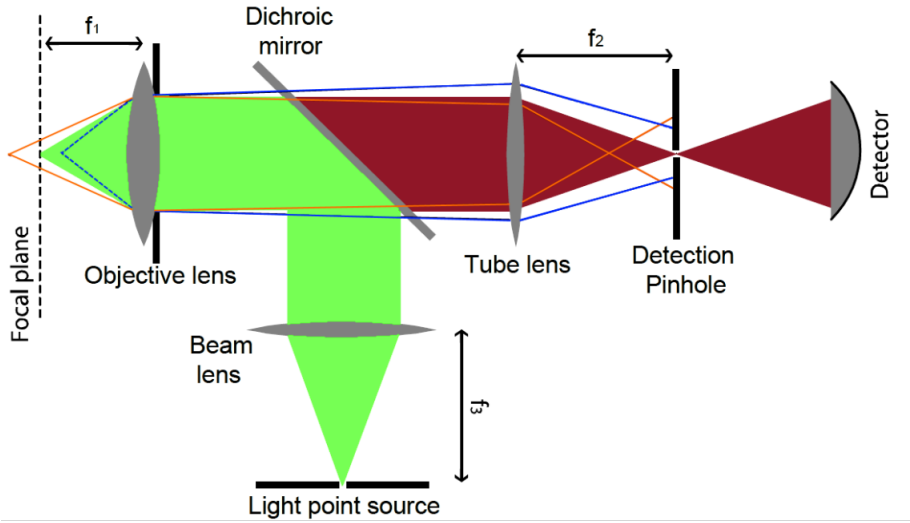

Figure 5.1: Confocal microscope setup. The rays of light arriving from objects lying at different depths with respect to the focal plane are intercepted by the collection iris (Pinhole).

As regards the study of the NV centers, the suitable source is a laser beam with a wavelength in the green ($\lambda = 532$ nm). To make the laser beam as similar as possible to an ideal plane wave, a lens is used, which focuses the beam at infinity. The light beam is reflected by a dichroic mirror (i.e. in our case a long-pass at 567 nm) and is then collected by a lens. The latter has the function of focusing the beam on a well-defined focal plane. The sample, which in turn contains one or more luminescent centers, is excited and isotropically emitting the luminescence radiation at different wavelengths, mainly in the red ($\lambda > 600$ nm) in the specific case of NV centers (see Figure 1.5). Part of the luminescence radiation is collected by the lens, arrives at the dichroic and, unlike the radiation of excitation, is transmitted and reaches the detector after passing through the collection iris. Without this latter optical component, the incoming light would be composed of photoluminescence generated by centers located at different depths, i.e. at different focal planes, making it difficult to isolate individual centers. This process is called *optical sectioning*, since geometrically removes the portion of fluorescence not coming from the focal plane.

5.1.2 Spatial resolution

Spatial resolution in optical microscopy is subject to the phenomena of *aberration* and *diffraction*: both limit the image quality. The first effect can ideally be removed by optimizing the optical alignment of the system. The second effect can only be minimized and represents the ultimate limit of the instrument's resolution.
To study the formation of an image mathematically, the *Point Spread Function* (PSF), is used. The PSF represents the impulse response in the field of image processing. In a generic microscope, the *I (x, y, z)* function describing the image is given by the convolution of the one representing the probed object *OBJ (x, y, z)* e of the PSF.

$$I(x, y, z) = OBJ(x, y, z) \otimes PSF(x, y, z) \tag{5.1}$$

A hypothetical object significantly smaller than resolution of the instrument (such as a single color center) can be approximated with a Dirac delta distribution:

$$OBJ(x, y, z) = \delta^3(x_0, y_0, z_0) \tag{5.2}$$

So the *I (x, y, z)* image resulting from an object of this type turns out to be the *PSF (x, y, z)* of the microscope itself.
The excitation radiation distribution near the object focal plane can be determined analytically (in paraxial approximation) by considering an incident plane electromagnetic wave that enters in the objective and is focused; this function is called I_p and, having cylindrical symmetry, can be expressed as:

$$I_p(\rho, \theta, z) = \frac{2 \cdot [J_1(\nu)]^2}{\nu^2} \quad with\ z = 0 \tag{5.3}$$

where:

$$\nu = \frac{2\pi}{\lambda} \cdot \rho \cdot n \cdot sen\ \alpha \tag{5.4}$$

In Eq.(5.3) the z axis coincides with the optical axis, ρ represents the distance from the optical axis, J_1 is the first order Bessel function, n is the refractive index of the medium (assumed to be homogeneous) between the target and

the sample, λ is the excitation wavelength and α is the half-opening of the light cone coming out of the lens. The equation (5.3) shows how the electromagnetic radiation, after being collected by the objective, is not entirely focused on one point of the sample but on a spatial region of finite size, called "*Airy disk*". This happens because the radiation is diffracted through the pupil of the objective itself.

The resolution η_{xy} on the xy plane can be defined as the inverse of the radius of the Airy disk R_{xy}, as follows:

$$R_{xy} = \frac{0.61 \cdot \lambda}{n \cdot sen\ \alpha} = \frac{0.61 \cdot \lambda}{N.A.} \tag{5.5}$$

This is defined as the FWHM of $I_p(\rho, \theta, z)$ at z = 0, having defined $N.A.$ such as the numerical aperture of the objective. Therefore:

$$\eta_{xy} = \frac{1}{R_{xy}} \tag{5.6}$$

To define the resolution η_z on the z axis it is necessary to impose $\rho = 0$ in Eq.(5.3), which becomes:

$$I_p(0, \theta, z) = [sen\ (\frac{u}{4}) \cdot \frac{4}{u}]^2 \tag{5.7}$$

with:

$$u = \frac{2\pi}{\lambda} \cdot z \cdot n \cdot sen^2\ \alpha \tag{5.8}$$

At this point R_z is defined as the distance (along z) between the maximum intensity and the nearest zero. You get:

$$R_z = \frac{2 \cdot n \cdot \lambda}{N.A.^2} \tag{5.9}$$

So the resolution along the optical z axis is given by:

$$\eta_z = \frac{1}{R_z} \tag{5.10}$$

It is therefore observed that both the axial and lateral resolution depend of the excitation radiation wavelength and the objective numerical aperture.

While the wavelength cannot be varied, since only photons of certain energies can efficiently stimulate the luminescent centers under examination, the numerical aperture does not affect the emission of the center. To maximize resolution is possibile act on this last quantity, for example by using oil immersion objectives, which allow you to improve the refractive index matching and therefore $N.A.$ (with respect to the objectives used in air).

5.1.3 Optical sectioning

The radiation emitted by the sample passes through the objective and is focused by the lens, before being collected by the detector.
The magnification of this system is given by the value $M = \frac{f_2}{f_1}$, where f_1 and f_2 are the focal distances of the objective and the lens, respectively. For geometric reasons, the light intensity distribution on the image focal plane is the same as that on the sample focal plane, that is I_p. However, the image is modified by the M scale factor in the directions transverse and axial. Now consider an optical plane uniformly illuminated. The luminous intensity profile is defined by the square of the PSF, therefore the energy collected is:

$$E_{traditional\ microscope} = \int PSF(x, y, z)^2\ dx\ dy \tag{5.11}$$

The integral is generally constant (along z) due to energy conservation, therefore at any distance the same energy is collected. Consequently, it is impossible to determine the position of the correct plane on the z axis. In the confocal microscope, however, the iris blocks all the radiation coming from planes out of focus, preventing it from reaching the detector. In this case the energy collected is:

$$E_{confocal\ microscope} = \int PSF(x, y, z)^4\ dx\ dy \sim \frac{1}{z^2} \quad per\ z >> \lambda \tag{5.12}$$

From Eq.(5.12) it can be seen that the light intensity revealed by a uniformly illuminated plane progressively reduces in intensity moving away from the focus (focal plane: z = 0). This feature of the confocal microscope is called *"optical sectioning"*.

5.2 Experimental set-up

The set-up used for all the experiments performed is described in this section and is illustrated in the Figure 5.2. The confocal microscope is set up in order to also carry out the control using microwaves to create the ODMR graph (and post-processing the data the differential ODMR graph). As an additional branch of collection, the set-up is organized so that a lock-in measurement can be performed. Finally, the instrument for measuring neuronal firing is described.

5.2.1 Confocal microscope with ODMR control

The experimental set-up developed for this thesis is presented here. Depending on the purpose of the experiments, the collection line was specially modified.
The apparatus used to measure, by means of nanodiamonds, the temperature induced in neuronal cells (see chapter 7) is shown in Figure 5.2a. It is based on an Olympus IX73 inverted microscope, in which optical elements to implement single-photon confocal imaging and microwave control for ODMR measurements were integrated. A CW 532-nm laser (Coherent Prometheus 100NE, noise reduced regime, $2nd$ harmonics) is used to excite the NV centers in the NDs. The power of the excitation light is varied using a Neutral Density filter. Then an acousto-optic modulator (AOM), controlled by a pulse generator (Pulse streamer, Swabian Instruments), is applied to the laser emission to switch on and off the laser illumination on the sample. This solution allows to shine the laser on the sample only during the measurement time, reducing the total amount of light energy delivered to the sample. This is of key importance in biological applications. Finally, a $60\times$ air microscope objective (Olympus UPLANFL, NA = 0.67) is used for both excitation and photoluminescence (PL) collection. The spot size of the focused laser beam is $\sim (1.2 \times 1.3)\,\mu m^2$, see section 5.2.1.1). The NV PL is filtered by a 567 nm dichroic mirror, a 650 nm long-pass filter and a Notch filter centered at 532 nm to remove the residual green laser scattering, and then collected by a single photon avalanche diode operated in Geiger mode (SPAD, SPCM-AQR 15, Perkin Elmer). The emission rate from a single ND was around 300

kCounts/s. The Petri dish, containing the cell culture with NDs, was placed in a closed incubation chamber with a temperature control (Okolab Temperature Controller, temperature stability 0.1 C). The sample could be moved via a manually or software-controlled piezoelectric XYZ scanning stage allowing selecting the area of interest. The output signal from the SPAD was fed to a data acquisition board system (National Instruments, USB-6343 BNC). To implement the ODMR measurements, a microwave source (Keysight N5172B) was used. The output signal was then amplified (Mini-Circuits, ZHL 16W 43+) to a power of 20 dBm and fed to a homemade planar broadband antenna, which provided a strong, homogeneous, electromagnetic radiation, specifically designed for ODMR measurements in a 400 MHz frequencies range centered around the 2.87 GHz spin resonance. The Petri dish was placed on the top of the antenna.

In order to improve the measuring sensitivity of the magnetic field, as described in chapter 8, the collection line has been modified. In these experiments, carried out with a bulk diamond sample, the sensitivity is improved by means of the lock-in technique (see section 4.1.3 for theoretical details). The microwave control central frequency was internally modulated at $f_{mod} =$ 5001 Hz with modulation depth $f_{dev} = 0.5$ MHz, where f_{dev} represents the deviation from the central microwave frequency. For simultaneous hyperfine driving, the microwave was mixed via a double-balanced mixer with a $\sim$2.16 MHz sinewave to create two simultaneous driving modulated frequencies near the central frequency. Then, the microwave generator was connected to the LIA to provide a sinusoidal reference channel modulated at f_{mod}. A permanent magnet fixed on a translation stage, allowing micrometric movement along the three spatial axes, provided the external magnetic field applied to the diamond sample. The photoluminescence (PL) emission was spectrally filtered with a notch filter centered at 532 nm and a long-pass filter centered at 650 nm, then collected and detected with two different acquisition systems. A 4% fraction of the total PL intensity was sent to the single-photon avalanche detector (SPAD). The signal from the SPAD was used for the ODMR spectrum acquisition. The remaining 96% fraction of the emitted PL intensity was collected by NA = 0.25 objective (Olympus 10$\times$) and imaged

onto a photodetector (Thorlabs DET 10A2). Finally, the signal from the photodiode was sent to the input channel of the LIA. In the measurement of the Linear Spectral Density(LSD) of the noise, a time constant of $\tau = 300$ μs was set. For the estimation of LSD, we acquired the LIA signal for 1 minute with a sampling rate of s = 10 kHz and subsequently the LIA signal was Fast-Fourier trans- formed. The time constant of the LIA was set to $\tau = 1$ ms for the construction of the LIA spectrum.

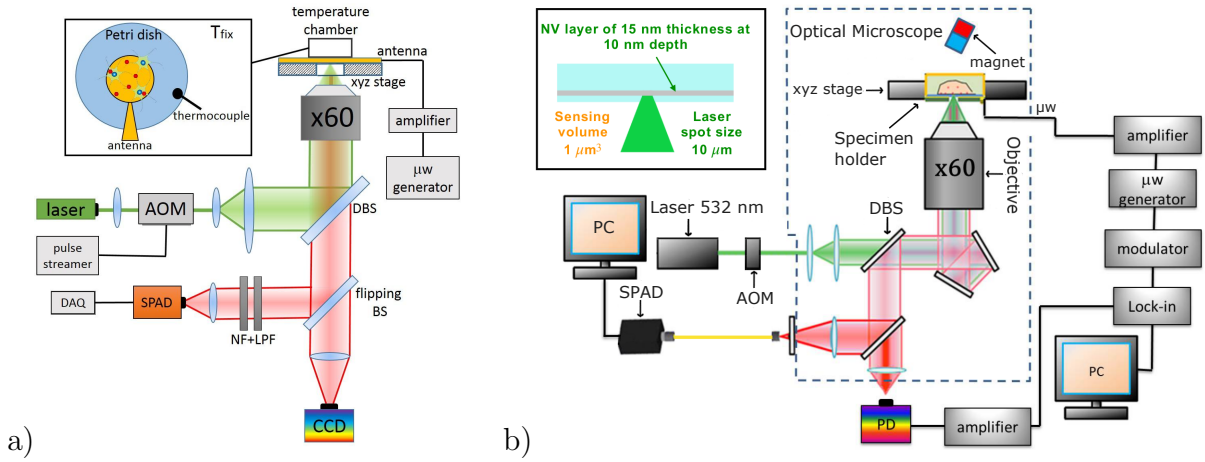

Figure 5.2: a) Experimental set-up scheme used for nanodiamonds experiment (see Chapter 6). The optical excitation using a green laser, the microwave(μw) control and the fluorescence detection are depicted. The optical excitation is switch on and off using an Acousto Optic Modulator (AOM). A Dichroic Beam Splitter (DBS) is used to separate the optical path of the green excitation and of the red photoluminescence (PL). The photoluminescence is filtered by a long-pass filter (LPF) and a notch filter (NF). Finally is collected by the single-photon avalanche diode (SPAD) and analyzed by the data acquisition board (DAQ). The cells are cultured on a Petri dish, placed inside an incubator (temperature chamber), which can be moved by means of a three-axis piezoelectric system (xyz stage). The temperature inside the closed incubation chamber is controlled by a PID and measured by a thermocouple. b) Schematics of the experimental set-up used for bulk diamonds experiment (see Chapter 7). The optical excitation and the microwave control is the same. The differences concern the presence of an additional path in the collection of photoluminescence: the lock-in detection are depicted. The 96% of the PL is then sent to a photodiode (PD), the remaining 4% is sent to the SPAD. In the inset a drawing of the bulk diamond sample is shown. The sensing layer has a thickness of 15 nm and a is localized at depth of 10 nm below the surface.

5.2.1.1 Spatial resolution of our set-up

The spatial resolution of our experimental set-up is shown below. As can be seen from the FWHM of the Gaussian in the Figure 5.3, there is a spatial resolution in the x and y planes of about 1 μm while in z of about 6 μm. These results are reasonably in agreement with the theoretical limit, which is found by inserting our set-up data into the equations (5.5) and (5.9). The theoretical resolution limit for the x and y axes is $R_{xy} \sim 0,5\,\mu m$, while that on the z axis is $R_z \sim 2\,\mu m$. The slight experimental disagreement is considered to be related to residual aberrations.
The values have been obtained using nanodiamonds of size 40 nm, placed on a slide.

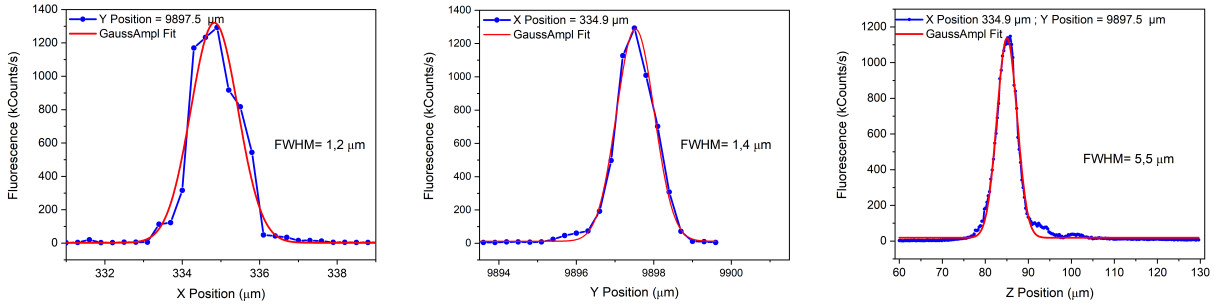

Figure 5.3: Spatial resolution of our set-up

5.2.2 Multi Electrode Arrays (MEA)

Multisite extracellular recordings were performed using the MEA-system, purchased from Multi-Channel Systems (Reutlingen, Germany). The 60 electrodes array (TiN) was composed of an 8 × 8 square grid with 200 μm inter-electrode spacing and 30 μm electrode diameter. Data acquisition was controlled through MC-Rack software (Multi-Channel Systems Reutlingen, Germany), sampling at 10 kHz.

Chapter 6

NV^- center for bio-sensing

The NV^- center plays a significant role in the field of sensors. As mentioned in section 1.2.2, the complex is in the *spin triplet* configuration and has an energy levels structure which gives it the peculiarity of having highly spin-dependent optical transitions of the electronic state.
Using the ODMR technique it is possible to measure the *splitting* between the energy levels of the center, which occur in the presence of external fields (see section 4.2) [79].
The performance of a single NV^- center as a sensor is compared with that of the main magnetic field measurement techniques, based on the use of *Hall probes*, *force sensors* and *SQUID sensors* (Superconducting Quantum Interference Devices). The use of the NV^- center allows to achieve a higher spatial resolution than other techniques, while maintaining high sensitivity even at room temperature; this constitutes a significant advantage over SQUID sensors, which require cryogenic temperatures to perform highly sensitive measurements [80, 81, 82]. There are several possible implementations for sensors based on NV^- centers. For example, a single spin associated with a defect contained in a nanodiamond can be positioned at nanometric distances from the sample and used to make precise measurements of the magnetic field and map its local properties. A possible strategy to achieve this objective is based on the insertion of NV centers on the tip of atomic force microscopes [83], in order to generate, in addition to a sample surface three-dimensional image (topography) at high resolution, also a probed magnetic forces image. Alternatively, NV^- centers present with high concentration in a diamond volume can be used to detect fields generated by distant sources with high sensitivity

(of the order of 1 $pT\ Hz^{-1/2}$) and micrometric spatial resolution.
As for the use of the NV^- center as an electric field sensor, also in this area techniques that require recourse at low temperatures to perform high sensitivity measurements is necessary. At the state of the art, sensors such as the *single electron transistor* (SET) and *tunnel effect microscopy* is used. Even in this case, the possibility offered by the NV^- center to carry out at room temperature high spatial resolution measurements with sensitivity of the order of $10^2\ V\ cm^{-1}\ Hz^{-1/2}$ constitutes a significant advantage. The NV^- center sensitivity to electromagnetic fields depends strongly by the spin coherence time τ, which is itself limited by the interaction with the other spins located in the immediate vicinity in the reticulum (in prepared samples appropriately τ can reach the value of 1.8 ms). By maximizing this parameter and using appropriate spin resonance techniques it is possible to achieve a sensitivity which, combined with the possibility of approaching the sensor at nanometric distances from the sample, allows to discriminate the magnetic fields generated by single electron or nuclear spins and electric fields generated by single elementary charges.
In addition, since the diamond, thanks to its high bonding energy, chemically inert and resistant to deterioration, this type of device is biocompatible. There are many possible applications in the biological field in which it is planned to exploit these sensors [84, 85, 86, 87, 83, 88]. For example, the NV^- center would allow the study of neuronal pulses associated with the generation of the action potential along the axons of neurons.
Finally, among the various applications in the sensor field, the NV^- center offers the possibility of detecting the temperature of the environment in which it is located, a topic that will be presented in chapter 7.

6.1 The biosensing theory

As mentioned above, NV sensors are particularly suitable for biological sensing, i.e. sensing of biological systems. Before describing the experiments focusing on the NV-based sensor it is necessary to specify the type of biological specimens of interest, the expected magnitude of the electromagnetic field

produced by these specimens and the principal parameters such as sensitivity and spatial/temporal resolution, required for the NV-based sensors.
This section, after reviewing some of the devices typically used for biosensing, analyzes in detail neuronal and cardiac cells. Higher sensitivity and resolution of electromagnetic fields is considered necessary to expand the understanding of the fundamental processes regulating the interaction of these cells.

6.1.1 From the conventional electrophysiological techniques to NV sensors

The electrical activity of excitable cells can be investigated by means of the conventional patch-clamp technique [89] or through Micro Electrode Array (MEA) [90] recordings.

- Single-cell recordings, performed under voltage- or current-clamp configuration, respectively allow to monitor ion currents or the membrane resting potential, postsynaptic responses and action potential firing activity [91]. Besides having an extreme versatility (monitoring overall electrical events from the whole cell, from microdomains of the cell membrane or even from single channel proteins), patch-clamp has a high temporal resolution and high sensitivity: all these features make this electrophysiological approach the gold standard for measuring the electrical activity. Though, patch-clamp is rather invasive, as it damages the cell membrane through the recording electrode: this implies that only one recording is feasible for each cell [92].

- On the contrary, MEA is a non-invasive approach, used to measure the membrane potential variations from many cells simultaneously. The MEA probe is structured as an array of sensing electrodes, of variable geometry dimensions and material, which are immersed in a glassy (insulating) double layer. Commonly, sensing electrodes are made of titanium or indium tin oxide (ITO), and have a diameter that can vary between 10 and 30 μm [93, 94]. By means of MEAs, it is possible to monitor the electrical activity of a neuronal network as a whole, and measuring its changes along with its maturation, even though informations on the biophysical properties of ion channel cannot be directly inferred. This

specific measurement need, requiring non-invasive and iterative detection for biological applications has prompted the study and realization of different devices. In the following I discuss and compare the most promising ones.

Promising devices for the detection of weak magnetic fields, in addition to the NV-based sensors, are the superconducting quantum interference device (SQUID) sensors [80, 82] and chip-scale atomic magnetometers (CSAMs) [95].

- Until now, the measurement of very weak magnetic fields was the domain of SQUIDs sensors. These sensors have reached sensitivity levels of (0.9–1.4) $\mathrm{fT/Hz^{1/2}}$ with a pick-up coil area of the order of 1 $\mathrm{cm^2}$. However, SQUIDs require cryogenic cooling, which, in addition to implying significant cost and maintenance complexity, requires positioning the sensor a few centimeters from the sample.

- An alternative is offered by the CSMAs, that are based on microfabricated alkali vapor cells integrated with small optical components such as diode lasers and fiber optics. These devices have reached sensitivities below 5 $\mathrm{fT/Hz^{1/2}}$ at sensor volume 8 $\mathrm{mm^3}$[95]. However, despite the exceptional sensitivity, the minimum working distance between sensor and magnetic source for CSAM or SQUIDS remains at least few mm, that makes them unsuitable for monitoring individual cell signals or small tissues, being the amplitude of the magnetic field decreasing quadratically with distance.

The sensors for the detection of electric fields, emerging in the last few decades are single-electron transistors (SETs) [96], that are a promising candidate for achieving higher detection sensitivity due to the Coulomb oscillations. However, the existence of a SET- based biosensor has emerged only in recent years [97], probably because of their difficulty of the room-temperature operation.

Finally, in recent years there has been a growing interest in the use of temperature sensors capable of operating on a nanometric scale. It has been known that local temperature variations at the intracellular level play a fundamental role in cellular activities related to body temperature homeostasis and energy balance [98]. Particular attention is paid to the possibility of measuring local

temperature variations of cell organelles (i.e. nucleus, mitochondria, etc.) or ion channels. For example, different simulation model [99, 100] shows a hypothetical variation in temperature at the level of the ion channels, due to the flow of the ions from the inside to the outside of the plasma membrane, during the genesis of the action potential. Due to the difficulty of this local measurement, no one has ever measured this thermal variation. Interestingly, temperature changes may drastically alter the neuronal firing frequency, as demonstrated by Guatteo et al.[101]. Currently fluorescence probes are powerful method used to study intracellular temperature variation thanks their high spatio-temporal resolution. The probes typically used for this measurement are organic or inorganic fluorescent probes, such as fluorescent proteins, organic dyes [102, 103, 104, 105], quantum dots (QDs) [106, 107] and many others.

- Organic proteins are biocompatible probes, rather stable and very easy to chemically target. But there are different problems related the use of these probes: these are often autofluorescent and to avoid the phenomenon it is necessary to add specific quenchers; they cannot be used for a long time, in fact these sensors suffer from photobleaching and unstable photoluminescence. In the best case scenario, the probe degradation consists of fluorescence suppression, in the worst case scenario it releases an electron that binds to nearby molecules making them toxic. These probes are organic and by their nature they are also subject to even weak pH variations, for this reason it is fundamental a strict control of the cell environment [108, 109].

- The inorganic probes such as quantum dots (QDs) have the advantage of being stable in fluorescence, have a high sensitivity to temperature variations and their nanometric size allows obtaining a spatial resolution useful for cellular measurements. Although the size of these sensors would allow spatial resolution limited by the diffraction limit only, their chemical composition is found to be non-biocompatible in most of the cases.

- Other temperature sensors are based on up converting nanoparticles (UCNPs) [98, 110]: nanoscale particles (diameter 1-100 nm) that exhibit

photon upconversion, i.e. when stimulated by incident photons they are able to emit fluorescence's of shorter wavelength. They are usually composed of rare-earth based lanthanide or actinide-doped transition metals. Their core-shell structure allows sensor compatibility, however, sensitivity is not high.

- Extremely interesting devices able to realize all these measurements (magnetic, electrical and temperature sensing) eventually at the same time, are one based on the NV center in diamond. The advantages of these sensors are manifold: they have stable photoluminescence in the visible and near-infrared range, their chemical composition ensures resistance to photobleaching and diamond is an inert and therefore biocompatible material [111], so cell/neurons can be grown directly on its surface [112, 113, 114] or nanodiamonds can be injected inside them, allowing for sub-cellular spatial resolutions [115] with a non-invasive techniques. Finally, NV sensors can operate at room temperature and, in more detail, their dynamical range of temperature sensing extends further 500 K for both bulk [116] and nanoscale [117] diamonds.

The various sensors discussed are shown in the Table 6.1, where the main advantages and disadvantages that differentiate them are stated. In the remainder of this section, the modelization of the target neural and cardiac signals for NV-based biosensing will be reviewed.

6.2 NV sensor for bio-electromagnetic signals

6.2.1 NV center as sensor for neuronal signals

In the last decades, neuroscience has attracted great interest beyond the scientific community. Because of the increase in life expectation, cases of neurodegenerative diseases such as Parkinson's, Alzheimer's, Huntington's disease and many others are constantly growing. Currently, these diseases are incurable, even symptoms mitigation is difficult because of late diagnosis when most of the neurons involved have been irreparably damaged. This reason strongly prompts to develop new increasingly precise and sensitive techniques, allowing a deeper understanding of neuronal circuits ranging from

sensors	application	advantages	disadvantages
patch-clamp	electrical cells activity	-high time resolution -high spatial resolution (ion channels level) -high sensitivity	invasive (no-biocompatible)
MEA	electrical activity of a neuronal network	non-invasive	low spatial resolution (many cells)
SQUID	weak magnetic fields	1 $fT/Hz^{1/2}$ - 1 cm^2	-cryogenic cooling -cost -low spatial resolution (few centimeters)
CSMAs	weak magnetic fields	5 $fT/Hz^{1/2}$ - 8 mm^3	-low spatial resolution (few centimeters)
Organic proteins	intracellular local temperature variations	-biocompatible -high spatial resolution nanometric scale	-photobleaching -photoblinking -toxic (some times)
QDs	intracellular local temperature variations	-high sensitivity -nanometric size	non-biocompatible
UCNPs	intracellular local temperature variations	bio-compatible	low sensitivity
NV-centres	magnetic, electrical and temperature sensing	-stable photoluminescence -biocompatible -room temperature	

Table 6.1: Summary of the various types of sensors and their main characteristics.

functioning of synaptic sites to the behavior of the entire neuronal network. Neurons are the functional units of the nervous system. They communicate via electrical signals, known as action potentials.
The action potential (AP) consists in the variation in time of the membrane potential V_m, where $V_m = \Phi e_{in} - \Phi e_{out}$ is the electrical potential difference between intra- and extra-cellular side of the cell membrane. The AP characteristic waveform is shown in Figure 6.1b). The AP pulse is caused by several ionic species (Na^+, K^+, Ca^{2+}), which flow through the neuronal membrane.
The two electrophysiological techniques mostly used to study cell excitability and synaptic transmission in a neuronal network are the patch-clamp and the MEA. In the last decade scientists have tried to study more and more specifically the propagation of the electrical signal from the cell body (or soma) to the whole dendritic tree. In other words, the goal would be to create a device that allows scanning the neuron point by point from the soma to the axon and the dendrites, following and characterizing the electrophysiological variations of the electrical signal during its propagation. The technology closer to this ambitious goal is the one of the CMOS-MEA, that allows having a much higher density of electrodes with respect to the traditional MEA technology. Numerous studies have managed to scan the path of the electrical signal in a neuronal network at the level of the single neuron [118, 119, 120].

Bakkum et al.[120] recently have developed a high electrode density CMOS-MEA device capable of stimulating a specific area and simultaneously scanning the signal along some points from the soma to the axon. Clearly, this technique is much more sensitive than MEA, but given the stochasticity of the cell's placement in space, it requires cells to be marked in order to follow their path. Recently several groups have correlated this technology to the technique of optogenetics. They tagged the genes of interest and activated them following an optical stimulation and simultaneously followed the signal thanks to the integration of the CMOS-MEA [121, 122].
However, these techniques do not allow following the entire dynamics of the action potential, but to have a scan of a region depending on the position of the electrodes with respect to the neuron with its axon and its dendritic body.

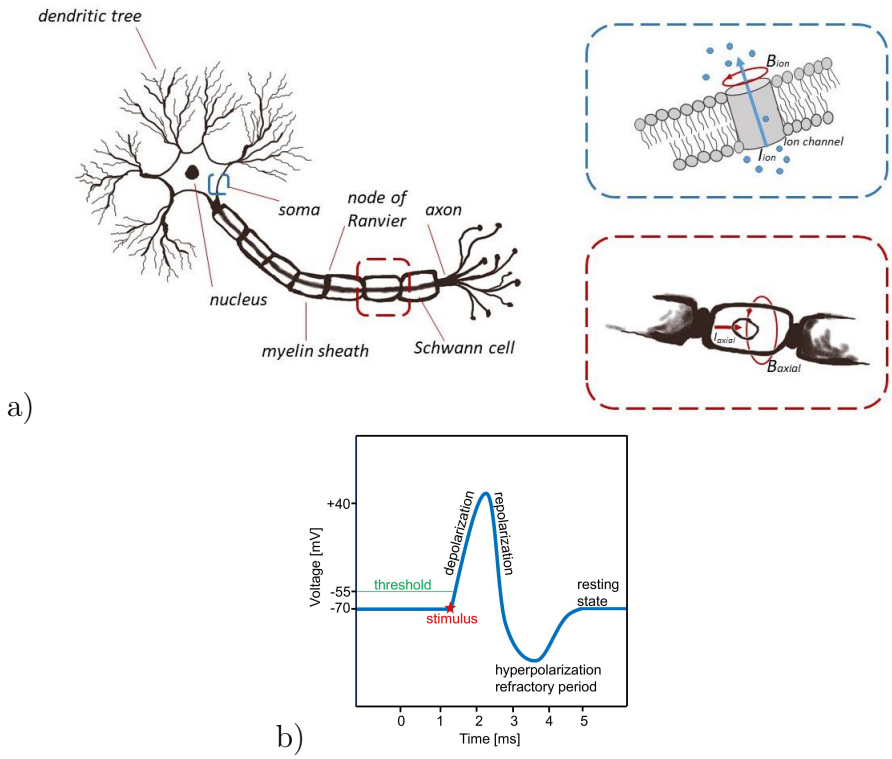

Figure 6.1: a) Single neuron simplified sketch. In the upper box a zoom of the neuronal membrane is reported, where the ionic current and the corresponding magnetic field are schematized. In the lower box the axial current and the relative magnetic field are shown. b) Schematic representation of neuronal action potential (AP). Resting membrane potential (-V_m) is -70 mV. When V_m is driven and exceeds the threshold (following an initial stimulus), a rapid membrane depolarization occurs. In this phase the Na^+ channels open, allowing sodium to enter in the neuron and bringing V_m to approximately +35 mV. Then the repolarization phase begins, caused by Na^+ channels inactivation and opening of K^+ channels. This outward current drives the membrane potential close to -93 mV (hyperpolarization). Finally, the Na^+/K^+ ATP-ase restores the initial conditions. During the depolarization, the influx of positive charges produces local internal and external longitudinal currents, which are responsible for the AP propagation in the axon adjacent area. The propagation directionality is guaranteed by the AP refractory period: although the local currents propagate in both directions, a new AP cannot be triggered in refractory membrane area.

NV sensors may therefore have a huge impact on these applications: nanodiamonds can be targeted on the membrane surface or, alternatively, cells can be plated and cultured on a bulk diamond [123]. Indeed, taking advantage of diamond biocompatibility and the exceptional spatial resolution displayed by color centers in diamonds , it will be worth exploiting these properties for

a timely reconstruction of the AP dynamics. Furthermore, the possibility of positioning them adjacent to the cell membrane has the advantage of experiencing stronger magnetic fields. However, since neuronal magnetic fields are extremely weak ($\simeq pT$), their detection appears to be challenging even for NV-based sensors, at least for mammalian cells, while measurements have been performed on giant neurons of invertebrates [113].

To predict the electromagnetic fields intensity created by the AP, and therefore to understand what sensitivity of the NV sensors is needed to sense it, it is necessary to model how the AP develops and propagates.

Hodgkin-Huxley model [124, 125, 126, 127] allows estimating the ionic current flowing through the neuron membrane (when the ion channels are open). For the human neuron, the total estimated ionic current, sum of the single channels contribution I_{ion} is:

$$I_{\perp} = \sum I_{ion} \simeq 2\ pA\ \mu m^{-2}$$

and the current pulse typically lasts $\Delta t\ \simeq\ 1\ ms$. Each I_{ion} generates a magnetic field (see Figure 6.1a)), which can be estimated by means of the Biot-Savart law: $\oint_C \vec{\boldsymbol{B}}_{\boldsymbol{ion}} \cdot \vec{\boldsymbol{l}} = \mu_0 I_{ion}$. However, the resulting amplitude of these fields depends on the channels density, which largely varies depending on the axon area being considered. Furthermore, we note that the $\vec{\boldsymbol{B}}^{\boldsymbol{tot}}_{\boldsymbol{ion}}$ field, sum of the contributions of the field produced by the various channels, can be vanishingly small on average, because of the different fields directions. To this purpose, channel clustering may be very significant [128, 129]. Assuming a current of 100 $pA/\mu m^2$ and considering that the NV sensor positioned at an average distance of few nanometers (by selective targeting the channel using functionalized NDs [130, 131]), a magnetic field of about $0.1 - 5\ nT$ (or even higher) could probably be sensed. This hypothesis is now under experimental analysis.

Current flowing through the membrane is not limited to the charge flow through ion channels, as longitudinal currents, but one should also consider the flow along the neuron axis, that is responsible for the AP propagation. These currents also generate a magnetic field, around the neuron (see Figure 6.1a)). Both the axial current and the corresponding magnetic field have been estimated [132, 133, 134]. In particular, Ref.[132] goes beyond the simplification of the Hodgkin-Huxley model, introducing the spatial and temporal

progression of the AP along the various neuronal compartments, into which they have divided the axon. The theoretical prediction is a maximum field $B_{axial} \simeq 3$ pT on the external membrane near the Ranvier node and a field $B_{axial} \simeq 2.3$ pT on the myelin sheath external surface in those regions where the axon is wrapped by it.
The maximum magnetic field was also calculated by Isakovic et al. in Ref.[132] for the nerve composed of 100 axons, obtaining only $B_{axial} \simeq 6$ pT. This is due to the cancellation of the magnetic field component, caused by different axons within the same nerve, bringing opposite directional currents. This estimated magnetic fields, in reality, are compatible with the fields detected by magnetoencephalography (MEG). MEG is able to detect fields if the order of 10^{-15} T because of the distance from the source [135].
Considering these values, a NV sensor positioned on the neuron surface or a few micrometers from it, should have a temporal resolution of about 0.1 ms (in order to be able to trace the time variation), and spatial resolution of about 10 μm^3 (which would allows a good reconstruction of the AP propagation, being the axon length ranging from 0.1 μm to 1 m). Thus, the NV sensor should have a minimum sensitivity of [136]:

$$\eta = \delta B_{min}\sqrt{\Delta t} \simeq 3\ pT\sqrt{0.1\,ms} \simeq 30\,fT\,Hz^{-1/2} \tag{6.1}$$

The NV sensor optimal sensitivity is in principle limited by the quantum projection noise. This fundamental sensitivity limit for spin-based magnetometers is given by [137]:

$$\eta_q = \frac{1}{\gamma_e}\frac{1}{\sqrt{nT_2^*}} \tag{6.2}$$

Where γ_e is the magnetic coupling coefficient (Table 4.1), n represents the number of NV centers and T_2^* their characteristic dephasing time. It is important to underline that the number of NV centers n refers to the sensing volume. As mentioned, for the single PA detection the sensing volume should be around 10 μm^3, the size of the cell.
In the Ref.[113], the estimation of the parameters $n \simeq 3 \cdot 10^6$ cm^{-3} and $T_2^* \simeq$ 450 ns determines a spin projection noise value of $\eta_q \simeq 30$ pT Hz$^{-1/2}$ for the sensing volume of 10 μm^3 (the experimental sensitivity reached is instead $\eta \simeq$ 15 pT Hz$^{-1/2}$ for the sensing volume of $5 \cdot 10^6$ μm^3). This value is still 1000

times larger than the sensitivity required for the detection of a single AP. However, as will be discussed in chapter 8, it is possible to optimize both the above mentioned parameters to improve the performances.

Once the biomagnetic field $\vec{\boldsymbol{B}}(\vec{\boldsymbol{x}}, t)$ has been measured, to reconstruct the unknown currents generating it, one should solve an inversion problem. In general, its solution is not unique, due to the existence of the so-called "magnetically silent" currents (i.e. the ones producing magnetic fields that almost cancel each others) and due to the fact that the magnetic field can be influenced by the electric field [138, 139]. However, in the single axon case, it can be uniquely resolved. On the contrary, in the biological tissue case and in the 3D structures case, that cannot be traced back to standard models (such as a spherically symmetrical conductor or a horizontally layered medium), the solution is not unique. In some cases this is resolved by the knowledge of the electric field on the conductor surface [138].

6.2.2 NV center as sensor for cardiac signals

The human (and animal) heart generates the body's most intense electromagnetic field. In particular, by comparing measurements performed externally to the human body, the electric field generated by the heart, measured through the electrocardiogram (ECG) is about 60 times stronger than that the one of the brain, recorded by an electroencephalogram (EEG). In addition, the heart magnetic field detected by the magnetocardiogram (MCG) is about 5000 times higher than the neuronal magnetic field detected by magnetoencephalography (MEG): 0,05 nT (heart) vs 1 fT (neuron). Thus, ODMR based on NV sensors can also find very significant applications in studying cardiac cells and tissues. To achieve a first qualitative estimation of the magnitude of the magnetic field in this case, one can start from a very simplified model: the spherical heart [140]. Although this model is not physiologically accurate, it allows to extrapolate analytical solutions.
In a more recent work [141], is proposed a further assumption concerning the origin of the currents. There are two currents sources in the heart: the first consists of intracellular currents, the second is given by the anisotropy of the tissue [142]. Regarding the first current contribution, the authors consider

a spherical shell of cardiac tissue, which covers a blood cavity and is surrounded by an external bath of unlimited electrical conduction. The heart fibers propagate in the z direction and a variation of the membrane potential V_m is assumed following the activation of the action potential (AP), started at $\theta = 90°$ (see Figure 6.2a)).
In this work the electric field is evaluated using the bidomain model [140] and considering a situation of quasi-stationarity (although V_m depends on time due to the action potential propagation, it is assumed that, given a certain $V_m(t_0)$, one can derive current and magnetic field in a quasistatic way).
Thus, the electric potential is obtained, using the continuity equations and the boundary conditions [143, 144], the current density distribution is obtained using Ohm's law and finally the magnetic field using Biot-Savart's law. Considering the anisotropic electrical conductance data [145], the V_m values and typical heart dimensions [140], it turns out that the magnetic field is stronger near the internal and external surfaces tissue while it is weaker in the heart wall. The peak value of the magnetic field is around 14 nT (see Figure 6.2b)).

At the heart center, instead, the magnetic field reduces to $B = 2$ nT [146]. This is due to the fact that intracellular and extracellular currents are in opposite directions with almost the same magnitudes in the depths of the tissue and, therefore, the corresponding magnetic fields essentially cancel each other.
Considering a planar cardiac tissue sample, the spherical shell method is no longer valid. In this last case it has been found that the magnetic field reaches a peak value $B = 1$ nT [147].

The heart AP is about $\Delta t = 300 \div 500$ ms long, however for some cardiac cells, such as ventricular or rapid response cells, the AP rapid rise occurs in 1 ms, as in the neuronal case. Considering a human heart, a NV sensor positioned on the heart surface should be sensitive to magnetic field $B = 14$ nT, with a temporal resolution of about 0.1 ms (in order to be able to trace the time variation Δt even in the case of the AP rapid rise), and a spatial resolution of about 10 μm^3 (which would allow a good reconstruction of the PA propagation, being the heart radius of about 40 mm [140]). This

corresponds to a minimum sensitivity:

$$\eta = \delta B_{min}\sqrt{\Delta t} \simeq 14\, nT\sqrt{0.1\, ms} \simeq 140\ pT\, Hz^{-1/2} \tag{6.3}$$

This value can be considered a useful intermediate step for the application of the actual NV^- based biosensing technologies, with the aim of reaching sensitivity that allows the detection on neuronal signals.

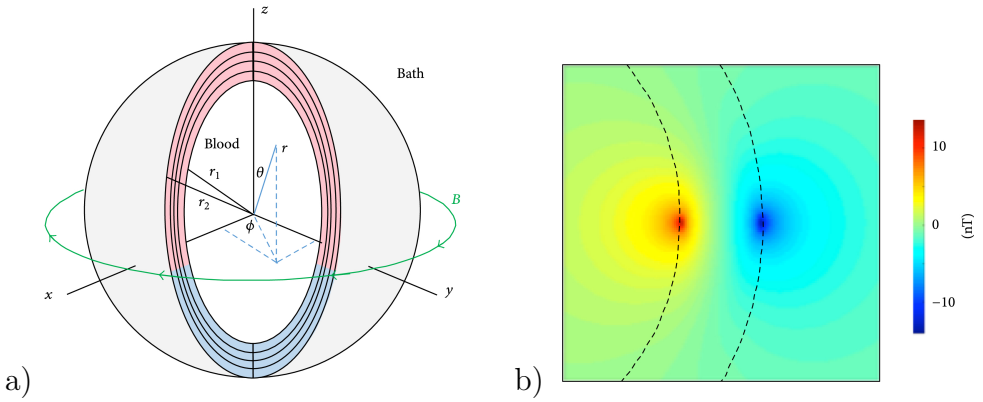

Figure 6.2: a) The model of a spherical heart, taken from the reference [141]. Part of the spherical shell has been cut out to show the heart wall. The black curves indicate the fiber orientation. The pink tissue has a transmembrane potential of 20 mV, and the blue tissue has a transmembrane potential of −80 mV. The green curve shows the magnetic field. The endocardial (inner) surface has radius r_1, and the epicardial (outer) surface has radius r_2. b) The magnetic field over a cross section of the heart. The dashed curves indicate the heart inner and outer surfaces. An area 40 mm by 40 mm is shown.

6.3 NV sensors for bio-termometry

Temperature is one of the most relevant parameters for the regulation of intracellular processes. Measuring localized subcellular temperature gradients is fundamental for a deeper understanding of cell function, such as the genesis of action potentials, and cell metabolism. Notwithstanding several proposed techniques, at the moment detection of temperature fluctuations at the subcellular level still represents an ongoing challenge. On the one side, temperature regulates the speed of ion channel opening [1], the pattern activity of a firing neuron [2] and the vesicular dynamics at the presynaptic terminal [3],

on the other side, intracellular temperature is affected by a variety of biochemical reactions occurring during cell activity. Pioneering findings dating back to the late 70's [148, 149] associated temperature increases to the impulse propagation in non-myelinated fibers of the olfactory nerve and, more recently, a theoretical explanation about the heat production and absorption by neurons during nervous conduction has been formulated [150]. Intracellular temperature variations have been probed to detect the phases of cell-cycle division [151] and the mitochondrial activity [152]. In the brain, temperature fluctuations are likely associated with changes in neuronal functions such as the genesis of action potentials, secretion at the level of synaptic terminals, or transmembrane ion transports [153, 154, 155]. Variation of intracellular temperature is also related to changes in cell metabolism, as observed through positron emission tomography (PET) and functional magnetic resonance imaging (fMRI) [156]. Besides its fundamental role in cell physiology, the temperature may be altered under pathological conditions, such as in cancerous cells [157], which display higher metabolic activity, in neurodegeneration, such as Parkinson's or Alzheimer's diseases, where the process of abnormal protein aggregation is temperature-dependent [158], or during the onset of malignant hyperthermia, a pathology that causes rapid temperature increases following excessive muscle contraction [159]. Furthermore, an increase in local temperature, up to a few Celsius degrees, has been detected as triggered by laser heating [160], calcium stress [103], direct electric stimulation [161] or using drugs that increase the heat produced during cellular respiration [160, 161, 162]. These results, in particular the ones related to the highest temperature variations, stimulated a debate since the power needed to justify this temperature growth has been calculated to exceed a few orders of magnitude what is expected by thermodynamic considerations in a model where thermal diffusion is characterized by conductive regime [163]. Nonetheless, other authors [164, 165] suggested that, by taking into account the inhomogeneity of the cells, this gap can be strongly reduced. However, detection of temperature fluctuations at the subcellular level still represents an ongoing challenge and several intracellular thermometry techniques are reported in the literature, ranging from fluorescent molecular thermometers [166], quantum dots [167] or rare-earth nanoparticles [168]. Compared to

the above-mentioned methods, nanodiamonds (ND) show a better biocompatibility [169, 12], insensitivity to biological environment [170], more stable photoluminescence (PL) and a lower noise floor [171]. All-optical temperature measurement methods, based on the temperature-dependent shift of the luminescence spectra of color centers in diamond such as silicon-vacancy (SiV), germanium vacancy (GeV), and tin vacancy (SnV) with strong zero-phonon line (ZPL), can be used [172]. These methods are promising, but for the moment, apart from one very invasive experiment [173], there are few reported biosensing applications. For instance, in a notable experiment [174], gold nanorod–fluorescent ND hybrids were used as nanoheater/nanothermometer for studying living human embryonic kidney cells. In this case the NDs registered the temperature variation associated with the heating obtained by local laser irradiation of the nanorods. In another recent experiment [175], SiV in NDs were used to for imaging and temperature measurement in HeLa cells, even if only the average temperature of the bath (by controlling the incubator temperature) was measured, without single-cell resolution. It must be stressed anyway that, in both the above mentioned works, the temperature variation was induced by the experimenters (i.e. via laser irradiation or by changing the incubator temperature) and no authentic biological phenomenon was measured. Notwithstanding the undoubted promising perspective of all-optical methods, currently the most promising approach exploits nitrogen-vacancy (NV) centers [171]. For these reasons, NV color centers in ND combined with Optically Detected Magnetic Resonance (ODMR) technique can assume a dominating position in thermometry [176] for biological application [151, 177]. Nevertheless, ODMR measurements protocols are based on microwave irradiation of the samples, which makes this technique more elaborated and requires awareness on the exploitable optical and microwave power providing the required sensitivity without damaging the cells. ND was used for the first time in in vitro [115] measurements (of a heated gold nanoparticle inside a cell). Subsequently, an in vivo experiment was performed inside Caenorhabditis elegans worms, reaching a sensitivity as low as 1.4 $^{\circ}\mathrm{C/Hz^{-1/2}}$. In the same experiment, thermogenic responses have been monitored during the chemical stimuli of mitochondrial uncouplers [160]. Temperature gradients have been mapped at the subcellular level into a single human embry-

onic fibroblast [151]; intracellular temperature mapping has been performed also in cultured primary cortical neurons, employing microelectrode arrays (MEAs) to demonstrate that the presence of NDs in primary cortical neurons does not elicit a neurotoxic response [87], in good agreement with our previous findings [169]. Finally, heterogeneous temperature variations have been coupled with Ca^{2+} increases in HeLa cells [178].

Chapter 7

Nanodiamonds quantum sensors experimental results: thermal biosensing in living cells

This chapter summarizes one of the more relevant experimental results obtained during the PhD activity. For the first time, we quantify the direct correlation of intracellular temperature variations with the modulation of neuronal activity. We demonstrate that sensors based on NV centers in nanodiamonds, interrogated via ODMR techniques, reveal up to 1 °C temperature variation when the spontaneous firing of hippocampal neurons is potentiated by picrotoxin or the 0.5 °C temperature decrease when the neuronal activity is silenced by a solution containing tetrodotoxin and cadmium chloride.

In the next sections the nanodiamonds and the cells sample used are explained in detail. Then, the necessary preliminary studies are discussed. The first of these studies highlights how the measurement carried out using the ODMR technique is biocompatible and therefore does not alter the cells vitality. The second one shows, through a firing measurement, how neuronal cells react to the chemical substances perfusion. Then the temperature measurement is presented performed on neuronal cells during the perfusion of picrotoxin and of the solution composed of tetratoxin and cadmium.
The content of this chapter is taken from the published article, see ref.[179].

7.1 Nanodiamonds

The nanodiamonds were supplied by Microdiamant Switzerland (MSY 0–0.25, containing approximately 100–200 ppm of natural nitrogen impurities).
The nanodiamonds were subsequently treated and irradiated by the colleagues of the Institute of Organic Chemistry and Biochemistry of the Czech Academy of Sciences. The preparation steps are summarized below. The NDs were oxidized by air oxygen at 510 °C for 5 h and then wet oxidized in a HF:HNO3 2:1 v/v stirred mixture at 160 °C for 2 days in a PTFE container. The acids were removed using consecutive centrifugation/washing and the resulting pure oxidized NDs were lyophilized. The monodisperse NDs (hydrodynamic diameter 205 nm) were isolated.
A total of 330 mg of the monodisperse ND was irradiated at 870 °C in an external target for 80 h with a 15.7 MeV electron beam ($2.5{\cdot}10^{19}$ particles cm^{-2})[131]. After irradiation, the NDs (315 mg) were annealed at 900 °C for 1 h under argon atmosphere and subsequently oxidized in air for 5 h at 510 °C. The resulting FNDs were wet oxidized using a 2:1 (v/v) mixture of $HF:HNO_3$, washed and lyophilized, providing 212 mg of NDs with NV centers (yield 64 %). Before use, the lyophilized NDs were redispersed in MiliQ water using cup horn sonication to concentration 1.0 mg/ml.

7.1.1 Nanodiamond characterization

In order to use nanodiamonds as sensors, it is necessary to know their characteristics in advance. In particular, it is necessary to know the nanodiamonds coupling constant $\partial D_{gs}/\partial T$ with respect to thermal variations and the measurement technique sensitivity.
The coupling constant links the shift of the resonance frequency, measurable through the ODMR graph (see Figure 7.1 for a resonance frequency shift example), with the thermal variation that has occurred. From the knowledge of this parameter (that varies in the different nanodiamonds batches) is possible to trace an indirect temperature measurement.
The thermal sensitivity is a figure of merit and it represents the minimum temperature variation that can be measured in a single second. Once this value is known, it is possible to design a measurement integration time suit-

able for particular thermal variation detection.

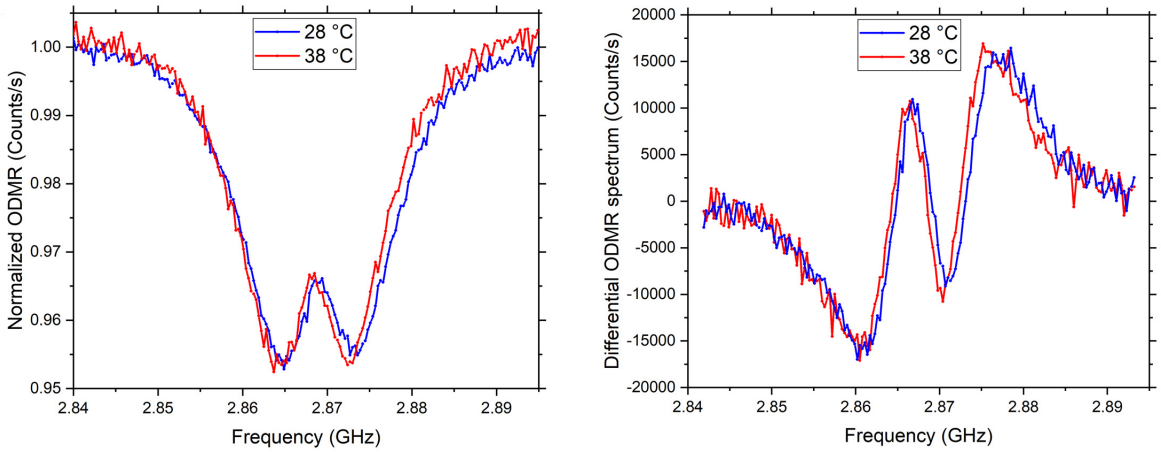

Figure 7.1: Example of ODMR and differential ODMR spectra at two different temperatures.

7.1.1.1 Estimation of $\partial D_{gs}/\partial T$

Under ambient conditions the coupling constant $\partial D_{gs}/\partial T$ is estimated as 75 kHz/°C for a bulk diamond [60, 61]. For NDs this constant varies due to the different strain splitting and, in principle, should be calibrated. The method to obtain $\partial D_{gs}/\partial T$ was the same adopted for the cell temperature measurement, with the difference that in this case ΔT was not induced by a substance perfusion but forced by the incubator chamber's heater, and that ΔT is measured by a thermocouple. The procedure was the following. The NDs were placed on the Petri dish with distilled water. The ODMR spectrum was acquired and so was the differential spectrum by post-processing the data, see above. The linear region slope of the differential spectrum was obtained by performing a linear regression. The microwave generator was set at the resonant frequency D_{gs,T_0} that occurred in the initial temperature condition reached in the incubator chamber, at which the differential spectrum signal $\tilde{F}$ was zero. The incubator temperature was varied, recording it with the thermocouple. The new value of the differential signal was read. Finally, $\Delta\tilde{F}$ was plotted as a function of the temperature increase ΔT recorded by the thermocouple. Through a linear regression the constant of proportionality b was evaluated, i.e. the quantities mentioned obey the following physical

relationship:

$$\Delta\tilde{F} = b \cdot \Delta T \tag{7.1}$$

where:

$$b = slope \cdot \partial D_{gs}/\partial T \tag{7.2}$$

By inverting the last equation, the quantity $\partial D_{gs}/\partial T$ was estimated. The results are shown in Table 1. Both the arithmetic mean and the weighted mean coincide: $\partial D_{gs}/\partial T = (-76 \pm 4)$ kHz/°C. We used this estimated value for and the associated uncertainty in our data analysis.

$\frac{\partial D_{gs}}{\partial T}$ $\left[\frac{kHz}{°C}\right]$
79 ± 6
63 ± 9
76 ± 12
86 ± 12
72 ± 8
81 ± 10

Table 7.1: Summary of NDs (N=6) coupling evaluations and their associated uncertainty, obtaining through the uncertainty propagation.

7.1.1.2 Temperature Sensitivity

In order to evaluate the sensitivity of our ND-based sensors, a control calibration test was performed. The NDs were deposited on a glass slide and inserted into the temperature chamber of the single-photon confocal microscope. The differential signal was evaluated (10 measurements with duration 60 s) at three different temperatures and then compared with the readout of a standard thermocouple. Figure 7.2 shows the response of the ND sensor to a thermal cycle with steps 0.5 °C, 1.2 °C (chamber temperature stability 0.1 °C). The average values are shown in the figure next to each dataset. The results are in agreement with the bath temperature recorded by the thermocouple, shown in the legend box. This control test highlights the sensitivity of the measurement method, capable of discriminating a variation of 0.5 °C. Our sensitivity is about 3 °C/$\sqrt{Hz}$ and is estimated according to the following

equation:

$$\eta = \frac{\sigma_{\tilde{F}} \cdot \sqrt{\Delta t}}{slope \cdot \gamma_T} \tag{7.3}$$

where $\sigma_{\tilde{F}}$ represents the standard error of the mean of the variation of the differential counts and Δt represents the measurement time.

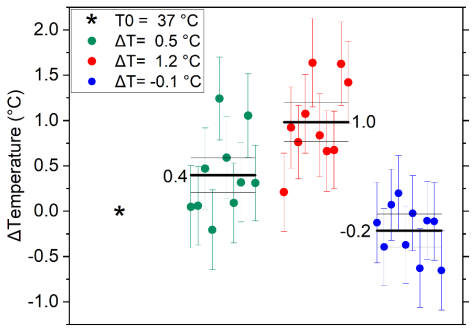

Figure 7.2: Validation of temperature detection by ND sensor. The legend box shows the temperature values recorded by the thermocouple. The box plot shows the temperature values recorded by the ND sensor. The mean and its uncertainty (standard deviation divided by the square root of repeated measurements) are reported as horizontal lines in each data set (N = 10, 60 s acquisition). The starting point is highlighted as an asterisk. The incubator temperature at the end of the cycle is consistent with the initial temperature within the incubator stability (0.1 °C).

7.2 Cell sample

Mouse neuronal cortex cells were used for this experiment. The cell sample was supplied by the Department of Drug and Science Technology - University of Torino.

The steps of the preparation are summarized below. Hippocampal neurons were obtained from C57BL/6 16-day embryos. Hippocampus was rapidly dissected under sterile conditions, kept in cold HBSS (4 °C) with high glucose, and then digested with papain (0.5 mg/ml) dissolved in HBSS plus DNAse (0.1 mg/ml). Isolated cells were plated at density of 1200 cells/mm^2 onto the MEA and 1000 cells/mm^2 onto the glass Petry dishes. Both the MEAs

and the dishes were previously coated with poly-DL-lysine and laminin, this allowed the neurons to adhere to the center of the device by using a ring made of Sylgard 184 (Dow Corning), which was removed after 4 h. The cell medium is composed of 1% penicillin/streptomycin, 1% glutamax, 2.5% fetal bovine serum, 2% B-27 supplemented neurobasal medium.

In our laboratory the neurons were incubated in a humidified 5% CO2 atmosphere at 37 °C. Recordings were carried out at 10-12 days in Vitro (DIV). The initial ND solution (1 mg/ml, MiliQ water) was sonicated for 5-10 minutes (100 W power, 80 kHz frequency), in order to separate diamond particle clusters into single NDs. After sonication, the 60 μl of solution was diluted with 1 ml of Tyroide to obtain a final ND concentration of 0.6 μg/ml which was poured into the Petri dish. The dish was exposed to NDs for 5 hours in order to allow NDs internalization. It is important to underline that this concentration is far below the cytotoxicity threshold (<250 μg/ml), as demonstrated in a previous work of our group [169] and by [180].
Once the dish was extracted from the incubator, the cell medium was removed and replaced with 2 ml of Tyrode solution. The sample is so ready for the measurement.

7.2.1 Cell survival and biocompatibility study with MEAs

Multisite extracellular recordings were performed using the MEA-system, purchased from Multi-Channel Systems (Reutlingen, Germany), see section 5.2.2 for working principles details.
Experiments were performed in a non-humidified incubator at 37 °C and with 5 % CO_2, maintaining the culture medium. Before starting the experiments, cells were allowed to stabilize in the non-humidified incubator for 5 minutes; recording of the spontaneous activity was then carried out for 120 s. Mean frequency has been evaluated over 120 s recording. The data are analyzed using Neuroexplorer software (Nex Technologies, Littleton, MA, USA) after spike sorting operations.

Before measuring the chemical-induced temperature change that can occur in neuronal cells, it is essential to assess the biocompatibility of the measure-

ment technique. For this purpose, neuronal firing was measured before and after cell exposure to the ODMR technique. In particular it has been tested whether the laser exposure, microwave radiation and incubation with NDs could affect the spontaneous firing activity of hippocampal neurons during ODMR measurement protocol. As shown in Figure 7.3c, both the spontaneous firing rate and the action potential waveform were not significantly altered by laser and ND exposure, confirming that cell excitability and ion channel functioning are preserved, in good agreement with our previous findings [169].

7.2.2 Correlation between neuronal firing and substance (picrotoxin and tetratoxin-cadmium) perfusion study with the MEA

Finally, in parallel with the thermometry experiment, the effect of GABAA receptor blockade on burst-firing of hippocampal neurons was assessed by comparing the spontaneous burst ratio of cells responses before and after application of picrotoxin. These recordings have been performed by means of conventional MEAs (MCS, multichannel system). An expected significant increase of the spontaneous activity [181] (from 2.1 $\pm$ 0.3 Hz to 3.4 $\pm$ 0.3 Hz), which is associated to disinhibition of GABAA receptors (Figure 7.3a), and a complete silencing of the network in the presence of the Na^+ and Ca^{2+} voltage-dependent channel blockers TTX and Cd was observed. The presented data allowed to conclude that the increase in temperature recorded in the experiment is directly related to the altered firing activity of hippocampal neurons.

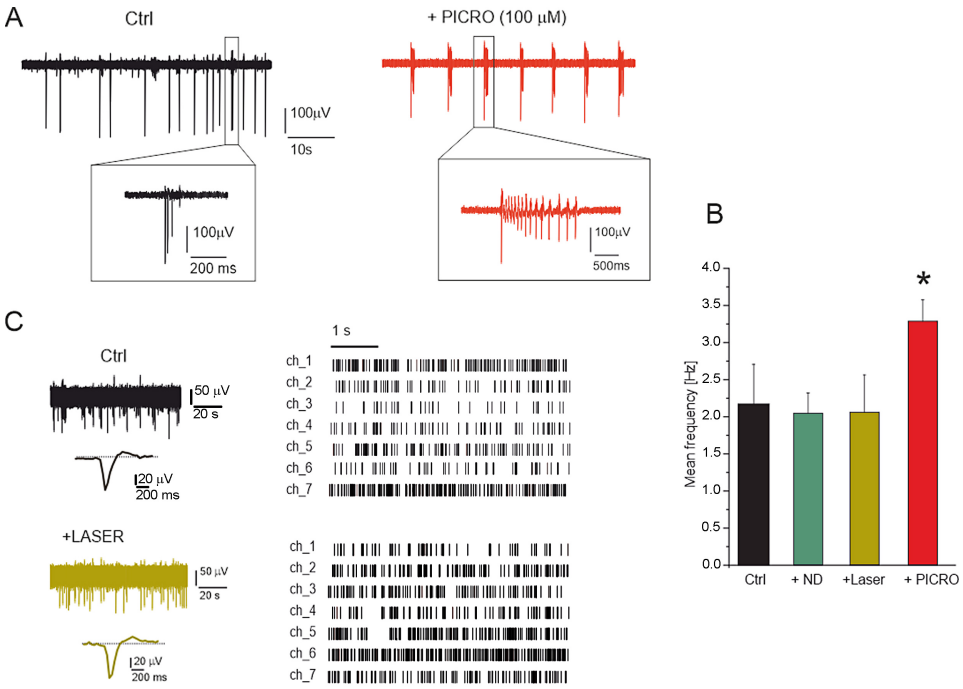

Figure 7.3: Laser exposure does not affect the hippocampal neurons. a) Modulation of the firing activity by PICRO (MEA recordings): representative traces from the same electrode under control condition, + PICRO. Insets: higher magnification of single spikes and bursts. b) Histogram of mean frequency in the different experimental conditions. The statistical difference of PICRO respect to other conditions is indicated ($p<0.05$, *) c) Left: Representative traces in control condition and after laser irradiation and (right) corresponding raster plot. In the raster plot, 7 representative channels (ch1÷ch7) are shown.

7.3 Temperature variation induces by picrotoxin and tetratoxin-cadmium perfusion measurement

This section illustrates the main part of the experiment conducted. After the explanation of the experimental measurement technique, the data obtained and finally their statistical analysis are presented.

7.3.1 Experimental procedure

The thermometric apparatus used for the experiment was based on a single-photon-sensitive confocal microscope compatible with ODMR measurement. A simplified scheme of the apparatus is shown in the section 5.2.1. The opti-

cal excitation power provided by a CW 532-nm laser (Coherent Prometheus 100NE, Relative Intensity Noise <-90 dB/Hz, 2nd harmonics) was <1mW and the acquisition time of all PL measurements was 60 s. These values were chosen as a trade-off between the fast measurement and the precise temperature estimation. We underline that our choice guarantees cell viability (see section 7.2.1).

The experimental procedure for detecting temperature variation using NV centers in NDs was the following. A Petri dish containing cultured hippocampal neurons (10 DIV), previously exposed to NDs, was positioned inside the single-photon confocal microscope incubation chamber. Using the motorized stage, the sample was scanned by incident laser (P < 1 mW, RIN < -90 dB/Hz) in order to select a single ND inside a cell. The ODMR spectrum was acquired for 60 s and the data was post-processed to create the differential graph (see section 4.1.2). Then, the microwave frequency was set in accordance with the minimum of the ODMR spectrum (zero of the differential spectrum). The differential signal of luminescence at this frequency was acquired for 60 s. The microwave field before and after data acquisition was always turned on to avoid possible heating transient processes. In a successive step, solutions containing 100 μM picrotoxin and then 300 nM TTX + 200 μM $CdCl_2$ were added to the medium (where M=mol/L is the molarity). The measurement of the differential signal was repeated at the same resonant frequency as in the previous step. Finally, the ODMR spectrum was reacquired for 400 s, recreating a new differential spectrum in order to improve the statistics and to evaluate the linear region slope with lower uncertainty. The temperature variation ΔT was evaluated through a direct PL change measurement according to equation:

$$\Delta\tilde{F} = slope \cdot \partial D_{gs}/\partial T \cdot \Delta T \tag{7.4}$$

Here $\Delta\tilde{F}$ represents the differential signal variation (difference in the photon counting rates), evaluated at the linear region of the differential spectrum and associated with a temperature variation ΔT. The slope represents the constant of proportionality that connects $\Delta\tilde{F}$ to the resonance frequency shift ΔD_{gs}. Finally, $\partial D_{gs}/\partial T$ represents the coupling constant.

7.3.2 Experimental data

To detect the temperature variations associated with different patterns of neuronal activity, recordings were performed in three conditions (Figure 7.4): (i) in the presence of external Tyrode solution (CTRL), since in this condition the hippocampal network was spontaneously firing [170], (ii) after addition of 100 μM of picrotoxin, a selective GABAA inhibitor, which is known to drastically potentiate the neuronal firing activity [182], (iii) after subsequent addition of 0.3 μM tetrodotoxin (TTX) and 500 μM cadmium chloride (Cd), to inhibit the spontaneous firing.
Bath temperature was kept at 37 °C and the photocounting rate was performed from internalized NDs. With reference to the above conditions, a more detailed account of the three measurements condition follows hereby.
-Condition (i): To exclude that the perfusion system could induce some temperature variations, the photocounting rate from an internalized ND was measured before and after perfusing the cells with Tyrode solution (CTRL, in Figure 7.4d). From the photoluminescence difference , the temperature variation was estimated according to Equation 7.5. In these conditions we revealed an average temperature variation $\Delta T = (0.05 \pm 0.15)$ °C (weighted average evaluated on a sample with a numerosity N = 11), proving that no significant temperature variations are associated with thermal exchanges of the perfusion system.
After this preliminary test, the next step was to assess whether changes in neuronal firing could be associated to temperature variations.
-Condition (ii): ΔT was estimated by comparing before and after perfusing the cells with a picrotoxin-enriched Tyrode solution. The addition of the GABAA inhibitor caused a significant temperature increase, $\Delta T = (1.02 \pm 0.24)$ °C (N=10), associated with the increased firing rate (Figure 7.4a)). As a more quantitative corroboration of our conclusions, a thorough statistical uncertainty analysis was performed (see next section) to confirm that a significant localized temperature variation occurs in a neuron deriving from sustained firing activity ($1.12 \cdot 10^{-8}$ significance in a Welch t-student test).
-Condition (iii): network activity was silenced by means of the Tyrode solution enriched with TTX+Cd. In this case, ΔT was measured by comparing before and after perfusing the cells with picrotoxin +TTX+Cd solution. Un-

der the latter condition, a significant temperature decrease ΔT = (-0.50 ± 0.17) °C (N = 8) was revealed (Figure 7.4d)) with a $2.21 \cdot 10^{-6}$ significance in a Welch t-student test (see section 7.3.3). These data demonstrate that both potentiation and silencing of the neuronal network activity could be assessed by temperature variations and that the hippocampal network, exhibiting basal spontaneous activity, displays higher temperatures than the completely silenced network.

Another set of experiments was carried out for measuring the average temperature variation associated to non-internalized ND before and after perfusing the cells with picrotoxin solution: in this case no significant difference with respect to the control conditions was found: ΔT = (-0.04 ± 0.23) °C (N = 7). This crossover trial excluded that temperature variation can be due to other external factors than the drug-potentiated neuronal activity.

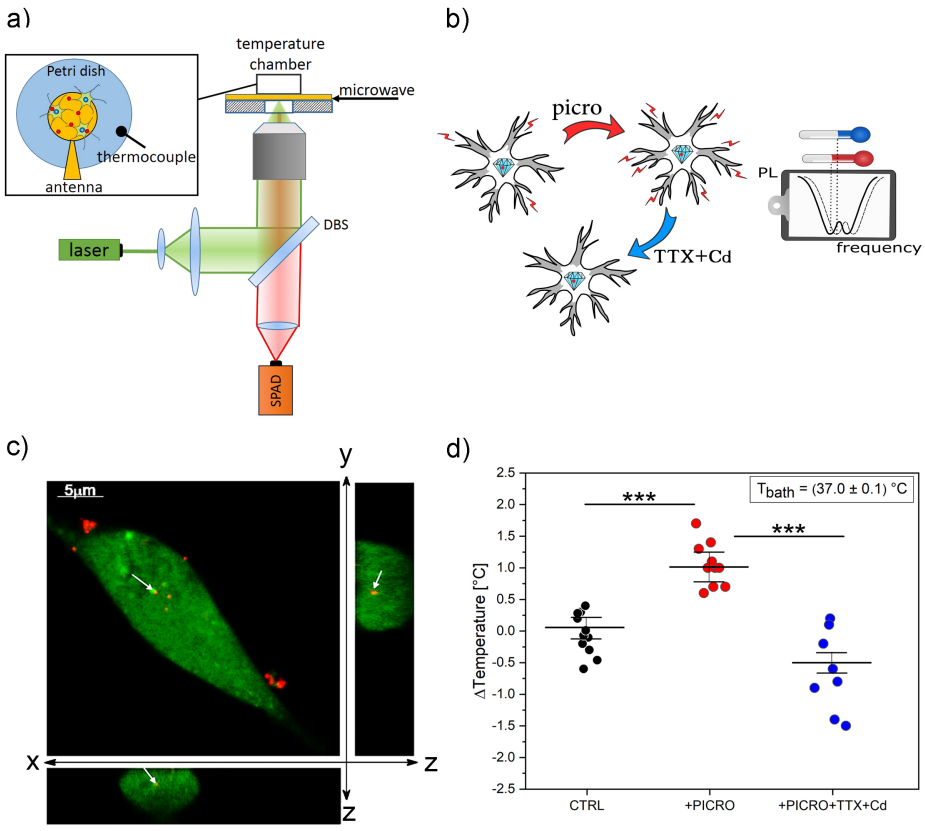

Figure 7.4: Illustration of the experiment. a) Simplified scheme of single-photon confocal ODMR setup b) The ODMR measurements are performed under control conditions (CTRL), after stimulation with picrotoxin and after the addition of TTX+Cd. The frequency shift in the ODMR spectrum (dashed line) is associated with the temperature variation recorded by the ND sensor, c) Confocal fluorescence micrograph of hippocampal neurons incubated with 0.6 µg/ml ND for 5 hours. The cytoplasm is stained in green, the red emission is from NDs. The entire field and cross-sections (XZ and YZ) are shown. White arrows show one internalized ND. d) Boxplot of temperature variations with standard deviations in the presence of saline Tyrode solution (CTRL, black circles), after addition of picrotoxin (PICRO, red circles), after addition of tetrodotoxin and cadmium chloride (TTX+Cd, blue circles), see text for details. Statistical difference is indicated by the asterisks (***, $p<0.0001$)

7.3.3 Statistical Analysis

As detailed in the main text, the experiment was repeated collecting a sample of N = 11 repeated measurements, revealing any temperature rise from a ND inside the cell before and after Tyrode's solution perfusion. In the main test this is referred to as "CTRL". In another sample of N = 10 NDs the

temperature was probed by a ND inside the cell before and after picrotoxin administration. This sample is referred to as "+PICRO". Starting from this condition, a sample of N = 8 temperature variation repeated measurements was performed in a ND inside the cell before and after TTX and cadmium administration. This is referred to as "+PICRO+TTX+Cd". The temperature variation ΔT detected by the NV sensor was evaluated through a direct fluorescence change measurement, as described before, the equation being:

$$\Delta T = \frac{\Delta \tilde{F}}{slope \cdot \partial D_{gs}/\partial T} \tag{7.5}$$

For the uncertainty estimation, the error propagation of the variables that appear in Equation (7.5) has been carried out. In the following, the involved uncertainties are analyzed in detail. The term is the difference between the differential spectrum signal before and after the substance perfusion. The associated uncertainty is the sum in quadrature: $\sigma(\Delta \tilde{F}) = \sqrt{[\sigma(\tilde{F}_{after})]^2 + [\sigma(\tilde{F}_{before})]^2}$. Where $\sigma(\tilde{F})$ is the data standard deviation divided by the square root of repeated measurement (500 values in 60 s).
As well as the PL, the slope was also evaluated on every single measurement. The associated uncertainty $\sigma(slope)$ was evaluated by the linear regression of the linear region differential spectrum. The constant $\partial D_{gs}/\partial T$ was evaluated by a previous measurement, analyzing a sample of N = 6 NDs (Table 7.1) as described in the Section "Estimation of $\partial D_{gs}/\partial T$". Unlike previous contributions, its associated uncertainty acts as a B type uncertainty, intervening only in the errors propagation on the average value estimate of each data set. The values ΔT_i and $\sigma(\Delta T_i)$ are shown in Table 7.2. To prove the main result of this work it was necessary to demonstrate a significant statistical difference between the "+PICRO" and the "CTRL" sets. This can be formalized by evaluating the probability that ΔT_{+PICRO} and ΔT_{CTRL} belong to the same population, which is the starting null hypothesis. The Welch t-student test was performed for this purpose. The calculated values for the stochastic t variable, the population degree of freedom and the probability of satisfying the null hypothesis are shown in Table 7.3. The test significance obtained allowed rejecting the initial null hypothesis. The two samples did not belong to the same population and therefore the increase in temperature, recorded fol-

lowing picrotoxin perfusion, was statistically significant. The same test was repeated to compare the "CTRL" and "+PICRO+TTX+Cd" sets in order to understand if the decrease in temperature recorded by the nanodiamonds following the TTX and Cd perfusion is statistically significant. As can be seen from Table 3, also in this case it is possible to reject the null hypothesis. The two samples did not belong to the same population and therefore the decrease in temperature was statistically significant.

$\Delta T \pm \sigma(\Delta T)$ [°C]		
CTRL	**+PICRO**	**+PICRO+TTX+Cd**
-0.08 ± 0.77	1.39 ± 0.76	0.18 ± 0.80
-0.27 ± 0.49	1.38 ± 1.02	0.14 ± 0.48
-0.17 ± 0.47	1.01 ± 0.90	-0.63 ± 0.29
-0.60 ± 1.23	0.65 ± 0.64	-1.46 ± 0.72
0.33 ± 0.33	1.73 ± 0.85	-0.76 ± 0.60
0.42 ± 0.88	1.04 ± 0.65	-0.92 ± 0.57
0.18 ± 0.59	1.12 ± 1.10	-0.20 ± 0.31
-0.07 ± 0.49	0.70 ± 1.06	-1.50 ± 0.77
0.29 ± 0.33	1.04 ± 0.49	
-0.47 ± 0.55	0.73 ± 0.57	
-0.01 ± 0.44		

Table 7.2: Summary of temperature variation $\Delta T \pm \sigma\Delta T$ [°C] for the three (sample size, respectively, N=11, N=10, N=8) independent groups.

CTRL vs +PICRO	
Welch's t value	11.24
Degree of freedom	14.90
Significance Welch's t-test	$1.12 \cdot 10^{-8}$
+PICRO vs +PICRO+TTX+Cd	
Welch's t value	7.63
Degree of freedom	14.15
Significance Welch's t-test	$2.21 \cdot 10^{-6}$

Table 7.3: Summary of statistical parameters for Welch's t-test.

7.4 Conclusions

Intracellular localized temperature gradients are associated with metabolic activity and with a variety of reactions and intracellular processes [183]. Real-time mapping of intracellular subtle temperature gradients and event-driven increased temperature represents a tool of the utmost interest for monitoring the functional activity of the cells, for identifying localized signaling under physiological conditions and for exploitation as a diagnostic tool.
Here we applied the ODMR technique to cultured hippocampal neurons for monitoring temperature variations in different conditions of network excitability. We provided evidence that a significant temperature increase can be correlated with the altered firing activity of cultured hippocampal neurons, in our case induced by picrotoxin, and that this phenomenon can be successfully observed at the single-cell level exploiting nanosensor based on NDs.
It is worth noting that picrotoxin-induced disinhibition primarily alters cell excitability, but the increased action potential firing activity may in turn alter intracellular pathways: since we cannot predict whether NDs are localized at the plasma membrane or at the intracellular level, the detected temperature increases are indeed induced by picrotoxin but can be associated to membrane-delimited or intracellular processes. Interestingly, a reduction of the network activity is detectable as a $\Delta T = (-0.50 \pm 0.17)$ °C temperature decrease. Another relevant finding is that our method is suitable to distinguish the basal spontaneous firing rate [169, 184, 185, 186] from the condition in which the network activity is completely silenced.
Thus this approach may uncover different degrees of neuronal excitability.
We underline that the possibility of slightly improving the set-up and the measurement technique (which being a first version is not yet completely optimal) can lead to a further enhancement of the sensor sensitivity. In perspective, it is reasonable to foresee more than a one-order of magnitude improvement in sensitivity with respect to the current condition by accounting for three main improvements of the system:
1) implementing orientation tracking of NDs in order to apply transversal bias field scheme as already demonstrated in bulk diamond [187], which al-

lows a factor 3 of scaling in the temperature sensitivity in EM-insensitive condition;
2) particle tracking would also allow for longer measurement time, for instance an increase of the measurement time of a factor 10 would result in another factor 3 scaling in sensitivity;
3) obtaining samples of NDs with an increased number of NV centers would result (below saturation threshold) in a further improvement of sensitivity (also in this case, an increase of a factor 10 in the interrogated centers would result in a factor 3 improvement in the sensitivity).
Finally, together with the above mentioned upgrades, improving the ND fabrication, resulting in increased coherence, would allow further improvement of the sensitivity, realistically rendering the system in perspective sensitive to < 0.1 °C variations. We underline that these nanosensors, carefully prepared and selected, are able to provide a fast temperature measurement with extraordinary spatial resolution, in perspective even below the diffraction limit [188].
The action potential generation and propagation is not the unique energy-requiring process involved in neuronal activity, as this may also involve maintenance of the membrane resting potential, neurotransmitter release and uptake, vesicular recycling and presynaptic Ca^{2+} currents [189]. The firing activity is correlated with the total energy consumed by neuronal activity. This has been calculated from anatomic and physiological data [183] and experimentally verified using fMRI techniques [190]. Thus, our results prompts further studies to assess whether the observed temperature increase during perfusion with picrotoxin is ascribed to sustained firing activity and/or potentiated cell metabolism [181].
By means of confocal microscopy observation, we demonstrate that 5 hours exposure to ND is enough to promote ND internalization and that action potential waveform remains unaffected after laser and microwave irradiation, confirming that the applied protocol for sensing temperature preserves cell excitability and ion channel functioning [169] (with perspectives for "in vivo" studies).
The measured temperature increases can be used to reveal the onset of different intracellular processes other than membrane-delimited pathways, likely

involving an altered cell metabolism as here was demonstrated with picrotoxin. Thus, our future goals will be devoted to functionalizing NDs to sub-cellular compartments, to detect thermogenesis at specific sub-cellular sites. These results, backed by a thorough analysis of other possible alternative causes of temperature variation, pave the way to a systematic study of cell activity with impacts ranging from a better insight on current unknowns associated with cells functioning, such as e.g. the aforementioned discrepancy between experimental data and thermal diffusion models, to the research on specific pathologies.

Our findings also prompt further applications where ongoing advances in microelectrode array technology (MEA), combined with quantum sensing paves the way for experiments that take advantage from the synergy of the two techniques, such as synchronized measurements of cellular activity with metabolism processes or propagation of electromagnetic signals.

Chapter 8

Bulk diamonds sensors experimental results: sensitivity improvements for biological applications in perspective

This chapter analyzes the experiments carried out on bulk diamond. Unlike nanodiamonds, macroscopic diamond obviously cannot diffuse across the cell membrane due to their size. Remaining outside the cell, not only are the detectable biological signals weaker, but also the spatial resolution is degraded (which for nanodiamonds is linked to the size of the latter). However, these disadvantages can be countered by more sophisticated fabrication techniques that allow for higher crystal quality and more refined ODMR measurement.

8.1 Technique for improve ODMR sensitivity in biological perspective

In this section some technological solutions to improve the NV-based sensors sensitivity are discussed as well as the precautions to be taken when they are used as a bio-sensor.
Equation (6.2) provides the ultimate sensitivity limit reachable highlighting that the number n of NV centers and their decoherence time T_2^* play a key role. To increase n, while maintaining the same spatial resolution, it is necessary to have diamonds with an increased NV centers density. This can be achieved by enhancing the number of nitrogen implanted in the diamond and improving the N-to-NV conversion efficiency, minimizing the concentration

of residual paramagnetic substitutional nitrogen [71]. In parallel, to increase T_2^*, it is also recommended the production of ultra-pure diamonds, with reduced unwanted electronic impurities (e.g. the P1 centers) and nuclear spins impurities (e.g. the paramagnetic ^{13}C isotopes, whose natural abundance is about 1.1%) [191, 192, 193]. It is important to note that the NV density increase will necessarily worsen the decoherence time of the NVs themselves, because of their mutual interaction. Consequently, an optimal trade-off between these parameters must be sought.

In addition to the NV-density and diamond engineering, the sensitivity can be improved by implementing specific experimental techniques, that are based on suitably synchronized laser and microwave pulses of particular duration [112, 194, 86].
For example, if an unknown electromagnetic field, responsible for the ODMR resonance frequency shift, is constant or slowly varying, it is possible to adopt the experimental *pulsed* ODMR protocols [195] or the *Ramsey* method [68] instead of the continuous wave (CW) ODMR [196].
The CW ODMR is the simplest and most widely employed magnetometry method with NV-based sensors, wherein the microwave driving and the optical polarization and readout (laser pumping) occur simultaneously (see section 4.1.1). Although this technique is easy to be implemented, the relative ODMR spectrum dips are affected by the broadening induced by the continuous exposure of the laser beam and microwave field on the sample.
With *pulsed* ODMR techniques this broadening effect is substantially suppressed, allowing to obtain narrower ODMR spectrum dips and therefore to improve the measurement sensitivity (see section 8.2.1). This protocol uses temporally separated optical laser initializations, π microwave control pulses, and laser readout pulses. The π pulses is an oscillating microwave field applied for a duration such as the electronic state passes from the $|m_s = 0>$ state to $|m_s = \pm 1>$. The name derives from its representation of the process on the *Bloch* sphere.
Ramsey ODMR spectroscopy, on the other hand, consists on in the application of two $\pi/2$ pulses, separated by a time τ. Also the $\pi/2$ pulse is an oscillating microwave field that brings the electronic state from the state

$|m_s = 0>$ to a superposition of $|m_s = +1>$ and $|m_s = -1>$. By varying the time τ, the so-called "Ramsey fringes" are obtained, from which it is possible to extrapolate an estimation of the magnetic fields amplitude. Also this technique allows sensitivity improvement with respect to the *CW*: the decoupling of the MW from the laser power allows increasing the MW power while improving the contrast, without degrading the FWHM of the spectral dip.

In the case of time-varying electromagnetic fields, there are other even more complex microwave pulse sequences, capable of decoupling the measurement from surrounding spin environment [197]. In this way the decoherence time of the NV centers increases and consequently it becomes possible to interrogate the quantum system for longer times, improving the measurement statistic and therefore the sensitivity.

One of these experimental protocols is the *Hahn Echo* sequence [198, 199], which refocuses the dephasing NVs spin, applying an additional π pulse in the middle of *Ramsey* sequence. The characteristic time of the spin coherence decay, measured with this protocol, is called T_2 and it is typically one or two orders of magnitude longer than T_2^*.

Even more complex dynamic decoupling sequences, which apply multiple refocusing π pulses further improving the decoherence time T_2 have been devised [200, 201, 202, 203]. Among these, the most famous are the *Carr-Purcell-Meiboom-Gill* (CPMG) [200, 201, 202, 203] and the *XY8* sequences [200, 204], which differ in the spin rotation axes: the first method applies the pulses along the same axis, while the second chooses a different one for each π pulses.

It is useful to underline that, although these techniques allow to extend the coherence time of the NV centers, this time cannot be reduced beyond the spin-lattice relaxation time T_1, that for an NV spin ensemble in bulk diamond is about 3 ms [205].

The Figure 8.1 briefly summarizes the above mentioned pulse sequences. It is useful to underline that the sensitivity formula in Equation (6.2) describes an idealized measurement with a perfect readout mechanism. On the contrary, typically the readout mechanism adds noise in the measurement, that can be described by introducing, in the previous equation, the spin-readout fidelity

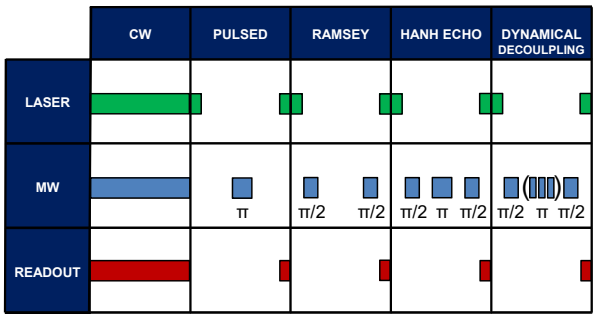

Figure 8.1: Scheme of timing and duration of laser pulses, microwave pulses and reading sequences associated with the most common measurement protocols of the external fields for the NV complex.

factor $\mathcal{F}$ [86]:

$$\eta = \frac{1}{\gamma_e \sqrt{nT_2^*}} \frac{1}{\mathcal{F}} \tag{8.1}$$

Keeping the usual optical-readout, but improving the photon collection is expected to increase $\mathcal{F}$ (see ref.[206] for different methods to improve photon collection). Ancilla-assisted repetitive readout, which is based on mapping the NV spin state to the nuclear spin state, also improves $\mathcal{F}$ [86]. Finally, in a further perspective, quantum methods of noise reduction can be applied [207, 208, 209, 210].

When the ultimate goal is bio-sensing, some constraints rise limiting the implementation of the above described pulse sequences. One constraint is the frequency bandwidth. In fact, the above-mentioned dynamic decoupling techniques are capable of measuring time-varying external fields only if this time variation is of the order of the time interval separating the π pulses. Furthermore, in order to control the system quantum state, the time between these pulses cannot exceed the coherence of the NV center. Consequently, the frequency of the signal to be measured must be of the order of the coherence time of the NV centers. In the biological case, the electromagnetic fields pulse lasts about 1 ms. This value is very far from T_2, marking a

boundary for the use of these techniques in biological applications. Another constraint is associated to the optical laser power. The higher the laser power the better the sensitivity in measurements with ensembles, since it increases the percentage of excited centers and consequently the fluorescence signal. However precautions must be taken to avoid cells and proteins damaging. An efficient solution can be to direct the laser beam towards the diamond at an angle allowing total reflection (*Brewster* angle). In this way only the fluorescence emitted by the NV centers travels through the cells, placed on the other diamond surface [113, 84]. In this case, however, precise control over sensing volume would be lost, deteriorating spatial resolution. In a standard configuration, where the laser impinges perpendicularly on the sample, it is necessary to limit the optical power reaching the cells to few mW.
In the next sections some sensitivity improvement techniques are presented for use in a biological perspective.

8.1.1 CW ODMR in the simultaneous hyperfine driving

This section presents an innovative experimental set-up to measure magnetic fields utilizing a lock-in based ODMR technique for the optical detection of microwave-driven spin resonances induced in NV centers. This method is characterized by the excellent magnetic sensitivity at such small scale and the full biocompatibility. The cellular scale is obtained using a NV-rich sensing layer of 15 nm thickness along z axis and a focused laser spot of (10×10) μm^2 in x-y plane oh the bulk diamond (see section 8.2). The biocompatibility derives from an accurate choice of the applied optical power. It is also reported how the magnetic sensitivity changes for different applied laser power and discussed the limits of the sensitivity sustainable with bio-system at such small volume scale.

The simplest way to track the ODMR shift is to collect the photoluminscence signal while scanning the microwave frequency. Adopting a frequency modulation of the microwaves can improve this method: the modulating signal is centered at the resonance dip and has an amplitude equal to the full-width half maximum (FWHM) of the resonance dip [113, 136]. The resulting modulated photoluminescence signal is read by a lock-in amplifier (LIA), see

Figure 8.2a). The resulting LIA signal is a linear function of ODMR shift. This technique has also the advantage to shift the spectrum of the signal in a region where the technical noise is lower (see section 4.1.3).

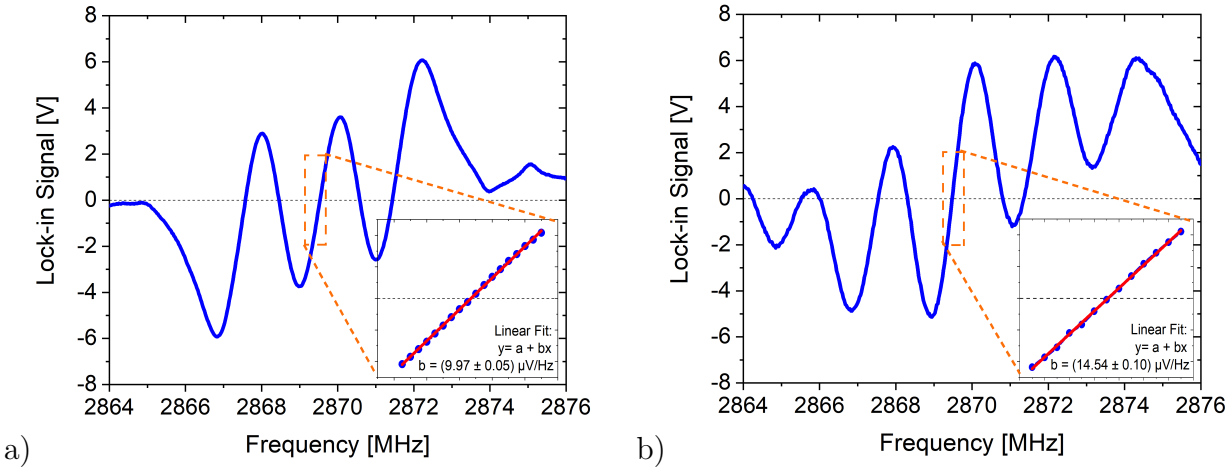

Figure 8.2: Lock-in spectrum with excitation of a single resonance a) and simultaneous excitation of the three resonances separated by the hyperfine coupling b). The insets shows the central linear zone and the value b of the slope the curve, that represents the figure of merit of the curve. The simultaneous excitation of the three resonances results in an improvement of b of a factor ~ 1.5 ($b = 9.97\mu V/Hz$ in the case of single resonance excitation and $b = 14.54\mu V/Hz$ in the case of three resonance excitation).

Figure 8.2a) depicts the LIA signal in function of the microwave frequency. Three frequency ranges can be identified over which the LIA signal is directly proportional to the resonance shift and hence to the applied field. A yellow dashed rectangle encloses the central one. These three zones correspond to the three dips in the ODMR spectrum due to the hyperfine coupling of the NV electronic system with the ^{14}N nuclear spin. The LIA signal is linear in these zones because the LIA detection method is sensitive to the first derivative of the ODMR spectrum. The figure of merit of the LIA detection method is represented by the slope b of the curve in the linear zone, as reported in Figure 8.2. In this zone, δB is related to the measured LIA signal S_{LIA} by [113]:

$$\delta B = \frac{1}{\gamma_e}\frac{1}{b}S_{LIA} \tag{8.2}$$

Where γ_e is the magnetic field coupling constant. It is possible to increase

the slope of the curve (and thus the sensitivity of the technique) by simultaneously addressing all the three resonances [113, 211]. To this scope, three frequency- modulated microwave tones separated by the hyperfine splitting $A_\perp = 2.16$ MHz were generated. When the center tone is at the frequency of the center resonance, all three resonance are excited, thus enhancing the slope of the curve. Figure 8.2b) shows an example of the LIA spectrum for multiple frequency excitation. b is increased by a factor ≈ 1.5 compared to single-resonance excitation. The minimum detectable magnetic field B_{min} is:

$$B_{min} = \frac{1}{\gamma_e}\frac{1}{b}\frac{\sigma_S}{\sqrt{N}} \tag{8.3}$$

where we have considered N independent measurements and that S_{LIA} is affected by an uncertainty equals to σ_S. Increasing the total time of measurement T leads to the usual scaling of the sensitivity η:

$$\eta = B_{min}\sqrt{T} = \frac{1}{\gamma_e}\frac{1}{b}\frac{\sigma_S}{\sqrt{N}}\sqrt{T} \tag{8.4}$$

Figure 8.3 shows the Linear Spectral Density of the LIA noise multiplied by the factor $\frac{1}{\gamma_e b}$ as defined in Eq. (8.3). For the Lock-in detection scheme described in this work, η corresponds to the low-frequency plateau in Figure 8.4. This figure also shows the shot-noise limit for the single hyperfine driving, the Continuos Wave (CW) shot-noise limit being:

$$\eta_{CW} = \frac{1}{\gamma_e}\frac{\sqrt{I_0}}{max(\frac{\partial I_0}{\partial \nu})} \tag{8.5}$$

where I_0 is the photons intensity and $max(\frac{\partial I_0}{\partial \nu})$ is the maximum slope in the ODMR graph. As results from ODMR spectrum:

$$\eta_{CW} = K\frac{1}{\gamma_e}\frac{\Delta\nu}{2\sqrt{I_0}C} = 12.5\, nT/\sqrt{Hz} \tag{8.6}$$

where $\Delta\nu = 1.072$ MHz is the ODMR linewidth, C = 0.00273 the contrast for the central dip of the hyperfine spectrum and K depends on the type of characteristic function of the spectrum, in case the ODMR spectrum can be interpolated with a Lorentzian function, the constant is 0.31. $I_0 = 3.03 \cdot 10^{10}\, s^{-1}$ is estimated from the optical power incident onto the photodiode W

$= 8.5$ nW, considering a photon energy $E_{ph} = 2.84 \cdot 10^{-19}$ J.
Figure 8.3 shows that simultaneous driving improves the sensitivity by a factor of ≈ 1.5 according to red and black lines.. This improvement is due to two contributions: (i) an increase in the slope b (ii) no significant increase in the LIA noise.

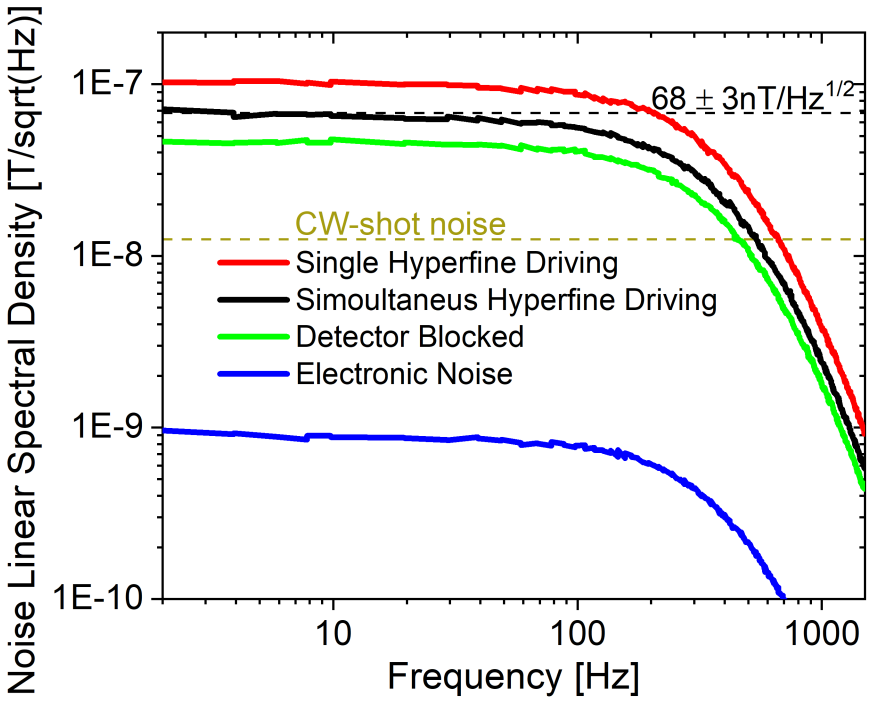

Figure 8.3: Comparison between the linear spectral densities (LSD) of the readout of the NV sensor in single hyperfine driving regime (red line) and in the simultaneous hyperfine driving (black line). The linear spectral density of the read-out with the detector blocked(green line), with the input of the LIA disconnected (blue line) and the Continous Wave(CW)-shot noise (dark green dashed line) are also shown. The value of the low-frequency plateau gives the magnetic sensitivity of the measurement. The simultaneous hyperfine driving improvement the sensitivity of a factor ≈ 1.5

To point out the biocompatibility of this method, we measured the magnetic sensitivity for different applied powers, see Fig. 8.4. The sensitivity decreases by lowering the laser power. It is important to underline that

we obtained a sensitivity of $\eta = 68 \pm 3\, nT/\sqrt{Hz}$ for an optical power of 80 mW: this value is beyond (or at least well comparable) with the one obtained in previous works when the sensing volume is taken into account [113, 133, 212, 213], see Figure 8.5.

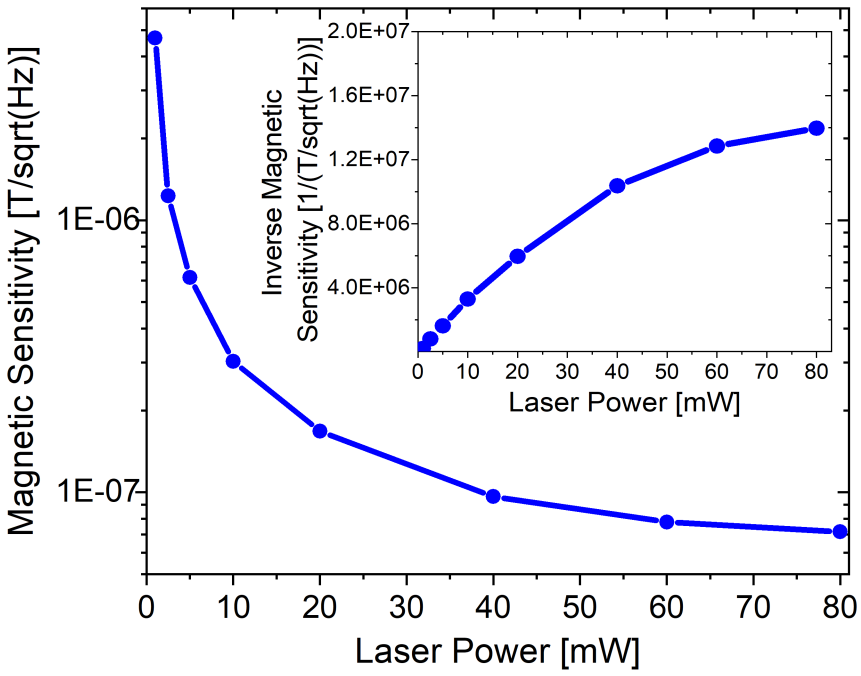

Figure 8.4: Magnetic sensitivity for different values of the applied optical power. In the inset, the inverse of the sensitivity is shown for the same power values. Uncertainties are too small for being visible. The magnetic sensitivity improves increasing the applied optical power

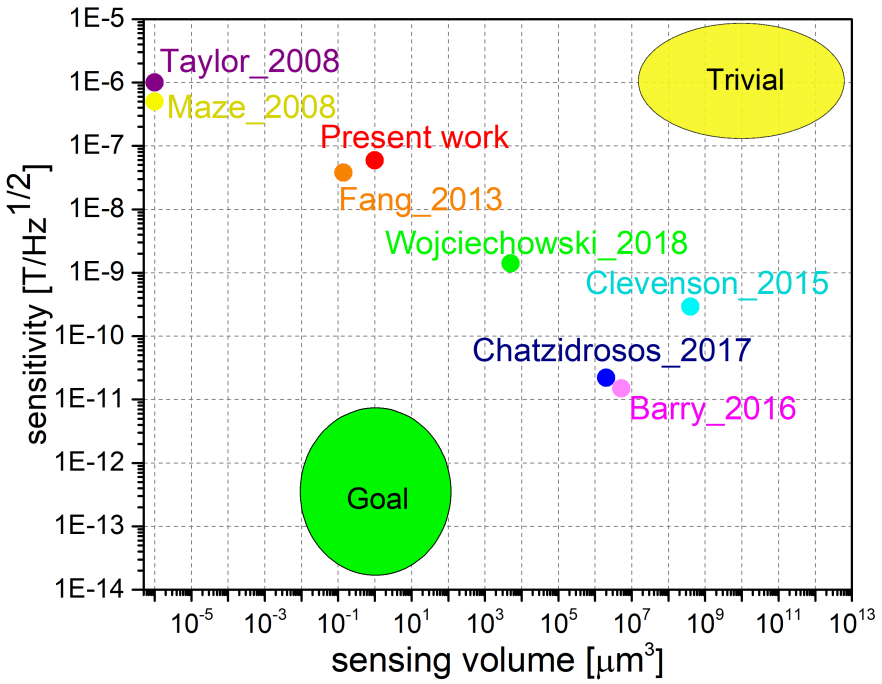

Figure 8.5: The sensitivity in function of the sensing volume for the present study and from data taken from literature [NV [68], ND 2008 [70], Fang 2013 [214], Barry 2016 [113], Wojciechowski 2018 [215], Clevenson 2015 [213], Chatzidrosos 2017 [213]. The region of interest for biological application is defined by the green region

It is not proved that living cells can sustain 80 mW of power radiating on a surface of 100 μm^2, even considering that we apply this power only for a measurement time of 10 ms in a measurement cycle of 1 s. On the other hand, living neuronal cells can surely tolerate without being affected an optical power of 3 mW applied for minutes in the same optical geometry and similar applied microwave powers of our setup [169]. Considering that we apply the optical power only for few milliseconds, we can estimate a conservative biocompatible optical power $\gtrsim$ 10 mW, that results in a sensitivity around $\eta_{bio} \lesssim 200\, nT/\sqrt{Hz}$.
This magnetometric sensitivity value still needs to be increased to sense neuron (or hearth cells) activity, where we expect a magnetic field of 1-10 nT in proximity of a single ionic channel (a functionalised nanodiamond can

in principle be targeted at nanometric distance from the channel) or when considering tissue slices. Furthermore, ion channels clustering can further increase the previous values.
In order to achieve accurate magnetic sensing from biological samples at the (sub-)cellular scale, we envisage the following improvements as necessary: (i) use of pulsed techniques (ii) use of isotopically-purified diamonds (iii) protection of the sample from the laser heating.

8.1.2 Pulsed ODMR

As described in section 8.1.1, the CW ODMR suffers from MW and optical power broadening, degrading contrast C and linewidth FWHM of the resonance dip. In order to mitigate this power broadening, a pulsed ODMR protocol uses a temporally separated laser initialization, a MW control π pulse, and a laser readout pulse as demonstrated in Figure 8.6a)-c). This leads to the decrease of the linewidths as shown in Figure 8.6b) with respect to CW ODMR. Alteration of the MW power changes the duration of a π pulse, and must be optimized to balance linewidth and contrast of ODMR resonance features.

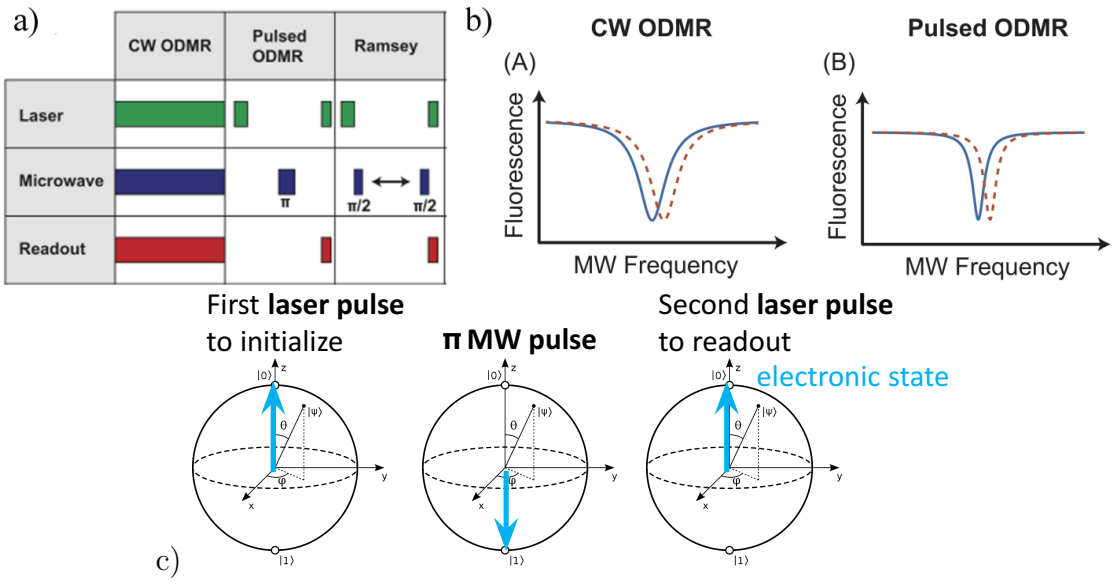

Figure 8.6: a) NV Measurement Protocols. Schematic of timing and duration of laser pulses, MW pulses, and readout sequences relative to the field being sensed for common NV diamond protocols. b) ODMR Protocols. (A) Example CW ODMR lineshape before (blue) and after (red) a resonance frequency shift. (B) Example pulsed ODMR lineshape before (blue) and after (red) a resonance frequency shift. c)Pulsed ODMR representation in the Bloch sphere.

As mentioned in section 8.1, the CW-ODMR schemes is more technically convenient for the low frequency fields (<1 kHz) or spatial field variations over macroscopic areas because avoids the difficulty facing pulsed schemes. The efficiency in this case is based on how large a change in fluorescence can be generated and how small a change can be detected, for incremental resonance shifts induced by an external magnetic/electric field of a temperature variation. The challenge is thus generating the narrowest spectral linewidth during cw-driving while ensuring that the fluorescence contrast is as high as possible. Figure 8.7 shows the effectiveness of applying the pulsed technique compared to the CW technique. The employed bulk diamond is described in section 8.2.

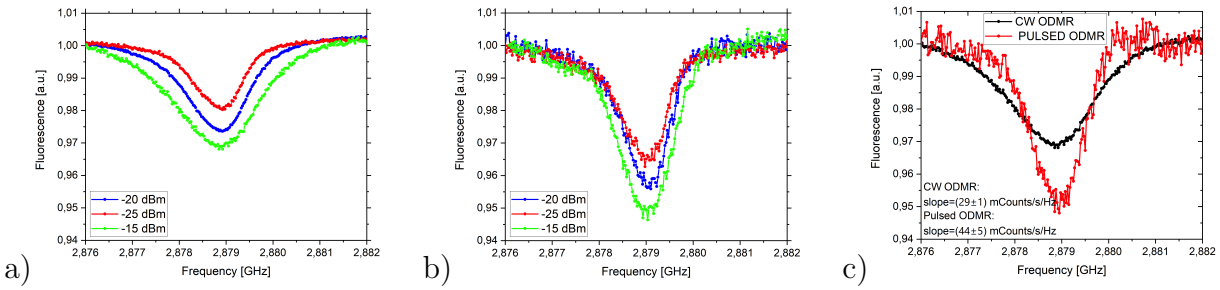

Figure 8.7: a) ODMR graphs with three different microwave powers. b) Pulsed ODMR graphs at different microwave powers. c) Comparison between the ODMR graph and the Pulsed ODMR graph at the same microwave power: -15 dBm.

8.1.3 CW ODMR with orthogonal external magnetic field application

Another method to improve the sensitivity, while maintaining the CW ODMR technique for biological temperature measurements in perspective, consists in the application of an intermediate transverse bias magnetic field $B^{\perp}$ [216]. The application of $B^{\perp}$ removes the degeneration of $|m_s = \pm 1>$ and therefore improves the FWHM. The intensity and the transverse direction of that field creates a quantum superposition of states, which is insensitive to magnetic fields but sensitive to temperature [216]. In this configuration, the expectation value of the spin along any direction is small, implying the degeneracy of the hyperfine structure between the levels $|m_I = \pm 1>$ (except for the quadrupole contribution Q_{gs}, which seperates $|m_I = 0>$ from $|m_I = \pm 1>$). In Figure 8.8 the corresponding scheme of the spin energy levels is reported (only the ^{14}N isotope is considered as it is the most common). In this situation, the ODMR spectrum reduces to two dips [216] (instead of 6), providing a substantial improvement in the signal-to-noise ratio. This particular orientation of the magnetic field ensures the protection of the measurements from the noise of other possible magnetic fields. In fact, the NV spin is non-sensitive to the magnetic field fluctuation, because the contribution of the magnetic component only appears at the second order in the Hamiltonian. In this regard, Figure 8.9 shows a sensitivity curve versus the laser optical power. The application of a transverse bias magnetic field $B^{\perp}_{bias} \simeq 3\ mT$, allows to improve the sensitivity of the NV-center-based thermo-sensor with

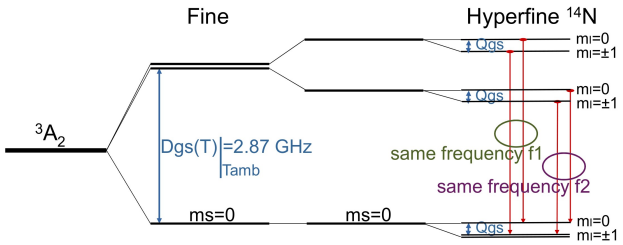

Figure 8.8: NV ground-state $^3A_2$ scheme, in presence of intense transverse magnetic field $B^{\perp}$.

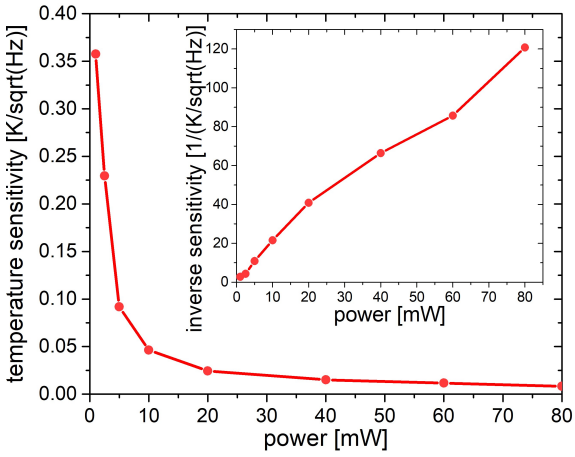

Figure 8.9: Temperature sensitivity versus the laser excitation power at 532 nm. The inset shows the inverse of the thermal sensitivity versus the excitation laser power.

respect to other standard techniques in CW regime. The temperature sensitivity reached at laser power of 80 mW is $\eta \simeq 8\ mK/Hz^{1/2}$ in a sensing volume of 1 μm^3, but this excitation power can present biocompatibility problems. However, the sensitivity obtained is even beyond the one required to monitor biological mechanisms, that is typically of the order of 1 °C. Figure 8.9 shows that it is possible to perform the temperature measurement with a lower laser power, finding an ideal compromise between the temperature sensitivity and laser intensity impinging on the cell sample. Indeed, with a power of a few mW it is already possible to discriminate biological processes with a sensitivity of the order of a tenth of a degree.

8.2 Diamond

To improve the sensitivity for the measurement of external fields, it is convenient to interrogate several NV centers simultaneously, in a small volume to preserve the spatial resolution. However, it is not enough to have a sample with an high number of active centers: they must be in a crystal lattice as pure as possible in order to avoid to be affected by the electromagnetic fields generated by impurities.
The pristine sample was a 3×3×0.3 mm^3 diamond substrate produced by ElementSix by CVD deposition and processed by the Solid State Physics group of the University of Turin. The sample was classified as an "optical grade" CDV diamond for having the nominal concentration of substitutional nitrogen and boron of <1 ppm and 0.05 ppm, respectively. The sample was implanted with 10 keV N ions at room temperature using a low energy ion implanter. Implanted N ions fluence (dose) was $1{\cdot}10^{14}$ cm^{-2}. Implanted sample was subsequently annealed for 2 hours at temperature of 950 °C. This process resulted in the formation of NV centers with a $\sim 3 \cdot 10^{19}\, cm^{-3}$ concentration across a ∼15 nm thick layer at ∼10 nm from the sample surface.

8.3 Conclusion

Magnetometry in biological systems is of the utmost importance for fundamental biological science and medicine [12]. Mapping brain activity by recording magnetic fields produced by the electrical currents which are naturally occurring in the brain is of extreme interest [217, 218], with direct applications in the timely detection and cure of psychic and neurodegenerative disorders [219, 220, 123]. Measuring the magnetic fields produced by electrical currents in the heart is also of the utmost importance [221], since this could lead to a new generation of non-invasive diagnostic and therapeutic techniques [222]. Despite the substantial interest in these research areas, the theoretical sensitivity needed to detect these very weak biological magnetic fields is still very far from that achieved experimentally. In this chapter some improvements that can be performed in bulk diamonds are discussed which concern both the sensing technique and the optimization of the diamond crystal growth. These results suggest a strategy for magnetic sensing at cellular

level, contributing to paving the way to practical biological applications of these methods.
Finally, the sensitivity obtainable with bulk diamond ideal for measuring temperature variations is presented in section 8.1.3. Although bulk diamond does not allow a spatial resolution comparable to nanodiamonds, the high improvement in sensitivity arouses great interest in its application. A further obstacle can be traced back to the high thermal conductivity of the diamond, which is between 1000 and 2600 $W/m \cdot K$. Consequently, a thermal increase localized in a few micrometres (for example in the case of a single cell) would be quickly compensated for due to the rapid thermalization of the diamond. These problems can be overcome by designing an experimental set up (gradiometer) capable of performing the measurement simultaneously in two points of the bulk diamond. Thanks to the good thermal sensitivity, a quick measurement of the thermal gradient could be possible.

Summary

This thesis was focused on the theoretical study and the practical implementation of the possible applications of nitrogen-vacancy (NV) color centers in diamonds. The above studies show the enormous potential of lattice defects not only as robust single photon sources, but also as highly sensitive nanoscale sensors operating under ambient conditions for quantum metrology and bio-sensing applications.
In the chapter 1 the characteristics of the diamond were stated and the subject of study was introduced, that is the NV center with its main properties. In the chapter 2 and 3 the results obtained on single photon emitters were reported. In chapter 2, after having stated the requirements to create ideal single photon sources and their main fields of applications that would benefit enormously, two mathematical functions have been introduced that allow to identify sources of this type. The former is the generalized Glauber's K^{th}-order correlation function $g^{(K)}$, while the latter is a recently proposed anti-correlation function (dubbed $\theta(K)$). In chapter 3 the experimental proof is described which highlights how the use of the theta parameters allow a more precise reconstruction of the modes, especially in the presence of SPSs with thermal and Poissonian fields, where the Glauber function alone fails. The experimental results presented here are collected in the article [223], where my work concerned the theoretical study of multimodal reconstruction and the practical experimental realization. Instead, the beginning of this chapter 3 is devoted to the purely theoretical study of the statistical distribution of photons emitted by an SPS when exposed to a continuous laser and measured for a macroscopic time T (greater than the $lifetime$ in the excited state of the source). As can be seen from the calculations and simulations, when the excitation rate and the emission rate are comparable, the number of photons emitted is described by a sub-Poissonian statistic, the same obtained when

the measurement times are lower than lifetime (and thus exposing the pulsed laser source). Again, the data presented here was collected to create an article, which however is still being written.
Chapter 4 details the spin properties of the negatively charged nitrogen-vacancy complex (NV^-), which make its energy levels sensitive to electromagnetic fields and temperature variations. The sensing techniques and some variants that allow a fast and biocompatible measurement are also explained in detail, in particular the differential ODMR technique introduced specifically for the experiments described in chapter 7 is described.
Chapter 5 analyzes the experimental apparatus I set up to conduct the experiments, both by illustrating its theoretical operating principles and by listing the various instruments I used.
Chapter 6 moves the description to biological applications by overviewing the characteristics of the NV^- center that make it a perfect sensor in the biological field compared to other state-of-the-art candidates. It also theoretically analyzes the theoretical fields generated by neurons or cardiac cells. The considerations reported in these sections are the result of a study carried out by me, which led to the realization of the review [12].
Chapter 7 presents the most relevant result of this thesis, which led to the article publication reported in ref.[179], in which I followed all the experimental part. The experiment consists in the first measurement of thermal variations at the sub-cellular level. The experiment was conducted by incubating the nanodiamond sensors inside the mouse cerebral cortex neurons and the temperature variation was performed following the substances perfusion that alter the firing and the metabolism.
Finally, chapter 8 presents the NV-based-sensing experiments realized with bulk diamonds, some of these are in our articles, reported in refs.[12, 224]. These sensors give more possibilities for engineering, both in the diamond production and in the sensing technique. An appropriate ODMR sequence allows to considerably improve the sensitivity of the measurements. In this chapter some results on technical improvements are compared, always adopting a biocompatible measurement process.

In perspective, it is planned to adopt these pulsed measurement techniques,

more easily applicable to bulk diamonds, to perform cell thermometry measurements with improved sensitivity. This would allow to reveal more imperceptible thermal variations and in perspective it would guarantee a thermal detection linked to substances that alter metabolism and firing in a less drastic way than those used in chapter 7. The loss of spatial resolution due to the high conductivity of the diamond could be restored using a gradiometer measurement, thus simultaneously detecting the temperature from two distinct diamond positions (one measurement exactly under the cell body, the second by interrogating a region of the diamond away from the analyzed cell). At the same time it is planned to develop the experimental improvements described in chapter 8 also for nanodiamonds. The problems that must be overcome are the imperfect immobility of the nanodiamonds and their rotation. For the first problem, we are working on the nanodiamonds functionalization which, in this way, would remain more fixed to the selected target, allowing longer measurements over time and therefore applications of more advanced ODMR measurement protocols. As for their rotation, a Helmoltz coil system has already been purchased which would allow a precise and fast application of a desired bias field in order to cause the degeneration of hyperfine levels and improve the contrast and FWHM of the ODMR spectrum and hence the sensitivity.

The successfully performed ODMR measurements demonstrate the feasibility of cellular sensing measurements without altering its physiological functions and these just mentioned improvements will lead to highly sensitive of temperature and, in perspective, of electrical biocurrents measurements.

Acknowledgments

The work presented in this thesis would have not been possible without the constant support of my colleagues. Here I would like to acknowledge the whole Quantum Optics Group of the National Institute of Metrological Research (INRiM): during the years spent working together I had the chance to learn a lot, also thanks to the many challenges faced.
I want to thank Dott. Ivo Pietro Degiovanni and Prof. Paolo Olivero, my supervisor, for giving me this amazing opportunity to work under his direction on this topic. Last but not least, for the correction of the drafts of this manuscript. A special thanks goes to Dr. Marco Genovese, head of our Quantum Optics Group, Dr. Ekaterina Moreva, Dr. Paolo Traina and Dr. Ettore Bernardi for all the valuable discussions, ideas and a great work environment.
Many other people supported me and I am grateful to all of them, in particular:
Expert help of collaborators Prof. Valentina Carabelli, Dott. Giulia Tomagra, Prof. Marco Marcantoni and Dott. Claudio Franchino who, in addition to providing us with cell samples, have continuously supported me for the measurements in the biological field.
Klaudia Kvakova and Peter Cigler, from the Institute of Organic Chemistry and Biochemistry of the Czech Academy of Sciences, for the nanodiamond samples they provided to me.
Solid State Physics group of the University of Turin coordinated by Prof. Paolo Olivero for the bulk diamond samples.
My family and my boyfriend, for always being at my side and supporting me in everything I do.

Appendix A

Supplementary Material of Section 3.2

A.1 Probability generating function

This section explains the mathematical passages by which it is possible to obtain the expression of $G(t,\xi)$ reported in Eq.(3.13) starting from its definition. Remember that $P_t(n) = K_n(t) - K_{n+1}(t)$.

$$\begin{aligned} G(t,\xi) &= \sum_{n=0}^{\infty} P_t(n)\,\xi^n = \sum_{n=0}^{\infty} [K_n(t) - K_{n+1}(t)]\,\xi^n \\ &= K_0(t) + \xi \sum_{n=1}^{\infty} K_n(t)\,\xi^{n-1} - \sum_{n=0}^{\infty} K_{n+1}(t)\,\xi^n \\ &= K_0(t) + \xi \sum_{m=0}^{\infty} K_{m+1}(t)\,\xi^m - \sum_{m=0}^{\infty} K_{m+1}(t)\,\xi^m \\ &= 1 + \sum_{m=0}^{\infty} K_{m+1}(t)(\xi-1)\,\xi^m = 1 + \sum_{n=1}^{\infty} K_n(t)(\xi-1)\,\xi^{n-1} \end{aligned}$$

In the second line of the proof, the fact was exploited that $G(t,1) = K_0(t)$ and that, by definition, $G(t,1) = \sum_{n=0}^{\infty} P_t(n) = 1$.

A.2 Properties of the probability generating function

In this section the properties of the probability generating function are obtained. For each proof, the starting point is always the definition of $G(t,\xi)$.

Proof of the property reported in Eq.(3.14):

$$\begin{aligned}\frac{1}{n\,!}\,\frac{\partial^n}{\partial\xi^n}G(t,\xi)\,\Big|_{\xi=0} &= \frac{1}{n\,!}\,\frac{\partial^n}{\partial\xi^n}\Big[\sum_{m=0}^{\infty}P_t(m)\,\xi^m\Big]_{\xi=0}\\ &= \frac{1}{n\,!}\,\sum_{m=0}^{\infty}P_t(m)\,\Big[\theta(m-n)\frac{m\,!}{(m-n)\,!}\xi^{m-n}\Big]_{\xi=0}\\ &= \sum_{m=0}^{\infty}P_t(m)\,\delta_{m,n} = P_t(n)\end{aligned}$$

Proof of the property reported in Eq.(3.15):

$$\frac{\partial}{\partial\xi}G(t,\xi)\,\Big|_{\xi=1} = \frac{\partial}{\partial\xi}\Big[\sum_{n=0}^{\infty}P_t(n)\,\xi^n\Big]_{\xi=1} = \sum_{n=0}^{\infty}P_t(n)\,n\,\xi^{n-1}\Big|_{\xi=1} = \sum_{n=0}^{\infty}n\,P_t(n) = \big\langle n\big\rangle$$

Proof of the property reported in Eq.(3.16):

$$\begin{aligned}\frac{\partial^2}{\partial\xi^{\,2}}G(t,\xi)\,\Big|_{\xi=1} &= \frac{\partial^2}{\partial\xi^{\,2}}\Big[\sum_{n=0}^{\infty}P_t(n)\,\xi^n\Big]_{\xi=1} = \sum_{n=0}^{\infty}P_t(n)\,n\,(n-1)\,\xi^{n-2}\Big|_{\xi=1}\\ &= \sum_{n=0}^{\infty}n\,(n-1)\,P_t(n) = \big\langle n(n-1)\big\rangle\end{aligned}$$

A.3 Laplace transform of the probability generating function

This section explains the mathematical passages by which it is possible to obtain the expression of the Laplace transform of $G(t,\xi)$.

$$\begin{aligned}\widetilde{G}(s,\xi) = \int_0^{\infty}G(t,\xi)e^{-st}dt &= \int_0^{\infty}[1+\sum_{n=1}^{\infty}K_n(t)(\xi-1)\,\xi^{n-1}]e^{-st}dt\\ &= \frac{1}{s}+\sum_{n=1}^{\infty}(\xi-1)\,\xi^{n-1}\int_0^{\infty}K_n(t)e^{-st}dt\end{aligned}$$

The integral can be rewritten by making $K_n(t)$ explicit as follows:

$$\begin{aligned}\int_0^\infty K_n(t)\, e^{-st}\, dt &= \int_0^\infty dt\, e^{-st} \int_0^t f_n(y)\, dy = \int_0^\infty dt\, e^{-st}\, [F_n(t) - F_n(0)] \\ &= \int_0^\infty dt\, e^{-st}\, F_n(t) = \int_0^\infty dt\, \frac{e^{-st}}{s} \frac{\partial}{\partial t} F_n(t) \\ &= \frac{1}{s} \int_0^\infty dt\, e^{-st} f_n(t) = \frac{1}{s}\, \tilde{f}_n(s)\end{aligned}$$

Substituting the integral into the equation of $\widetilde{G}(s, \xi)$, is found:

$$\begin{aligned}\widetilde{G}(s,\xi) &= \frac{1}{s} + \sum_{n=1}^{\infty} (\xi - 1)\, \xi^{n-1} \frac{\widetilde{f}_n(s)}{s} = \frac{1}{s} + \sum_{n=1}^{\infty} (\xi - 1)\, \xi^{n-1} \frac{[\widetilde{f}(s)]^n}{s} \\ &= \frac{1}{s} \left[1 + (\xi - 1)\, \widetilde{f}(s) \sum_{m=0}^{\infty} (\xi\, \widetilde{f}(s))^m \right] = \frac{1}{s} \left[1 + \frac{(\xi - 1)\widetilde{f}(s)}{1 - \xi\, \widetilde{f}(s)} \right] = \frac{1}{s}\, \frac{1 - \widetilde{f}(s)}{1 - \xi\, \widetilde{f}(s)}\end{aligned}$$

Where has it been used the convolution theorem of the Laplace transform and to the closed form of the geometric series.

A.4 Laplace transform of $f(t)$ in the presence of optical losses

This section explains the mathematical passages by which it is possible to obtain the expression of the Laplace transform of $f(t)$.

$$\begin{aligned}\widetilde{f}_{\eta_r}(s) &= \sum_{n=1}^{\infty} \eta_r\, (1 - \eta_r)^{n-1}\, \widetilde{f}_n(s) = \sum_{n=1}^{\infty} \eta_r\, (1 - \eta_r)^{n-1}\, \left[\widetilde{f}(s)\right]^n \\ &= \eta_r \widetilde{f}(s) \sum_{n=1}^{\infty} \left((1 - \eta_r)\, \widetilde{f}(s) \right)^{n-1} = \eta_r \widetilde{f}(s) \sum_{m=0}^{\infty} \left((1 - \eta_r)\, \widetilde{f}(s) \right)^m \\ &= \frac{\eta_r \widetilde{f}(s)}{1 - (1 - \eta_r) \widetilde{f}(s)}\end{aligned}$$

Where has it been used the fundamental formula of the integral calculus and the closed form of the geometric series.

A.5 Statistics in the presence of optical losses

This section explains the mathematical steps by which it is possible to obtain the moments of the emission statistic of a generic source in the presence of optical losses modeled in terms of efficiency η_r. In particular, Eq.(3.28) is used to indicate the probability of detecting k photons in a time interval t in the presence of this non-ideal element.
The derivation of the average value is shown below.

$$\begin{aligned}\big\langle k\big\rangle_{\eta_r} &= \sum_{k=0}^{\infty} k\, P_{\eta_r}(k) = \sum_{k=0}^{\infty}\sum_{n=k}^{\infty} k\, P_t(n)\, \mathcal{B}(k|\, n, \eta_r) \\ &= \sum_{n=0}^{\infty} P_t(n) \sum_{k=0}^{n} k\, \mathcal{B}(k|\, n, \eta_r) = \sum_{n=0}^{\infty} P_t(n)\, \eta_r\, n = \eta_r \big\langle n \big\rangle\end{aligned}$$

Subsequently, the mathematical passages by which the variance is obtained are reported.

$$\begin{aligned}\big\langle k(k-1)\big\rangle_{\eta_r} &= \sum_{k=0}^{\infty} k(k-1)\, P_{\eta_r}(k) = \sum_{k=0}^{\infty}\sum_{n=k}^{\infty} k(k-1)\, P_t(n)\, \mathcal{B}(k|\, n, \eta_r) \\ &= \sum_{n=0}^{\infty} P_t(n) \sum_{k=0}^{n} k(k-1)\, \mathcal{B}(k|\, n, \eta_r) = \sum_{n=0}^{\infty} P_t(n)\, \eta_r^2\, n \sum_{y=0}^{n-2} \mathcal{B}(y|\, (n-2), \eta_r) \\ &= \eta_r^2 \sum_{n=0}^{\infty} P_t(n)\, n\, (n-1) = \eta_r^2 \left\langle n(n-1) \right\rangle\end{aligned}$$

$$\begin{aligned}Var[k]_{\eta_r} &= \big\langle k(k-1)\big\rangle_{\eta_r} + \big\langle k\big\rangle_{\eta_r} - \big\langle k\big\rangle_{\eta_r}^2 = \eta_r^2 \left\langle n(n-1) \right\rangle + \eta_r \big\langle n\big\rangle - \eta_r^2 \big\langle n\big\rangle^2 \\ &= \eta_r^2 Var[n] + \eta_r(1-\eta_r)\big\langle n\big\rangle\end{aligned}$$

Appendix B

Supplementary Material of Section 3.3

B.1 Characteristic function for a discrete probability function p_n of having n photons accounting efficiency η

The characteristic function for a discrete probability function p_n of having n photons in the system described in the section 3.3 is:

$$\Gamma(z) = \sum_{m=0}^{+\infty} p(m) z^m \tag{B.1}$$

Accounting for the efficiency η, the characteristic function in Eq.(B.1) becomes:

$$\begin{aligned}
\Gamma(z) &= \sum_{m=0}^{+\infty} p_\eta(m) z^m = \sum_{m=0}^{+\infty} \sum_{n=0}^{+\infty} \mathcal{B}(m|n\eta)\, p(n) z^m \\
&= \sum_{n=0}^{+\infty} p(n) \sum_{m=0}^{+\infty} \frac{n!}{m!(n-m)!} \eta^m (1-\eta)^{n-m} z^m \\
&= \sum_{n=0}^{+\infty} p(n) \sum_{m=0}^{+\infty} \frac{n!}{m!(n-m)!} (\eta z)^m (1-\eta)^{n-m} \\
&= \sum_{n=0}^{+\infty} p(n)(1-\eta+z\eta)^n = \sum_{n=0}^{+\infty} [1-\eta(1-z)]^n p(n)
\end{aligned}$$

Where the probability $p_\eta(m) = \sum_{n=0}^{+\infty} \mathcal{B}(m|n\eta)\, p(n)$ is inserted.

B.2 Reconstruction algorithm

In least square minimization function (Eq.(3.56) in section 3.3), the $g^{(K)}_{\text{exp}}$'s are calculated as the ratio between the K-fold coincidence probability $Q_{(i_1,...,i_K)}(1)$ and the product of the single detection probabilities $Q_{i_1}(1), ...Q_{i_K}(1)$ of the K SPADs involved, averaged for all possible SPADs combinations. The $\theta^{(K)}_{\text{exp}}$'s are evaluated from the overall no-click probability $Q_{(i_1,...,i_K)}(0)$ and the single branch no-click probabilities $Q_{i_j}(0)$ ($i_j = 1, ..., N$, with $j = 1, ..., K$) of the SPADs considered. As stated above, while the $g^{(K)}$'s by construction do not depend on the efficiency of the detector-tree branches involved in their measurement, the same does not hold for the $\theta^{(K)}$ functions, which are intrinsically η-dependent. For this reason, we took the efficiency unbalance between the branches comprising our detector tree in account by computing six different $\theta^{(2)}(0)$ values, four $\theta^{(3)}(0)$'s and one $\theta^{(4)}(0)$, each corresponding to a different combination of the detector-tree branches.
Furthermore, Lagrange multipliers are introduced in Eq. (3.56) for both $g^{(K)}$ and $\theta^{(K)}$ functions. In particular, for each $g^{(K)}$ a different Lagrange multiplier $\lambda_g(K)$ is used according to the following rule:

$$\lambda_g(K) = \begin{cases} 1/K! & \text{if } g^{(2)}_{\text{exp}}(0) > 1 \\ 1 & \text{otherwise.} \end{cases} \tag{B.2}$$

Whenever $g^{(2)}_{\text{exp}}(0) \leq 1$, a unity Lagrange multiplier is applied to all Glauber functions ($\lambda_g(K) = 1 \ \forall K$). Otherwise, we divide the corresponding square difference by the value $K!$, accounting for the factorial growth of $g^{(K)}(0)$ with K for thermal modes. In addition, the higher the order of an experimentally measured Glauber function, the higher is the associated uncertainty. Thus, order-dependent Lagrange multipliers reduce the impact of uncertainties for large K's. For all $\theta^{(K)}$ functions, instead, we use the same Lagrange multiplier λ_θ, chosen case by case to make $\theta^{(K)}$'s contribution to Eq. (3.56) match the size of the one due to the $g^{(K)}$ functions. To do this, we recursively run the minimization algorithm, progressively adjusting λ_θ to equilibrate the $g^{(K)}$ and $\theta^{(K)}$ minima. Finally, to increase the robustness and reliability of our reconstruction method, we exploit the single-branch no-click probabilities $Q_i(0)$ as a constraint on the overall photon number distribution of the

reconstructed photon state. Our minimization is carried on any four of nine unknown parameters, each characterizing a different source: μ is the mean photon number for the coherent mode, $\nu_1, \ldots, \nu_4$ are the ones for the thermal modes and $p_1, \ldots, p_4$ are the emission probabilities of the single-photon emitters for the single-photon modes.

Bibliography

[1] ML Markham, JM Dodson, GA Scarsbrook, DJ Twitchen, G Balasubramanian, F Jelezko, and J Wrachtrup. Cvd diamond for spintronics. *Diamond and Related Materials*, 20(2):134–139, 2011.

[2] Jagdish Narayan and Anagh Bhaumik. Novel synthesis and properties of pure and nv-doped nanodiamonds and other nanostructures. *Materials Research Letters*, 5(4):242–250, 2017.

[3] Christopher M Breeding and James E Shigley. The "type" classification system of diamonds and its importance in gemology. *Gems & Gemology*, 45(2):96–111, 2009.

[4] David P DiVincenzo. The physical implementation of quantum computation. *Fortschritte der Physik: Progress of Physics*, 48(9-11):771–783, 2000.

[5] Romain Alléaume, François Treussart, Gaëtan Messin, Yannick Dumeige, Jean-François Roch, Alexios Beveratos, Rosa Brouri-Tualle, Jean-Philippe Poizat, and Philippe Grangier. Experimental open-air quantum key distribution with a single-photon source. *New Journal of physics*, 6(1):92, 2004.

[6] L Fleury, J-M Segura, G Zumofen, B Hecht, and UP Wild. Nonclassical photon statistics in single-molecule fluorescence at room temperature. *Physical review letters*, 84(6):1148, 2000.

[7] Philippe Grangier, Gerard Roger, and Alain Aspect. Experimental evidence for a photon anticorrelation effect on a beam splitter: a new light on single-photon interferences. *EPL (Europhysics Letters)*, 1(4):173, 1986.

[8] Stefano Pirandola, Ulrik L Andersen, Leonardo Banchi, Mario Berta, Darius Bunandar, Roger Colbeck, Dirk Englund, Tobias Gehring, Cosmo Lupo, Carlo Ottaviani, et al. Advances in quantum cryptography. *Advances in optics and photonics*, 12(4):1012–1236, 2020.

[9] Marco Genovese. Real applications of quantum imaging. *Journal of Optics*, 18(7):073002, 2016.

[10] Marco Genovese. Experimental quantum enhanced optical interferometry. *AVS Quantum Science*, 3(4):044702, 2021.

[11] Jianwei Wang, Fabio Sciarrino, Anthony Laing, and Mark G Thompson. Integrated photonic quantum technologies. *Nature Photonics*, 14(5):273–284, 2020.

[12] Giulia Petrini, Ekaterina Moreva, Ettore Bernardi, Paolo Traina, Giulia Tomagra, Valentina Carabelli, Ivo Pietro Degiovanni, and Marco Genovese. Is a quantum biosensing revolution approaching? perspectives in nv-assisted current and thermal biosensing in living cells. *Advanced Quantum Technologies*, 3(12):2000066, 2020.

[13] Alan Migdall, Sergey V Polyakov, Jingyun Fan, and Joshua C Bienfang. *Single-photon generation and detection: physics and applications*. Academic Press, 2013.

[14] Frank Arute, Kunal Arya, Ryan Babbush, Dave Bacon, Joseph C Bardin, Rami Barends, Rupak Biswas, Sergio Boixo, Fernando GSL Brandao, David A Buell, et al. Quantum supremacy using a programmable superconducting processor. *Nature*, 574(7779):505–510, 2019.

[15] M Chipaux, L Toraille, Ch Larat, L Morvan, S Pezzagna, J Meijer, and Th Debuisschert. Wide bandwidth instantaneous radio frequency spectrum analyzer based on nitrogen vacancy centers in diamond. *Applied Physics Letters*, 107(23):233502, 2015.

[16] Qi-Chao Sun, Tiancheng Song, Eric Anderson, Andreas Brunner, Johannes Förster, Tetyana Shalomayeva, Takashi Taniguchi, Kenji

Watanabe, Joachim Gräfe, Rainer Stöhr, et al. Magnetic domains and domain wall pinning in atomically thin crbr3 revealed by nanoscale imaging. *Nature communications*, 12(1):1–7, 2021.

[17] Guido Zambra, Alessandra Andreoni, Maria Bondani, Marco Gramegna, Marco Genovese, Giorgio Brida, Andrea Rossi, and Matteo GA Paris. Experimental reconstruction of photon statistics without photon counting. *Physical review letters*, 95(6):063602, 2005.

[18] Georg Harder, Ch Silberhorn, J Rehacek, Z Hradil, L Motka, B Stoklasa, and Luis Lorenzo Sánchez-Soto. Time-multiplexed measurements of nonclassical light at telecom wavelengths. *Physical review A*, 90(4):042105, 2014.

[19] Malte Avenhaus, Hendrik B Coldenstrodt-Ronge, Kaisa Laiho, Wolfgang Mauerer, Ian A Walmsley, and Christine Silberhorn. Photon number statistics of multimode parametric down-conversion. *Physical review letters*, 101(5):053601, 2008.

[20] Matteo Paris and Jaroslav Rehacek. *Quantum state estimation*, volume 649. Springer Science & Business Media, 2004.

[21] Paolo Facchi, Giuseppe Florio, and Saverio Pascazio. Probability-density-function characterization of multipartite entanglement. *Physical Review A*, 74(4):042331, 2006.

[22] N Bent, H Qassim, AA Tahir, D Sych, G Leuchs, Luis Lorenzo Sánchez-Soto, E Karimi, and RW Boyd. Experimental realization of quantum tomography of photonic qudits via symmetric informationally complete positive operator-valued measures. *Physical Review X*, 5(4):041006, 2015.

[23] Ch Marquardt, J Heersink, R Dong, MV Chekhova, AB Klimov, LL Sánchez-Soto, Ulrik Lund Andersen, and G Leuchs. Quantum reconstruction of an intense polarization squeezed optical state. *Physical review letters*, 99(22):220401, 2007.

[24] M Avenhaus, K Laiho, MV Chekhova, and Ch Silberhorn. Accessing higher order correlations in quantum optical states by time multiplexing. *Physical review letters*, 104(6):063602, 2010.

[25] Luca Rigovacca, Carlo Di Franco, Benjamin J Metcalf, Ian A Walmsley, and MS Kim. Nonclassicality criteria in multiport interferometry. *Physical Review Letters*, 117(21):213602, 2016.

[26] Jan Sperling, WR Clements, Andreas Eckstein, Meritt Moore, JJ Renema, WS Kolthammer, Sae Woo Nam, Adriana Lita, Thomas Gerrits, Wolfgang Vogel, et al. Detector-independent verification of quantum light. *Physical review letters*, 118(16):163602, 2017.

[27] Jan Peřina Jr, Ondřej Haderka, and Václav Michálek. Nonclassicality and entanglement criteria for bipartite optical fields characterized by quadratic detectors. ii. criteria based on probabilities. *Physical Review A*, 102(4):043713, 2020.

[28] DN Klyshko. Observable signs of nonclassical light. *Physics Letters A*, 213(1-2):7–15, 1996.

[29] Christopher J Chunnilall, Ivo Pietro Degiovanni, Stefan Kück, Ingmar Müller, and Alastair G Sinclair. Metrology of single-photon sources and detectors: a review. *Optical Engineering*, 53(8):081910, 2014.

[30] Matthew D Eisaman, Jingyun Fan, Alan Migdall, and Sergey V Polyakov. Invited review article: Single-photon sources and detectors. *Review of scientific instruments*, 82(7):071101, 2011.

[31] H Paul, P Törmä, T Kiss, and I Jex. Photon chopping: New way to measure the quantum state of light. *Physical review letters*, 76(14):2464, 1996.

[32] Valentina Schettini, Sergey V Polyakov, Ivo P Degiovanni, Giorgio Brida, Stefania Castelletto, and Alan L Migdall. Implementing a multiplexed system of detectors for higher photon counting rates. *IEEE Journal of Selected Topics in Quantum Electronics*, 13(4):978–983, 2007.

[33] Aleksander Divochiy, Francesco Marsili, David Bitauld, Alessandro Gaggero, Roberto Leoni, Francesco Mattioli, Alexander Korneev, Vitaliy Seleznev, Nataliya Kaurova, Olga Minaeva, et al. Superconducting nanowire photon-number-resolving detector at telecommunication wavelengths. *Nature Photonics*, 2(5):302–306, 2008.

[34] D Rosenberg, AJ Kerman, RJ Molnar, and EA Dauler. High-speed and high-efficiency superconducting nanowire single photon detector array. *Optics express*, 21(2):1440–1447, 2013.

[35] MJ Fitch, BC Jacobs, TB Pittman, and JD Franson. Photon-number resolution using time-multiplexed single-photon detectors. *Physical Review A*, 68(4):043814, 2003.

[36] Daryl Achilles, Christine Silberhorn, Cezary Śliwa, Konrad Banaszek, and Ian A Walmsley. Fiber-assisted detection with photon number resolution. *Optics letters*, 28(23):2387–2389, 2003.

[37] Fabrizio Piacentini, MP Levi, Alessio Avella, M López, S Kück, SV Polyakov, Ivo P Degiovanni, Giorgio Brida, and Marco Genovese. Positive operator-valued measure reconstruction of a beam-splitter tree-based photon-number-resolving detector. *Optics letters*, 40(7):1548–1551, 2015.

[38] Elizabeth A Goldschmidt, Fabrizio Piacentini, Ivano Ruo Berchera, Sergey V Polyakov, Silke Peters, Stefan Kück, Giorgio Brida, Ivo P Degiovanni, Alan Migdall, and Marco Genovese. Mode reconstruction of a light field by multiphoton statistics. *Physical Review A*, 88(1):013822, 2013.

[39] Lukáš Lachman, Lukáš Slodička, and Radim Filip. Nonclassical light from a large number of independent single-photon emitters. *Scientific reports*, 6(1):1–8, 2016.

[40] E Moreva, P Traina, J Forneris, IP Degiovanni, S Ditalia Tchernij, F Picollo, G Brida, P Olivero, and M Genovese. Direct experimental observation of nonclassicality in ensembles of single-photon emitters. *Physical Review B*, 96(19):195209, 2017.

[41] Petr Obšil, Lukáš Lachman, Tuan Pham, Adam Lešundák, V Hucl, M Čížek, Jan Hrabina, Ondřej Číp, Lukáš Slodička, and Radim Filip. Nonclassical light from large ensembles of trapped ions. *Physical Review Letters*, 120(25):253602, 2018.

[42] Luo Qi, Mathieu Manceau, Andrea Cavanna, Fabian Gumpert, Luigi Carbone, Massimo de Vittorio, Alberto Bramati, Elisabeth Giacobino, Lukas Lachman, Radim Filip, et al. Multiphoton nonclassical light from clusters of single-photon emitters. *New Journal of Physics*, 20(7):073013, 2018.

[43] Christian Kurtsiefer, Sonja Mayer, Patrick Zarda, and Harald Weinfurter. Stable solid-state source of single photons. *Physical review letters*, 85(2):290, 2000.

[44] David Steinmetz, Elke Neu, Jan Meijer, Wolfgang Bolse, and Christoph Becher. Single photon emitters based on ni/si related defects in single crystalline diamond. *Applied Physics B*, 102(3):451–458, 2011.

[45] Igor Aharonovich, Chunyuan Zhou, Alastair Stacey, Julius Orwa, Stefania Castelletto, David Simpson, Andrew D Greentree, François Treussart, Jean-Francois Roch, and Steven Prawer. Enhanced single-photon emission in the near infrared from a diamond color center. *Physical Review B*, 79(23):235316, 2009.

[46] DA Simpson, E Ampem-Lassen, BC Gibson, Steven Trpkovski, FM Hossain, ST Huntington, AD Greentree, LCL Hollenberg, and Steven Prawer. A highly efficient two level diamond based single photon source. *Applied Physics Letters*, 94(20):203107, 2009.

[47] Tina Müller, Christian Hepp, Benjamin Pingault, Elke Neu, Stefan Gsell, Matthias Schreck, Hadwig Sternschulte, Doris Steinmüller-Nethl, Christoph Becher, and Mete Atatüre. Optical signatures of silicon-vacancy spins in diamond. *Nature communications*, 5(1):1–7, 2014.

[48] Carlo Bradac, Weibo Gao, Jacopo Forneris, Matthew E Trusheim, and Igor Aharonovich. Quantum nanophotonics with group iv defects in diamond. *Nature communications*, 10(1):1–13, 2019.

[49] Takayuki Iwasaki, Fumitaka Ishibashi, Yoshiyuki Miyamoto, Satoshi Kobayashi, Takehide Miyazaki, Kosuke Tahara, Kay D Jahnke, Lachlan J Rogers, Boris Naydenov, Fedor Jelezko, et al. Germanium-vacancy single color centers in diamond. *Scientific reports*, 5(1):1–7, 2015.

[50] Sviatoslav Ditalia Tchernij, T Luhmann, T Herzig, J Kupper, A Damin, S Santonocito, Matteo Signorile, P Traina, Ekaterina Moreva, F Celegato, et al. Single-photon emitters in lead-implanted single-crystal diamond. *ACS Photonics*, 5(12):4864–4871, 2018.

[51] OA Shcherbina, GA Shcherbina, M Manceau, S Vezzoli, L Carbone, M De Vittorio, A Bramati, E Giacobino, MV Chekhova, and G Leuchs. Photon correlations for colloidal nanocrystals and their clusters. *Optics letters*, 39(7):1791–1794, 2014.

[52] Chunlang Wang. *A solid-state single photon source based on color centers in diamond*. PhD thesis, lmu, 2007.

[53] François Treussart, Romain Alléaume, Véronique Le Floc'h, LT Xiao, J-M Courty, and J-F Roch. Direct measurement of the photon statistics of a triggered single photon source. *Physical review letters*, 89(9):093601, 2002.

[54] Romain Alléaume, Francois Treussart, Jean-Michel Courty, and Jean-Francois Roch. Photon statistics characterization of a single-photon source. *New Journal of physics*, 6(1):85, 2004.

[55] Hristina Georgieva, Alice Meda, Sebastian MF Raupach, Helmuth Hofer, Marco Gramegna, Ivo Pietro Degiovanni, Marco Genovese, Marco López, and Stefan Kück. Detection of ultra-weak laser pulses by free-running single-photon detectors: modeling dead time and dark counts effects. *Applied Physics Letters*, 118(17):174002, 2021.

[56] Giorgio Brida, Ivo Pietro Degiovanni, Marco Genovese, A Migdall, Fabrizio Piacentini, SV Polyakov, and I Ruo Berchera. Experimental realization of a low-noise heralded single-photon source. *Optics express*, 19(2):1484–1492, 2011.

[57] Giorgio Brida, Ivo Pietro Degiovanni, M Genovese, Fabrizio Piacentini, Paolo Traina, Adriano Della Frera, Alberto Tosi, Andrea Bahgat Shehata, Carmelo Scarcella, Angelo Gulinatti, et al. An extremely low-noise heralded single-photon source: A breakthrough for quantum technologies. *Applied Physics Letters*, 101(22):221112, 2012.

[58] JoHoNo Loubser and JoA van Wyk. Electron spin resonance in the study of diamond. *Reports on Progress in Physics*, 41(8):1201, 1978.

[59] MW Doherty, F Dolde, H Fedder, Fedor Jelezko, J Wrachtrup, NB Manson, and LCL Hollenberg. Theory of the ground-state spin of the nv-center in diamond. *Physical Review B*, 85(20):205203, 2012.

[60] Erik Bauch, Connor A Hart, Jennifer M Schloss, Matthew J Turner, John F Barry, Pauli Kehayias, Swati Singh, and Ronald L Walsworth. Ultralong dephasing times in solid-state spin ensembles via quantum control. *Physical Review X*, 8(3):031025, 2018.

[61] Chang S Shin, Mark C Butler, Hai-Jing Wang, Claudia E Avalos, Scott J Seltzer, Ren-Bao Liu, Alexander Pines, and Vikram S Bajaj. Optically detected nuclear quadrupolar interaction of n 14 in nitrogen-vacancy centers in diamond. *Physical Review B*, 89(20):205202, 2014.

[62] S Felton, AM Edmonds, ME Newton, PM Martineau, D Fisher, DJ Twitchen, and JM Baker. Hyperfine interaction in the ground state of the negatively charged nitrogen vacancy center in diamond. *Physical Review B*, 79(7):075203, 2009.

[63] Xing-Fei He, Neil B Manson, and Peter TH Fisk. Paramagnetic resonance of photoexcited n-v defects in diamond. ii. hyperfine interaction with the n 14 nucleus. *Physical Review B*, 47(14):8816, 1993.

[64] Gopalakrishnan Balasubramanian, IY Chan, Roman Kolesov, Mohannad Al-Hmoud, Julia Tisler, Chang Shin, Changdong Kim, Aleksander Wojcik, Philip R Hemmer, Anke Krueger, et al. Nanoscale imaging magnetometry with diamond spins under ambient conditions. *Nature*, 455(7213):648–651, 2008.

[65] Marcus W Doherty, Neil B Manson, Paul Delaney, Fedor Jelezko, Jörg Wrachtrup, and Lloyd CL Hollenberg. The nitrogen-vacancy colour centre in diamond. *Physics Reports*, 528(1):1–45, 2013.

[66] Linh My Pham, David Le Sage, Paul L Stanwix, Tsun Kwan Yeung, D Glenn, Alexei Trifonov, Paola Cappellaro, Philip R Hemmer, Mikhail D Lukin, Hongkun Park, et al. Magnetic field imaging with nitrogen-vacancy ensembles. *New Journal of Physics*, 13(4):045021, 2011.

[67] Jennifer M Schloss, John F Barry, Matthew J Turner, and Ronald L Walsworth. Simultaneous broadband vector magnetometry using solid-state spins. *Physical Review Applied*, 10(3):034044, 2018.

[68] JM Taylor, P Cappellaro, L Childress, L Jiang, D Budker, PR Hemmer, A Yacoby, R Walsworth, and MD Lukin. High-sensitivity diamond magnetometer with nanoscale resolution. *Nature Physics*, 4(10):810–816, 2008.

[69] CL Degen. Scanning magnetic field microscope with a diamond single-spin sensor. *Applied Physics Letters*, 92(24):243111, 2008.

[70] Jeronimo R Maze, Paul L Stanwix, James S Hodges, Seungpyo Hong, Jacob M Taylor, Paola Cappellaro, Liang Jiang, MV Gurudev Dutt, Emre Togan, AS Zibrov, et al. Nanoscale magnetic sensing with an individual electronic spin in diamond. *Nature*, 455(7213):644–647, 2008.

[71] Victor M Acosta, Erik Bauch, Micah P Ledbetter, Charles Santori, K-MC Fu, Paul E Barclay, Raymond G Beausoleil, Héloïse Linget, Jean Francois Roch, Francois Treussart, et al. Diamonds with a high density of nitrogen-vacancy centers for magnetometry applications. *Physical Review B*, 80(11):115202, 2009.

[72] Ekaterina Moreva. The biosensing with nv centers in diamond: Related challenges. *International Journal of Quantum Information*, 18(01):1941023, 2020.

[73] Varun KA Sreenivasan, Andrei V Zvyagin, and Ewa M Goldys. Luminescent nanoparticles and their applications in the life sciences. *Journal of Physics: Condensed Matter*, 25(19):194101, 2013.

[74] Florian Dolde, Helmut Fedder, Marcus W Doherty, Tobias Nöbauer, Florian Rempp, Gopalakrishnan Balasubramanian, Thomas Wolf, Friedemann Reinhard, Lloyd CL Hollenberg, Fedor Jelezko, et al. Electric-field sensing using single diamond spins. *Nature Physics*, 7(6):459–463, 2011.

[75] Eric Van Oort and Max Glasbeek. Electric-field-induced modulation of spin echoes of nv centers in diamond. *Chemical Physics Letters*, 168(6):529–532, 1990.

[76] Victor M Acosta, Erik Bauch, Micah P Ledbetter, Amir Waxman, L-S Bouchard, and Dmitry Budker. Temperature dependence of the nitrogen-vacancy magnetic resonance in diamond. *Physical review letters*, 104(7):070801, 2010.

[77] X-D Chen, C-H Dong, F-W Sun, C-L Zou, J-M Cui, Z-F Han, and G-C Guo. Temperature dependent energy level shifts of nitrogen-vacancy centers in diamond. *Applied Physics Letters*, 99(16):161903, 2011.

[78] Yan-Kai Tzeng, Pei-Chang Tsai, Hsiou-Yuan Liu, Oliver Y Chen, Hsiang Hsu, Fu-Goul Yee, Ming-Shien Chang, and Huan-Cheng Chang. Time-resolved luminescence nanothermometry with nitrogen-vacancy centers in nanodiamonds. *Nano letters*, 15(6):3945–3952, 2015.

[79] A Gruber, A Dräbenstedt, C Tietz, L Fleury, J Wrachtrup, and C Von Borczyskowski. Scanning confocal optical microscopy and magnetic resonance on single defect centers. *Science*, 276(5321):2012–2014, 1997.

[80] M Vengalattore, JM Higbie, SR Leslie, J Guzman, LE Sadler, and DM Stamper-Kurn. High-resolution magnetometry with a spinor bose-einstein condensate. *Physical review letters*, 98(20):200801, 2007.

[81] MI Faley, U Poppe, K Urban, DN Paulson, and RL Fagaly. A new generation of the hts multilayer dc-squid magnetometers and gradiometers.

In *Journal of physics: conference series*, volume 43, page 292. IOP Publishing, 2006.

[82] F Baudenbacher, LE Fong, JR Holzer, and M Radparvar. Monolithic low-transition-temperature superconducting magnetometers for high resolution imaging magnetic fields of room temperature samples. *Applied Physics Letters*, 82(20):3487–3489, 2003.

[83] Yulia G Ermakova, Aleksandr A Lanin, Ilya V Fedotov, Matvey Roshchin, Ilya V Kelmanson, Dmitry Kulik, Yulia A Bogdanova, Arina G Shokhina, Dmitry S Bilan, Dmitry B Staroverov, et al. Thermogenetic neurostimulation with single-cell resolution. *Nature communications*, 8(1):1–15, 2017.

[84] David Le Sage, Koji Arai, David R Glenn, Stephen J DeVience, Linh M Pham, Lilah Rahn-Lee, Mikhail D Lukin, Amir Yacoby, Arash Komeili, and Ronald L Walsworth. Optical magnetic imaging of living cells. *Nature*, 496(7446):486–489, 2013.

[85] Hunter C Davis, Pradeep Ramesh, Aadyot Bhatnagar, Audrey Lee-Gosselin, John F Barry, David R Glenn, Ronald L Walsworth, and Mikhail G Shapiro. Mapping the microscale origins of magnetic resonance image contrast with subcellular diamond magnetometry. *Nature communications*, 9(1):1–9, 2018.

[86] John F Barry, Jennifer M Schloss, Erik Bauch, Matthew J Turner, Connor A Hart, Linh M Pham, and Ronald L Walsworth. Sensitivity optimization for nv-diamond magnetometry. *Reviews of Modern Physics*, 92(1):015004, 2020.

[87] David A Simpson, Emma Morrisroe, Julia M McCoey, Alain H Lombard, Dulini C Mendis, Francois Treussart, Liam T Hall, Steven Petrou, and Lloyd CL Hollenberg. Non-neurotoxic nanodiamond probes for intraneuronal temperature mapping. *ACS nano*, 11(12):12077–12086, 2017.

[88] Masazumi Fujiwara, Simo Sun, Alexander Dohms, Yushi Nishimura, Ken Suto, Yuka Takezawa, Keisuke Oshimi, Li Zhao, Nikola Sadzak,

Yumi Umehara, Yoshio Teki, Naoki Komatsu, Oliver Benson, Yutaka Shikano, and Eriko Kage-Nakadai. Real-time nanodiamond thermometry probing in-vivo thermogenic responses, 2020.

[89] Erwin Neher and Bert Sakmann. The patch clamp technique. *Scientific American*, 266(3):44–51, 1992.

[90] Alfred Stett, Ulrich Egert, Elke Guenther, Frank Hofmann, Thomas Meyer, Wilfried Nisch, and Hugo Haemmerle. Biological application of microelectrode arrays in drug discovery and basic research. *Analytical and bioanalytical chemistry*, 377(3):486–495, 2003.

[91] Single-Channel Recording. edited by b. sakmann and n. neher, 1995.

[92] Richard T Mathias, Ira S Cohen, and Carlos Oliva. Limitations of the whole cell patch clamp technique in the control of intracellular concentrations. *Biophysical journal*, 58(3):759, 1990.

[93] Michael Fejtl, Alfred Stett, Wilfried Nisch, Karl-Heinz Boven, and Andreas Möller. On micro-electrode array revival: its development, sophistication of recording, and stimulation. In *Advances in network electrophysiology*, pages 24–37. Springer, 2006.

[94] Micha E Spira and Aviad Hai. Multi-electrode array technologies for neuroscience and cardiology. *Nature nanotechnology*, 8(2):83, 2013.

[95] Svenja Knappe, Tilmann H Sander, Olaf Kosch, Frank Wiekhorst, John Kitching, and Lutz Trahms. Cross-validation of microfabricated atomic magnetometers with superconducting quantum interference devices for biomagnetic applications. *Applied Physics Letters*, 97(13):133703, 2010.

[96] Anri Nakajima. Application of single-electron transistor to biomolecule and ion sensors. *Applied Sciences*, 6(4):94, 2016.

[97] Jubayer Jalil, Yong Zhu, Chandima Ekanayake, and Yong Ruan. Sensing of single electrons using micro and nano technologies: a review. *Nanotechnology*, 28(14):142002, 2017.

[98] Yoshiaki Takei, Satoshi Arai, Atsushi Murata, Masao Takabayashi, Kotaro Oyama, Shin'ichi Ishiwata, Shinji Takeoka, and Madoka Suzuki. A nanoparticle-based ratiometric and self-calibrated fluorescent thermometer for single living cells. *ACS nano*, 8(1):198–206, 2014.

[99] Duan P Chen, Robert S Eisenberg, Joseph W Jerome, and Chi-Wang Shu. Hydrodynamic model of temperature change in open ionic channels. *Biophysical Journal*, 69(6):2304, 1995.

[100] Ahmed El Hady and Benjamin B Machta. Mechanical surface waves accompany action potential propagation. *Nature communications*, 6:6697, 2015.

[101] Ezia Guatteo, Kenny KH Chung, Tharushini K Bowala, Giorgio Bernardi, Nicola B Mercuri, and Janusz Lipski. Temperature sensitivity of dopaminergic neurons of the substantia nigra pars compacta: involvement of transient receptor potential channels. *Journal of neurophysiology*, 94(5):3069–3080, 2005.

[102] Jon S Donner, Sebastian A Thompson, Mark P Kreuzer, Guillaume Baffou, and Romain Quidant. Mapping intracellular temperature using green fluorescent protein. *Nano letters*, 12(4):2107–2111, 2012.

[103] Jui-Ming Yang, Haw Yang, and Liwei Lin. Quantum dot nano thermometers reveal heterogeneous local thermogenesis in living cells. *ACS nano*, 5(6):5067–5071, 2011.

[104] Soo Ho Kim, Jermim Noh, Min Ku Jeon, Ki Woong Kim, Luke P Lee, and Seong Ihl Woo. Micro-raman thermometry for measuring the temperature distribution inside the microchannel of a polymerase chain reaction chip. *Journal of Micromechanics and Microengineering*, 16(3):526, 2006.

[105] Fiorenzo Vetrone, Rafik Naccache, Alicia Zamarron, Angeles Juarranz de la Fuente, Francisco Sanz-Rodriguez, Laura Martinez Maestro, Emma Martin Rodriguez, Daniel Jaque, Jose Garciia Sole, and John A Capobianco. Temperature sensing using fluorescent nanothermometers. *ACS nano*, 4(6):3254–3258, 2010.

[106] Laura Martinez Maestro, Emma Martin Rodriguez, Francisco Sanz Rodriguez, MC Iglesias-de la Cruz, Angeles Juarranz, Rafik Naccache, Fiorenzo Vetrone, Daniel Jaque, John A Capobianco, and Jose Garcia Sole. Cdse quantum dots for two-photon fluorescence thermal imaging. *Nano letters*, 10(12):5109–5115, 2010.

[107] Laura Martinez Maestro, Qiming Zhang, Xiangping Li, Daniel Jaque, and Min Gu. Quantum-dot based nanothermometry in optical plasmonic recording media. *Applied Physics Letters*, 105(18):181110, 2014.

[108] Ellen C Jensen. Use of fluorescent probes: their effect on cell biology and limitations. *The Anatomical Record: Advances in Integrative Anatomy and Evolutionary Biology*, 295(12):2031–2036, 2012.

[109] Tytus Bernas, Bartlomiej P Rajwa, Elikplimki K Asem, and Joseph Paul Robinson. Loss of image quality in photobleaching during microscopic imaging of fluorescent probes bound to chromatin. *Journal of biomedical optics*, 10(6):064015, 2005.

[110] CDS Brites, A Millán, and LD Carlos. Lanthanides in luminescent thermometry. In *Handbook on the Physics and Chemistry of Rare Earths*, volume 49, pages 339–427. Elsevier, 2016.

[111] Shu-Jung Yu, Ming-Wei Kang, Huan-Cheng Chang, Kuan-Ming Chen, and Yueh-Chung Yu. Bright fluorescent nanodiamonds: no photobleaching and low cytotoxicity. *Journal of the American Chemical Society*, 127(50):17604–17605, 2005.

[112] Romana Schirhagl, Kevin Chang, Michael Loretz, and Christian L Degen. Nitrogen-vacancy centers in diamond: nanoscale sensors for physics and biology. *Annual review of physical chemistry*, 65:83–105, 2014.

[113] John F Barry, Matthew J Turner, Jennifer M Schloss, David R Glenn, Yuyu Song, Mikhail D Lukin, Hongkun Park, and Ronald L Walsworth. Optical magnetic detection of single-neuron action potentials using quantum defects in diamond. *Proceedings of the National Academy of Sciences*, 113(49):14133–14138, 2016.

[114] Christian G Specht, Oliver A Williams, Richard B Jackman, and Ralf Schoepfer. Ordered growth of neurons on diamond. *Biomaterials*, 25(18):4073–4078, 2004.

[115] Georg Kucsko, Peter C Maurer, Norman Ying Yao, MICHAEL Kubo, Hyun Jong Noh, Po Kam Lo, Hongkun Park, and Mikhail D Lukin. Nanometre-scale thermometry in a living cell. *Nature*, 500(7460):54–58, 2013.

[116] DM Toyli, DJ Christle, A Alkauskas, BB Buckley, CG Van de Walle, and DD Awschalom. Measurement and control of single nitrogen-vacancy center spins above 600 k. *Physical Review X*, 2(3):031001, 2012.

[117] Taras Plakhotnik, Marcus W Doherty, Jared H Cole, Robert Chapman, and Neil B Manson. All-optical thermometry and thermal properties of the optically detected spin resonances of the nv–center in nanodiamond. *Nano letters*, 14(9):4989–4996, 2014.

[118] Jan Müller, Marco Ballini, Paolo Livi, Yihui Chen, Milos Radivojevic, Amir Shadmani, Vijay Viswam, Ian L Jones, Michele Fiscella, Roland Diggelmann, et al. High-resolution cmos mea platform to study neurons at subcellular, cellular, and network levels. *Lab on a Chip*, 15(13):2767–2780, 2015.

[119] Gabriel Bertotti, Dmytro Velychko, Norman Dodel, Stefan Keil, Dirk Wolansky, Bernd Tillak, Matthias Schreiter, Andreas Grall, Peter Jesinger, Sebastian Röhler, et al. A cmos-based sensor array for in-vitro neural tissue interfacing with 4225 recording sites and 1024 stimulation sites. In *2014 IEEE Biomedical Circuits and Systems Conference (BioCAS) Proceedings*, pages 304–307. IEEE, 2014.

[120] Douglas J Bakkum, Urs Frey, Milos Radivojevic, Thomas L Russell, Jan Müller, Michele Fiscella, Hirokazu Takahashi, and Andreas Hierlemann. Tracking axonal action potential propagation on a high-density microelectrode array across hundreds of sites. *Nature communications*, 4(1):1–12, 2013.

[121] György Buzsáki, Eran Stark, Antal Berényi, Dion Khodagholy, Daryl R Kipke, Euisik Yoon, and Kensall D Wise. Tools for probing local circuits: high-density silicon probes combined with optogenetics. *Neuron*, 86(1):92–105, 2015.

[122] Milos Radivojevic, David Jäckel, Michael Altermatt, Jan Müller, Vijay Viswam, Andreas Hierlemann, and Douglas J Bakkum. Electrical identification and selective microstimulation of neuronal compartments based on features of extracellular action potentials. *Scientific reports*, 6:31332, 2016.

[123] Giulia Tomagra, Pietro Aprà, Alfio Battiato, Cecilia Colla Ruvolo, Alberto Pasquarelli, Andrea Marcantoni, Emilio Carbone, Valentina Carabelli, Paolo Olivero, and Federico Picollo. Micro graphite-patterned diamond sensors: Towards the simultaneous in vitro detection of molecular release and action potentials generation from excitable cells. *Carbon*, 152:424–433, 2019.

[124] Michael Hines. Neuron—a program for simulation of nerve equations. In *Neural systems: Analysis and modeling*, pages 127–136. Springer, 1993.

[125] Michael L Hines and Nicholas T Carnevale. The neuron simulation environment. *Neural computation*, 9(6):1179–1209, 1997.

[126] F Santamaria and JM Bower. Hodgkin-huxley models. In *Encyclopedia of Neuroscience*, pages 1173–1180. Elsevier Ltd, 2009.

[127] Blaise Agüera y Arcas, Adrienne L Fairhall, and William Bialek. Computation in a single neuron: Hodgkin and huxley revisited. *Neural Computation*, 15(8):1715–1749, 2003.

[128] Matthew N Rasband and James S Trimmer. Developmental clustering of ion channels at and near the node of ranvier. *Developmental biology*, 236(1):5–16, 2001.

[129] Daisuke Sato, Gonzalo Hernández-Hernández, Collin Matsumoto, Sendoa Tajada, Claudia M Moreno, Rose E Dixon, Samantha O'Dwyer,

Manuel F Navedo, James S Trimmer, Colleen E Clancy, et al. A stochastic model of ion channel cluster formation in the plasma membrane. *Journal of General Physiology*, 151:1116–1134, 2019.

[130] Bokai Zhang, Xi Feng, Hang Yin, Zhenpeng Ge, Yanhuan Wang, Zhiqin Chu, Helena Raabova, Jan Vavra, Petr Cigler, Renbao Liu, et al. Anchored but not internalized: shape dependent endocytosis of nanodiamond. *Scientific reports*, 7:46462, 2017.

[131] Torsten Rendler, Jitka Neburkova, Ondrej Zemek, Jan Kotek, Andrea Zappe, Zhiqin Chu, Petr Cigler, and Jörg Wrachtrup. Optical imaging of localized chemical events using programmable diamond quantum nanosensors. *Nature communications*, 8(1):1–9, 2017.

[132] Jasmina Isakovic, Ian Dobbs-Dixon, Dipesh Chaudhury, and Dinko Mitrecic. Modeling of inhomogeneous electromagnetic fields in the nervous system: a novel paradigm in understanding cell interactions, disease etiology and therapy. *Scientific reports*, 8(1):1–20, 2018.

[133] Mürsel Karadas, Adam M Wojciechowski, Alexander Huck, Nils Ole Dalby, Ulrik Lund Andersen, and Axel Thielscher. Feasibility and resolution limits of opto-magnetic imaging of neural network activity in brain slices using color centers in diamond. *Scientific reports*, 8(1):1–14, 2018.

[134] LT Hall, GCG Beart, EA Thomas, DA Simpson, LP McGuinness, JH Cole, JH Manton, RE Scholten, Fedor Jelezko, Jörg Wrachtrup, et al. High spatial and temporal resolution wide-field imaging of neuron activity using quantum nv-diamond. *Scientific reports*, 2:401, 2012.

[135] Matti Hämäläinen, Riitta Hari, Risto J Ilmoniemi, Jukka Knuutila, and Olli V Lounasmaa. Magnetoencephalography—theory, instrumentation, and applications to noninvasive studies of the working human brain. *Reviews of modern Physics*, 65(2):413, 1993.

[136] Rolf Simon Schoenfeld and Wolfgang Harneit. Real time magnetic field sensing and imaging using a single spin in diamond. *Physical review letters*, 106(3):030802, 2011.

[137] Dmitry Budker and Michael Romalis. Optical magnetometry. *Nature physics*, 3(4):227–234, 2007.

[138] Jukka Sarvas. Basic mathematical and electromagnetic concepts of the biomagnetic inverse problem. *Physics in Medicine & Biology*, 32(1):11, 1987.

[139] Christoph M Michel, Micah M Murray, Göran Lantz, Sara Gonzalez, Laurent Spinelli, and Rolando Grave de Peralta. Eeg source imaging. *Clinical neurophysiology*, 115(10):2195–2222, 2004.

[140] Natalia A Trayanova, Bradley J Roth, and Lisa J Malden. The response of a spherical heart to a uniform electric field: a bidomain analysis of cardiac stimulation. *IEEE transactions on biomedical engineering*, 40(9):899–908, 1993.

[141] Dan Xu and Bradley J Roth. The magnetic field produced by the heart and its influence on mri. *Mathematical Problems in Engineering*, 2017, 2017.

[142] Ryan A Murdick and BJ Roth. A comparative model of two mechanisms from which a magnetic field arises in the heart. *Journal of applied physics*, 95(9):5116–5122, 2004.

[143] Bradley J Roth. A comparison of two boundary conditions used with the bidomain model of cardiac tissue. *Annals of biomedical engineering*, 19(6):669–678, 1991.

[144] Wanda Krassowska and John C Neu. Effective boundary conditions for syncytial tissues. *IEEE transactions on biomedical engineering*, 41(2):143–150, 1994.

[145] Bradley J Roth. Electrical conductivity values used with the bidomain model of cardiac tissue. *IEEE Transactions on Biomedical Engineering*, 44(4):326–328, 1997.

[146] Krista Kay McBride, Bradley J Roth, VY Sidorov, John P Wikswo, and Franz J Baudenbacher. Measurements of transmembrane poten-

tial and magnetic field at the apex of the heart. *Biophysical journal*, 99(10):3113–3118, 2010.

[147] Jenny R Holzer, Luis E Fong, Veniamin Y Sidorov, John P Wikswo Jr, and Franz Baudenbacher. High resolution magnetic images of planar wave fronts reveal bidomain properties of cardiac tissue. *Biophysical journal*, 87(6):4326–4332, 2004.

[148] DG Margineanu and E Schoffeniels. Molecular events and energy changes during the action potential. *Proceedings of the National Academy of Sciences*, 74(9):3810–3813, 1977.

[149] JV Howarth, Joseph Murdoch Ritchie, and D Stagg. The initial heat production in garfish olfactory nerve fibres. *Proceedings of the Royal Society of London. Series B. Biological Sciences*, 205(1160):347–367, 1979.

[150] Aymar CL de Lichtervelde, J Pedro de Souza, and Martin Z Bazant. Heat of nervous conduction: A thermodynamic framework. *Physical Review E*, 101(2):022406, 2020.

[151] Joonhee Choi, Hengyun Zhou, Renate Landig, Hai-Yin Wu, Xiaofei Yu, Stephen E Von Stetina, Georg Kucsko, Susan E Mango, Daniel J Needleman, Aravinthan DT Samuel, et al. Probing and manipulating embryogenesis via nanoscale thermometry and temperature control. *Proceedings of the National Academy of Sciences*, 117(26):14636–14641, 2020.

[152] Leopoldo De Meis, Luisa A Ketzer, Rodrigo Madeiro Da Costa, Ivone Rosa De Andrade, and Marlene Benchimol. Fusion of the endoplasmic reticulum and mitochondrial outer membrane in rats brown adipose tissue: activation of thermogenesis by ca2+. *PloS one*, 5(3):e9439, 2010.

[153] SCOTT M Thompson, LEONA M Masukawa, and DAVID A Prince. Temperature dependence of intrinsic membrane properties and synaptic potentials in hippocampal ca1 neurons in vitro. *Journal of Neuroscience*, 5(3):817–824, 1985.

[154] M Volgushev, TR Vidyasagar, Marina Chistiakova, and UT Eysel. Synaptic transmission in the neocortex during reversible cooling. *Neuroscience*, 98(1):9–22, 2000.

[155] JCF Lee, Joseph C Callaway, and Robert C Foehring. Effects of temperature on calcium transients and ca2+-dependent afterhyperpolarizations in neocortical pyramidal neurons. *Journal of neurophysiology*, 93(4):2012–2020, 2005.

[156] Marcus E Raichle. Behind the scenes of functional brain imaging: a historical and physiological perspective. *Proceedings of the National Academy of Sciences*, 95(3):765–772, 1998.

[157] M Monti, L Brandt, J Ikomi-Kumm, and H Olsson. Microcalorimetric investigation of cell metabolism in tumour cells from patients with non-hodgkin lymphoma (nhl). *Scandinavian journal of haematology*, 36(4):353–357, 1986.

[158] Mahdi Ghavami, Meisam Rezaei, Reza Ejtehadi, Mina Lotfi, Mohammad A Shokrgozar, Baharak Abd Emamy, Jens Raush, and Morteza Mahmoudi. Physiological temperature has a crucial role in amyloid beta in the absence and presence of hydrophobic and hydrophilic nanoparticles. *ACS chemical neuroscience*, 4(3):375–378, 2013.

[159] Puping Liang, Yanwen Xu, Xiya Zhang, Chenhui Ding, Rui Huang, Zhen Zhang, Jie Lv, Xiaowei Xie, Yuxi Chen, Yujing Li, et al. Crispr/cas9-mediated gene editing in human tripronuclear zygotes. *Protein & cell*, 6(5):363–372, 2015.

[160] Masazumi Fujiwara, Simo Sun, Alexander Dohms, Yushi Nishimura, Ken Suto, Yuka Takezawa, Keisuke Oshimi, Li Zhao, Nikola Sadzak, Yumi Umehara, et al. Real-time nanodiamond thermometry probing in vivo thermogenic responses. *Science advances*, 6(37):eaba9636, 2020.

[161] Shigeki Kiyonaka, Taketoshi Kajimoto, Reiko Sakaguchi, Daisuke Shinmi, Mariko Omatsu-Kanbe, Hiroshi Matsuura, Hiromi Imamura, Takenao Yoshizaki, Itaru Hamachi, Takashi Morii, et al. Genetically

encoded fluorescent thermosensors visualize subcellular thermoregulation in living cells. *Nature methods*, 10(12):1232–1238, 2013.

[162] Dominique Chretien, Paule Bénit, Hyung-Ho Ha, Susanne Keipert, Riyad El-Khoury, Young-Tae Chang, Martin Jastroch, Howard T Jacobs, Pierre Rustin, and Malgorzata Rak. Mitochondria are physiologically maintained at close to 50 c. *PLoS biology*, 16(1):e2003992, 2018.

[163] Guillaume Baffou, Hervé Rigneault, Didier Marguet, and Ludovic Jullien. A critique of methods for temperature imaging in single cells. *Nature methods*, 11(9):899–901, 2014.

[164] Madoka Suzuki, Vadim Zeeb, Satoshi Arai, Kotaro Oyama, and Shin'ichi Ishiwata. The 10 5 gap issue between calculation and measurement in single-cell thermometry. *Nature methods*, 12(9):802–803, 2015.

[165] Madoka Suzuki and Taras Plakhotnik. The challenge of intracellular temperature. *Biophysical reviews*, 12(2):593–600, 2020.

[166] D Jaque, LM Maestro, E Escudero, E Martín Rodríguez, JA Capobianco, F Vetrone, A Juarranz De La Fuente, F Sanz-Rodríguez, MC Iglesias-De La Cruz, C Jacinto, et al. Fluorescent nano-particles for multi-photon thermal sensing. *Journal of luminescence*, 133:249–253, 2013.

[167] Meixiu Li, Tao Chen, J Justin Gooding, and Jingquan Liu. Review of carbon and graphene quantum dots for sensing. *ACS sensors*, 4(7):1732–1748, 2019.

[168] SW Allison, GT Gillies, AJ Rondinone, and MR Cates. Nanoscale thermometry via the fluorescence of yag: Ce phosphor particles: measurements from 7 to 77 c. *Nanotechnology*, 14(8):859, 2003.

[169] Laura Guarina, C Calorio, D Gavello, E Moreva, P Traina, A Battiato, S Ditalia Tchernij, J Forneris, M Gai, F Picollo, et al. Nanodiamonds-induced effects on neuronal firing of mouse hippocampal microcircuits. *Scientific Reports*, 8(1):1–14, 2018.

[170] Tongtong Zhang, Goutam Pramanik, Kai Zhang, Michal Gulka, Lingzhi Wang, Jixiang Jing, Feng Xu, Zifu Li, Qiang Wei, Petr Cigler, et al. Toward quantitative bio-sensing with nitrogen–vacancy center in diamond. *ACS sensors*, 6(6):2077–2107, 2021.

[171] Masazumi Fujiwara and Yutaka Shikano. Diamond quantum thermometry: From foundations to applications. *Nanotechnology*, 2021.

[172] Carlo Bradac, Shuang Fang Lim, Huan-Cheng Chang, and Igor Aharonovich. Optical nanoscale thermometry: from fundamental mechanisms to emerging practical applications. *Advanced Optical Materials*, 8(15):2000183, 2020.

[173] Ilya V Fedotov, Maxim A Solotenkov, Matvey S Pochechuev, Olga I Ivashkina, Sergei Ya Kilin, Konstantin V Anokhin, and Aleksei M Zheltikov. All-optical brain thermometry in freely moving animals. *ACS Photonics*, 7(12):3353–3360, 2020.

[174] Pei-Chang Tsai, Chandra P Epperla, Jo-Shan Huang, Oliver Y Chen, Chih-Che Wu, and Huan-Cheng Chang. Measuring nanoscale thermostability of cell membranes with single gold–diamond nanohybrids. *Angewandte Chemie International Edition*, 56(11):3025–3030, 2017.

[175] Weina Liu, Md Noor A Alam, Yan Liu, Viatcheslav N Agafonov, Haoyuan Qi, Kaloian Koynov, Valery A Davydov, Rustem Uzbekov, Ute Kaiser, Theo Lasser, et al. Silicon-vacancy nanodiamonds as high performance near-infrared emitters for live-cell dual-color imaging and thermometry. *Nano letters*, 22(7):2881–2888, 2022.

[176] Kapildeb Ambal and Robert D McMichael. A differential rate meter for real-time peak tracking in optically detected magnetic resonance at low photon count rates. *Review of Scientific Instruments*, 90(2):023907, 2019.

[177] Yingke Wu and Tanja Weil. Recent developments of nanodiamond quantum sensors for biological applications. *Advanced Science*, page 2200059, 2022.

[178] Vadim Tseeb, Madoka Suzuki, Kotaro Oyama, Kaoru Iwai, and Shin'ichi Ishiwata. Highly thermosensitive ca2+ dynamics in a hela cell through ip3 receptors. *HFSP journal*, 3(2):117–123, 2009.

[179] Giulia Petrini, Giulia Tomagra, Ettore Bernardi, Ekaterina Moreva, Paolo Traina, Andrea Marcantoni, Federico Picollo, Klaudia Kvaková, Petr Cígler, Ivo Pietro Degiovanni, Valentina Carabelli, and Marco Genovese. Nanodiamond–quantum sensors reveal temperature variation associated to hippocampal neurons firing. *Advanced Science*, 9(28):2202014, 2022.

[180] Yung-An Huang, Chun-Wei Kao, Kuang-Kai Liu, Hou-Syun Huang, Ming-Han Chiang, Ching-Ren Soo, Huan-Cheng Chang, Tzai-Wen Chiu, Jui-I Chao, and Eric Hwang. The effect of fluorescent nanodiamonds on neuronal survival and morphogenesis. *Scientific reports*, 4(1):1–10, 2014.

[181] Andrea Marcantoni, Maria Sabina Cerullo, Pol Buxeda, Giulia Tomagra, Maurizio Giustetto, Giuseppe Chiantia, Valentina Carabelli, and Emilio Carbone. Amyloid beta42 oligomers up-regulate the excitatory synapses by potentiating presynaptic release while impairing postsynaptic nmda receptors. *The Journal of Physiology*, 598(11):2183–2197, 2020.

[182] M Papa and Menahem Segal. Morphological plasticity in dendritic spines of cultured hippocampal neurons. *Neuroscience*, 71(4):1005–1011, 1996.

[183] David Attwell and Simon B Laughlin. An energy budget for signaling in the grey matter of the brain. *Journal of Cerebral Blood Flow & Metabolism*, 21(10):1133–1145, 2001.

[184] Daniela Gavello, Chiara Calorio, Claudio Franchino, Federico Cesano, Valentina Carabelli, Emilio Carbone, and Andrea Marcantoni. Early alterations of hippocampal neuronal firing induced by abeta42. *Cerebral Cortex*, 28(2):433–446, 2018.

[185] Isabella Russo, Daniela Gavello, Elisabetta Menna, David Vandael, Carola Veglia, Noemi Morello, Irene Corradini, Elisa Focchi, Annalisa Alfieri, Costanza Angelini, et al. p140cap regulates gabaergic synaptogenesis and development of hippocampal inhibitory circuits. *Cerebral Cortex*, 29(1):91–105, 2019.

[186] N Fujiwara, H Higashi, S Nishi, K Shimoji, S Sugita, and M Yoshimura. Changes in spontaneous firing patterns of rat hippocampal neurones induced by volatile anaesthetics. *The Journal of Physiology*, 402(1):155–175, 1988.

[187] E Moreva, E Bernardi, P Traina, A Sosso, S Ditalia Tchernij, J Forneris, F Picollo, G Brida, Ž Pastuović, IP Degiovanni, et al. Practical applications of quantum sensing: A simple method to enhance the sensitivity of nitrogen-vacancy-based temperature sensors. *Physical Review Applied*, 13(5):054057, 2020.

[188] D Gatto Monticone, K Katamadze, Paolo Traina, E Moreva, Jacopo Forneris, Ivano Ruo-Berchera, Paolo Olivero, Ivo Pietro Degiovanni, Giorgio Brida, and M Genovese. Beating the abbe diffraction limit in confocal microscopy via nonclassical photon statistics. *Physical review letters*, 113(14):143602, 2014.

[189] BE Leonard. Principles of neural science, by er kandel, jh schwartz and tm jessell. appleton & lange, 1991. pp. 1135+ xxxvii. isbn 0-8385-8068-8, 1993.

[190] Stephen M Smith. Fast robust automated brain extraction. *Human brain mapping*, 17(3):143–155, 2002.

[191] Gopalakrishnan Balasubramanian, Philipp Neumann, Daniel Twitchen, Matthew Markham, Roman Kolesov, Norikazu Mizuochi, Junichi Isoya, Jocelyn Achard, Johannes Beck, Julia Tissler, et al. Ultralong spin coherence time in isotopically engineered diamond. *Nature materials*, 8(5):383–387, 2009.

[192] Jocelyn Achard, Vincent Jacques, and Alexandre Tallaire. Cvd diamond single crystals with nv centres: a review of material synthesis

and technology for quantum sensing applications. *Journal of Physics D: Applied Physics*, 2020.

[193] Ettore Bernardi, Richard Nelz, Selda Sonusen, and Elke Neu. Nanoscale sensing using point defects in single-crystal diamond: recent progress on nitrogen vacancy center-based sensors. *Crystals*, 7(5):124, 2017.

[194] Edlyn V Levine, Matthew J Turner, Pauli Kehayias, Connor A Hart, Nicholas Langellier, Raisa Trubko, David R Glenn, Roger R Fu, and Ronald L Walsworth. Principles and techniques of the quantum diamond microscope. *Nanophotonics*, 8(11):1945–1973, 2019.

[195] A Dréau, M Lesik, L Rondin, P Spinicelli, O Arcizet, J-F Roch, and V Jacques. Avoiding power broadening in optically detected magnetic resonance of single nv defects for enhanced dc magnetic field sensitivity. *Physical Review B*, 84(19):195204, 2011.

[196] Chang S Shin, Claudia E Avalos, Mark C Butler, David R Trease, Scott J Seltzer, J Peter Mustonen, Daniel J Kennedy, Victor M Acosta, Dmitry Budker, Alexander Pines, et al. Room-temperature operation of a radiofrequency diamond magnetometer near the shot-noise limit. *Journal of Applied Physics*, 112(12):124519, 2012.

[197] Erik Bauch, Swati Singh, Junghyun Lee, Connor A Hart, Jennifer M Schloss, Matthew J Turner, John F Barry, Linh Pham, Nir Bar-Gill, Susanne F Yelin, et al. Decoherence of dipolar spin ensembles in diamond. *arXiv preprint arXiv:1904.08763*, 2019.

[198] Michael Sean Grinolds, Sungkun Hong, Patrick Maletinsky, Lan Luan, Mikhail D Lukin, Ronald Lee Walsworth, and Amir Yacoby. Nanoscale magnetic imaging of a single electron spin under ambient conditions. *Nature Physics*, 9(4):215–219, 2013.

[199] Liam P McGuinness, Yuling Yan, Alastair Stacey, David A Simpson, Liam T Hall, Dougal Maclaurin, Steven Prawer, P Mulvaney, J Wrachtrup, F Caruso, et al. Quantum measurement and orientation tracking of fluorescent nanodiamonds inside living cells. *Nature nanotechnology*, 6(6):358, 2011.

[200] G De Lange, ZH Wang, D Riste, VV Dobrovitski, and R Hanson. Universal dynamical decoupling of a single solid-state spin from a spin bath. *Science*, 330(6000):60–63, 2010.

[201] Piotr Szańkowski, Guy Ramon, Jan Krzywda, Damian Kwiatkowski, et al. Environmental noise spectroscopy with qubits subjected to dynamical decoupling. *Journal of Physics: Condensed Matter*, 29(33):333001, 2017.

[202] Boris Naydenov, Florian Dolde, Liam T Hall, Chang Shin, Helmut Fedder, Lloyd CL Hollenberg, Fedor Jelezko, and Jörg Wrachtrup. Dynamical decoupling of a single-electron spin at room temperature. *Physical Review B*, 83(8):081201, 2011.

[203] Helena S Knowles, Dhiren M Kara, and Mete Atatüre. Observing bulk diamond spin coherence in high-purity nanodiamonds. *Nature materials*, 13(1):21–25, 2014.

[204] Q-Y Cao, P-C Yang, M-S Gong, M Yu, A Retzker, Martin B Plenio, C Müller, N Tomek, B Naydenov, LP McGuinness, et al. Protecting quantum spin coherence of nanodiamonds in living cells. *Physical Review Applied*, 13(2):024021, 2020.

[205] Mariusz Mrózek, Daniel Rudnicki, Pauli Kehayias, Andrey Jarmola, Dmitry Budker, and Wojciech Gawlik. Longitudinal spin relaxation in nitrogen-vacancy ensembles in diamond. *EPJ Quantum Technology*, 2(1):22, 2015.

[206] Mariusz Radtke, Ettore Bernardi, Abdallah Slablab, Richard Nelz, and Elke Neu. Nanoscale sensing based on nitrogen vacancy centers in single crystal diamond and nanodiamonds: achievements and challenges. *Nano Futures*, 3(4):042004, 2019.

[207] Nir Bar-Gill, Linh My Pham, Chinmay Belthangady, David Le Sage, Paola Cappellaro, JR Maze, Mikhail D Lukin, Amir Yacoby, and Ronald Walsworth. Suppression of spin-bath dynamics for improved coherence of multi-spin-qubit systems. *Nature communications*, 3(1):1–6, 2012.

[208] Analia Zwick, Gonzalo A Álvarez, and Gershon Kurizki. Maximizing information on the environment by dynamically controlled qubit probes. *Physical Review Applied*, 5(1):014007, 2016.

[209] Matthias M Müller, Stefano Gherardini, Nicola Dalla Pozza, and Filippo Caruso. Noise sensing via stochastic quantum zeno. *Physics Letters A*, 384(13):126244, 2020.

[210] Christian Arenz, Daniel Burgarth, Paolo Facchi, Vittorio Giovannetti, Hiromichi Nakazato, Saverio Pascazio, and Kazuya Yuasa. Universal control induced by noise. *Physical Review A*, 93(6):062308, 2016.

[211] Haitham AR El-Ella, Sepehr Ahmadi, Adam M Wojciechowski, Alexander Huck, and Ulrik L Andersen. Optimised frequency modulation for continuous-wave optical magnetic resonance sensing using nitrogen-vacancy ensembles. *Optics express*, 25(13):14809–14821, 2017.

[212] Hannah Clevenson, Matthew E Trusheim, Carson Teale, Tim Schröder, Danielle Braje, and Dirk Englund. Broadband magnetometry and temperature sensing with a light-trapping diamond waveguide. *Nature Physics*, 11(5):393–397, 2015.

[213] Georgios Chatzidrosos, Arne Wickenbrock, Lykourgos Bougas, Nathan Leefer, Teng Wu, Kasper Jensen, Yannick Dumeige, and Dmitry Budker. Miniature cavity-enhanced diamond magnetometer. *Physical Review Applied*, 8(4):044019, 2017.

[214] Kejie Fang, Victor M Acosta, Charles Santori, Zhihong Huang, Kohei M Itoh, Hideyuki Watanabe, Shinichi Shikata, and Raymond G Beausoleil. High-sensitivity magnetometry based on quantum beats in diamond nitrogen-vacancy centers. *Physical review letters*, 110(13):130802, 2013.

[215] Adam M Wojciechowski, Mürsel Karadas, Christian Osterkamp, Steffen Jankuhn, Jan Meijer, Fedor Jelezko, Alexander Huck, and Ulrik L Andersen. Precision temperature sensing in the presence of magnetic field noise and vice-versa using nitrogen-vacancy centers in diamond. *Applied Physics Letters*, 113(1):013502, 2018.

[216] E. Moreva, E. Bernardi, P. Traina, A. Sosso, S. Ditalia Tchernij, J. Forneris, F. Picollo, G. Brida, Ž. Pastuović, I. P. Degiovanni, P. Olivero, and M. Genovese. Practical applications of quantum sensing: A simple method to enhance the sensitivity of nitrogen-vacancy-based temperature sensors. *Phys. Rev. Applied*, 13:054057, May 2020.

[217] Jinhu Xiong, Peter T Fox, and Jia-Hong Gao. Directly mapping magnetic field effects of neuronal activity by magnetic resonance imaging. *Human brain mapping*, 20(1):41–49, 2003.

[218] Bingshuo Li, Juha P Virtanen, Axel Oeltermann, Cornelius Schwarz, Martin A Giese, Ulf Ziemann, and Alia Benali. Lifting the veil on the dynamics of neuronal activities evoked by transcranial magnetic stimulation. *Elife*, 6:e30552, 2017.

[219] Dimitri M Kullmann. Neurological channelopathies. *Annual review of neuroscience*, 33:151–172, 2010.

[220] Stephen G Waxman. Axonal conduction and injury in multiple sclerosis: the role of sodium channels. *Nature Reviews Neuroscience*, 7(12):932–941, 2006.

[221] David Cohen. Magnetic fields around the torso: production by electrical activity of the human heart. *Science*, 156(3775):652–654, 1967.

[222] Annette Wacker-Gussmann, Janette F Strasburger, Bettina F Cuneo, and Ronald T Wakai. Diagnosis and treatment of fetal arrhythmia. *American journal of perinatology*, 31(07):617–628, 2014.

[223] Laura T Knoll, Giulia Petrini, Fabrizio Piacentini, Paolo Traina, Sergey V Polyakov, Ekaterina Moreva, Ivo Pietro Degiovanni, and Marco Genovese. Mode structure reconstruction by detected and undetected light. *arXiv preprint arXiv:2212.13873*, 2022.

[224] Ettore Bernardi, Ekaterina Moreva, Paolo Traina, Giulia Petrini, Sviatoslav Ditalia Tchernij, Jacopo Forneris, Željko Pastuović, Ivo Pietro Degiovanni, Paolo Olivero, and Marco Genovese. A biocompatible technique for magnetic field sensing at (sub) cellular scale using nitrogen-vacancy centers. *EPJ Quantum Technology*, 7(1):13, 2020.